

CRANFIELD UNIVERSITY

GONZALO VALDES

URBAN AIR MOBILITY FLIGHT DYNAMICS

School of Aerospace, Transport and Manufacturing
Aerospace Dynamics

MSc in Aerospace Dynamics
Academic Year: 2019 -2020

Supervisor: Mudassir Lone
Associate Supervisor: Julien Enconniere
August 2020

CRANFIELD UNIVERSITY

School of Aerospace, Transport and Manufacturing
Aerospace Dynamics

MSc

Academic Year 2019 - 2020

GONZALO VALDES

URBAN AIR MOBILITY FLIGHT DYNAMICS

Supervisor: Mudassir Lone
Associate Supervisor: Julien Enconniere
August 2020

This thesis is submitted in partial fulfilment of the requirements for
the degree of MSc in Aerospace Dynamics

© Cranfield University 2020. All rights reserved. No part of this
publication may be reproduced without the written permission of the
copyright owner.

ABSTRACT

Electric Urban Air Mobility arises as an alternative to conventional means of transportation. However, current electric battery technology imposes restrictions on performance due to its low specific power and energy. A feasibility analysis of a 2000kg MTOW, three tilt-rotor EVTOL with canard configuration based on the Aston Martin Volante UAM concept was performed. The mission objective was defined as flying over a range of 300km, at 300km/h and 1000m altitude. This work provides a modelling environment for propeller-driven EVTOLs. The tool, composed by the aircraft model, an optimisation module and a performance module, allows for design and performance tasks within the conceptual design stage. The aircraft model includes airframe aerodynamics, propeller aerodynamics, Li-ion battery and inertia properties. Aerodynamic model is based on Vortex Lattice Method, whereas propeller model is based on Blade Element Momentum Theory. The optimisation module allows to obtain a set of best configurations for different flight conditions, so the associated trade-offs can be analysed. The performance module includes trim and mission analysis capabilities. Optimum configuration and thrust distribution at hover for each propeller were obtained for different configurations. The concept proved to be unfeasible with current battery technology for the defined mission. Results yielded a need to increase current energy density by a factor of 3.1.

Keywords:

Tilt-rotor, Response surface, Optimization, EVTOL, Canard, AVL, QPROP

ACKNOWLEDGEMENTS

I would like to thank Julien Enconniere. This project would be completely different without his invaluable help and continuous guidance through these last months.

TABLE OF CONTENTS

ABSTRACT	i
ACKNOWLEDGEMENTS	ii
TABLE OF CONTENTS	iii
LIST OF FIGURES	vi
LIST OF TABLES	ix
LIST OF ABBREVIATIONS	x
1. Introduction	1
1.1. Electric-powered aviation	2
1.2. Urban Air Mobility	3
1.3. Current project configuration	5
2. Aims and Objectives	8
3. Literature review	9
3.1. Modelling	9
3.2. Aerodynamic modelling	10
3.2.1. Solvers	11
3.3. Propeller modelling	12
3.3.1. Blade Element Momentum Theory solvers	13
3.4. Design considerations	13
3.4.1. EVTOL configurations	14
3.4.2. Airframe design	14
3.4.3. Rotor design	17
4. Modelling	20
4.1. Aerodynamic modelling	20
4.1.1. Aerodynamic model structure	20
4.1.2. AVL	21
4.1.4. Empirical $CD0$ estimation	26
4.1.5. Empirical K estimation	28
4.2. Mass distribution and inertia calculation	29
4.2.1. Mass distribution	29
4.2.2. Inertia calculation	31
4.2.3. Inertia model validation	33
4.3. Propeller model	34
4.3.1. QPROP theory	34

4.3.2.	Limitations	36
4.3.3.	Propeller angle of attack correction	39
4.4.	Battery	40
4.4.1.	Cell model	40
4.4.2.	Battery pack modelling	43
4.5.	Simulink model	45
4.6.	Optimization	48
4.6.1.	Genetic Algorithm	49
4.6.2.	Pattern search algorithm	50
4.7.	Response surface	50
4.7.1.	Seeding	52
4.7.2.	Metamodel fitting: Interpolation, regression and neural networks.	52
4.7.3.	Methodology comparison	56
4.8.	Model Assembly	58
4.8.1.	Optimization model assembly	58
4.8.2.	Performance trimming module	62
4.9.	Battery performance analysis	64
4.9.1.	Mission definition	65
4.9.2.	Battery and model assembly and optimization	66
5.	Discussion of results	68
5.1.	Propeller Optimization	68
5.1.1.	Optimization Results Analysis	68
5.1.2.	Propeller efficiency study	72
5.2.	Airframe Optimization	74
5.3.	Full aircraft optimization	77
5.3.1.	Previous configurations insights	77
5.3.2.	Full aircraft optimization results for back propeller diameter of 2m.	79
5.3.3.	Sensibility analysis	86
5.3.4.	Optimization results for variations in propeller diameter and CG.	89
5.4.	Performance analysis	92
5.4.1.	Trim analysis	92
5.4.2.	Battery performance	98
5.5.	Assessment against other aircraft	102
6.	Conclusions	105

6.1. Achievement of the objectives	105
6.2. Key findings	106
6.3. Future work	107
Bibliography	109
Appendix A	116
Canard aircraft data	116
Rotorcraft and Tilt-rotor Data	119
UAM Data	121

LIST OF FIGURES

Figure 1.1: Urban and rural population projections.....	1
Figure 1.2: UK ambient air quality. Left, NO_2 particle concentration annual mean. Right, $\text{PM}_{2.5}$ particle concentration annual mean	2
Figure 1.3: EHang 184(2000), Airbus Vahana(2019c), Kitty Hawk(2020) and Lilium Jet(2020).	4
Figure 1.4: Side view(up) and plant view(down) of Aston Martin Volante concept (Aston Martin, 2020).	6
Figure 3.1: Canard aircraft wing area, wingspan and aspect ratio comparison as a function of MTOW.....	15
Figure 3.2: Disk loading comparison for different aircraft. Extracted from Leishman(2006), left, and Maisel, Giulianetti and Dugan(2000), right.	18
Figure 4.1: Aerodynamic model structure.....	20
Figure 4.2: Airframe simplified plant geometry.	21
Figure 4.3: Vortex Lattice Method filament diagram. Adapted from Anderson(2001).	22
Figure 4.4: Jetstream 31 geometry implemented in AVL.....	25
Figure 4.5: Graphical representation of the aerodynamic coefficients for Jetstream 31 validation results.	26
Figure 4.6: Diagram representing the simplified surfaces for inertia calculation.	31
Figure 4.7: Propeller blade velocity decomposition at a certain radial location r. Adapted from Drela(2006)	35
Figure 4.8: Propeller blade velocity triangle and forces at a radius r. Adapted from Drela(2006).....	36
Figure 4.9: Aerodynamic coefficients curves definition on QPROP. Extracted from Drela(2005).....	37
Figure 4.10: Simplified propeller velocity diagram.	38
Figure 4.11: Rotational speed limits as a function of airspeed, altitude and propeller diameter for $M < 0.7$ (left) and $M < 0.8$ (right) constrains.	39
Figure 4.12: Propeller corrections for angle of attack and sideslip. Extracted from ESDU 89047(2016).	39
Figure 4.13: Cell electric diagram. Adapted from Chen and Rincón-Mora(2006).	41
Figure 4.14: Relative available capacity r_c as a function of discharge rate. Extracted from Vratny et al.(2013).	42
Figure 4.15: Battery model diagram. Adapted from Vratny et al(2013).	44
Figure 4.16: Battery study for increase in the number of batteries in series and in parallel.	44
Figure 4.17: Simulink model global structure.....	46
Figure 4.18: Simulink model powerplant structure.....	47
Figure 4.19: Propellers and body axes diagram.	47
Figure 4.20: Pattern search dominated area defined by Hypervolume criterion.	50
Figure 4.21: Response surface creation diagram.....	51
Figure 4.22: Box-Behnken and factorial design seeding diagrams.....	52

Figure 4.23: Error histogram comparing regression and validation errors.	54
Figure 4.24: Feed-forward and cascade-forward neural network architectures.	55
Figure 4.25: Error histogram for Simple vs complex regression models.	57
Figure 4.26: Error histograms for the different configurations	58
Figure 4.27: Comparison of aeroderivatives results with response surface and the full model.	58
Figure 4.28: Full aircraft simplified plant diagram.	59
Figure 4.29: Model integration diagram for the optimization process.	59
Figure 4.30: Propeller forces diagram during hover.	60
Figure 4.31: Optimization scheme diagram.	62
Figure 4.32: Trimming routine diagram.	63
Figure 4.33: Emrax motor performance curves. Extracted from Emrax(2020).	66
Figure 4.34: Battery performance model assembly.	67
Figure 5.1: Propeller multi-objective optimization pareto front.	69
Figure 5.2: Chord, pitch angle, maximum camber and maximum thickness distributions for three different points in the Pareto front obtained from the propellers multi-objective optimization.	71
Figure 5.3: Chord, pitch angle, maximum camber and maximum thickness mean values for all the points in the Pareto front obtained from the propellers multi-objective optimization.	72
Figure 5.4: Optimized propeller for hover condition at altitude of 0m for different thrust and propeller diameter values.	73
Figure 5.5: Aircraft geometry comparison, Single-objective Cruise 300km/h(blue) vs Multi-objective Cruise 300km/h and Cruise 170km/h(black).	75
Figure 5.6: Full aircraft optimisation Pareto Front.	81
Figure 5.7: Chord, pitch angle, maximum camber and thickness distribution for the three points selected from the Pareto front in Figure 5.6.	82
Figure 5.8: Chord, pitch angle, maximum camber and thickness mean values as a function of power required at cruise for all the points from the Pareto front in Figure 5.6.	83
Figure 5.9: Percentage of thrust generated by the back propeller during hover as a function of power at hover(left) and power at cruise(right).	84
Figure 5.10: Airframe geometry(up) and CG location(down) for the multi- objective full aircraft optimization.	85
Figure 5.11: Aeroderivatives as a function of power at cruise for full model optimization	85
Figure 5.12: Trimming angles (airframe angle of attack, propeller angle of attack and elevator deflection) as a function of power at cruise for the full model optimization	86
Figure 5.13: Comparison of optimization results. Red, optimization results as seen in 5.3.2. Black, optimization with transonic limitation constrain for blade tip Mach below 0.7.	88
Figure 5.14: Pareto front for the original configuration and the different variants. Left, whole domain. Right, zoom in the black square.	91
Figure 5.15: Percentage of thrust provided by the back propeller at hover as a function of Power at cruise at 300km/ for Variant 1 and Variant 3.	91

Figure 5.16: Power and thrust required as a function of airspeed and altitude for the D=2m optimized aircraft.	93
Figure 5.17: Trimming angles as a function of airspeed and altitude for the D=2m optimized aircraft.....	95
Figure 5.18: Power required as a function of airspeed and tilt angle for altitude=0m.	96
Figure 5.19: Propeller angle of attack(left) and Airframe angle of attack(right) as a function of airspeed and tilt angle for altitude=0m.....	97
Figure 5.20: Percentage of thrust by the back propeller at hover(left) and power by the back propeller at hover(right) as a function of airspeed and tilt angle for altitude=0m.	97
Figure 5.21: Pareto front and optimum mission points of 'Original' and 'Variant 1' configurations.....	98
Figure 5.22: Battery parameters evolution during the mission described in Section 4.9.1.Config 1 is the original configuration while Config 2 represents Variant 1.	100
Figure 5.23: Hover time as a function of power density multiplier for the current mass. Config 1 is the original configuration while Config 2 represents Variant 1.	101
Figure 5.24: Disk loading and ideal hover efficiency for current project and a range of helicopters, tilt-rotors and Urban Air Mobility projects.....	102
Figure 5.25:Wing surface, span and aspect ratio as a function of MTOW for different canard aircraft and current configuration.	103
Figure 5.26: Stall speed as a function of MTOW for different canard aircraft and current project configuration.	104

LIST OF TABLES

Table 4.1: Aerodynamic coefficients results from Dantsker and Vahora(2018).	24
Table 4.2: Specific values for the aerodynamic coefficients for Jetstream 31 validation results.	26
Table 4.3: Mass distribution along aircraft groups.	29
Table 4.4: Systems distribution for conventional military aircraft. Extracted from Lanham(1979).	30
Table 4.5: Mass distribution for the whole aircraft.	30
Table 4.6: Geometric properties extracted from Jetstream 31 Datapack(Cooke,2013)	33
Table 4.7: Validation of inertia model against Jetstream 31 data for the wing. .	33
Table 4.8: UAM vs Fokker 100 non-dimensional inertia values comparison. ...	34
Table 5.1: Parameters and bounds for propeller multi-objective optimization. .	69
Table 5.2: Optimization parameters with correspondent upper and lower boundaries.	74
Table 5.3: Airframe optimization results for the single-objective optimization only considering cruise and the multi-objective optimization considering stall limitations.	76
Table 5.4: Full aircraft optimization parameters and bounds.	80
Table 5.5: Span sensitivity study for the final D=2m configuration.	87
Table 5.6: CG position sensitivity study for the final D=2m configuration.	87
Table 5.7: Mass sensitivity study for the final D=2m configuration.	88
Table 5.8: Variant configurations boundaries during the optimization.	90
Table 5.9: Original and Variant 1 required mass and increase in specific energy to complete mission described in Section 4.9.1	99
Table 5.10: Percentage of SOC consumed at each flight phase and remaining SOC in the end.	99

LIST OF ABBREVIATIONS

AR	Aspect Ratio
BPROP	Back Propeller
CFD	Computational Fluid Dynamics
CG	Centre of Gravity
EASA	European Union Aviation Safety Agency
EVTOL	Electric Vertical Take-Off and Landing
FPROP	Forward Propeller
fus	Fuselage
MTOW	Maximum Take-Off Weight
TAS	True Airspeed
UAM	Urban Air Mobility
VTOL	Vertical Take-Off and Landing
<i>B</i>	Number of blades
<i>DCM</i>	Direction-Cosine Matrix
<i>c</i>	Chord/canard
<i>C</i>	Capacity
C_{L0}	Lift coefficient intercept $\frac{L_0}{q_\infty S_w V_\infty^2}$
$C_{L\alpha}$	Lift coefficient slope
C_{D0}	Zero-lift drag $\frac{D_0}{q_\infty S_w V_\infty^2}$
C_{M0}	Moment coefficient intercept $\frac{M_0}{q_\infty S_w V_\infty^2}$
$C_{M\alpha}$	Moment coefficient slope
C_P	Power coefficient $\frac{P}{\rho n^3 D^5}$
C_Q	Torque coefficient $\frac{Q}{\rho n^2 D^5}$
C_T	Thrust coefficient $\frac{T}{\rho n^2 D^4}$
<i>D</i>	Diameter/Drag
<i>e</i>	Oswald factor
<i>J</i>	Advance ratio $\frac{V_\infty}{nD}$
<i>I</i>	Current
<i>K</i>	Induced drag coefficient
<i>L</i>	Lift
<i>le</i>	Leading edge

M	Mach number
n	Revolutions per second
P	Power
Q	Torque
q_{∞}	Dynamic Pressure $0.5\rho V_{\infty}^2$
r	Radius(location)
R	Radius(tip)
Re	Reynolds number
SOC	State of Charge
S_{ref}	Reference surface
S_w	Wing surface
S_{wet}	Wet surface
T	Thrust
$\frac{t}{c}$	Maximum thickness relative to the chord of the airfoil
te	Trailing edge
V	Voltage
V_{∞}	True airspeed
W	Weight
W_{prop}	Blade airspeed
X	Force in the Y axis (Body axes, positive right wing)
Z	Force in the Z axis (Body axes, positive downwards)
α_b	Body/Airframe angle of attack
α_{prop}	Propeller angle of attack
β	Sideslip
β_{prop}	Pitch angle of propeller
β_{75}	Pitch angle of propeller at 75% of the tip radius
γ	Flight path angle
θ	Pitch angle
ρ	Density
ω/Ω	Rotational speed
φ	Yaw angle
Λ	Sweep angle

λ	Taper ratio
$\eta / \eta_{elevator}$	Elevator deflection
η_p	Propulsive efficiency
Γ	Circulation

1. Introduction

Worldwide, more than 4 billion people live in urban areas (United Nations, 2018). Concentration of population in urban settlements has been rising over the years, and the trend is becoming steeper. According to United Nations (2016) data, an estimated of 54.5% of the population is currently concentrated in these areas. The projections elevate this value to a 60% by 2030. By 2050, the estimate surges to two-thirds of the population living in urban areas. Although population growth rate is estimated to fall for the next years, the estimates expect an increase from 7.7billion people to 9.7billion in 2005 (Our World in Data, 2019).

Traffic congestion is an issue in urban areas across the world. In larger European cities like Madrid, Paris or London, people lose around 78, 165 and 149 hours, respectively, each year due to congestion issues (INRIX, 2019a). For UK, this translated into a cost of 6.9 billion during 2019 (INRIX, 2019b). Given the tendencies in urban population growth, traffic congestion in urban areas will keep posing a problem for the next years.

Urban and rural population projected to 2050, World, 1500 to 2050

Total urban and rural population, given as estimates to 2016, and UN projections to 2050. Projections are based on the UN World Urbanization Prospects and its median fertility scenario.

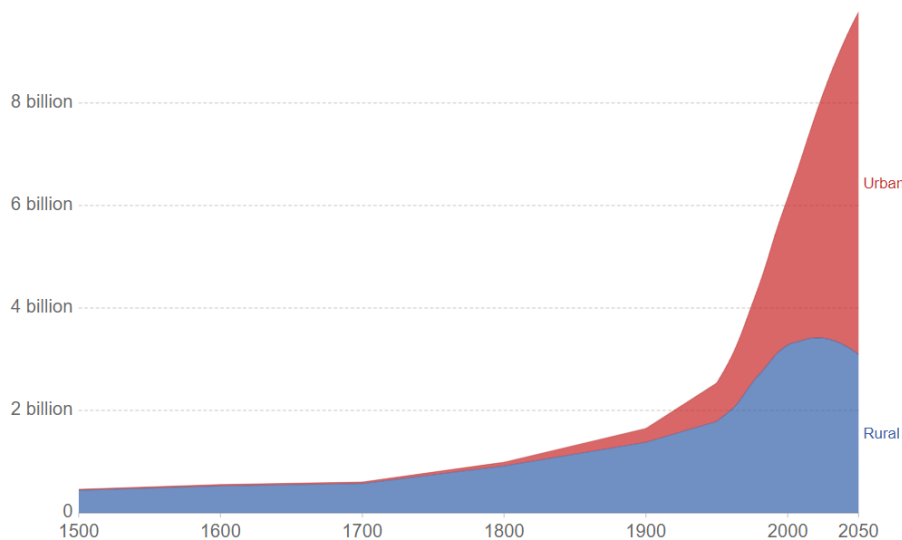


Figure 1.1: Urban and rural population projections.

This growth in urban traffic congestion and pollution is demanding alternatives to conventional means of transportation. Urban Air Mobility arises as one of the possible solutions for this problem. However, energy consumption and emissions must be further considered.

One of the issues associated with people concentration and traffic congestion is air pollution. Air pollution is a relevant issue in large urban areas, where NO₂ and other potentially prejudicial particles concentration is considerably higher than in less populated areas, as observed in Figure 1.2. Energy demand, and thus emissions, for flying vehicles are higher than the required by grounded ones. Airplane present emission levels are over 5 times the average car ones, 285g CO₂/passenger/km vs 55 g of CO₂/passenger/km respectively (European Environment Agency, 2019). In the context of urban mobility, this difference may be attenuated by the increase in time spent in traffic congestion. Nevertheless, this is still a relevant problem that must be solved.

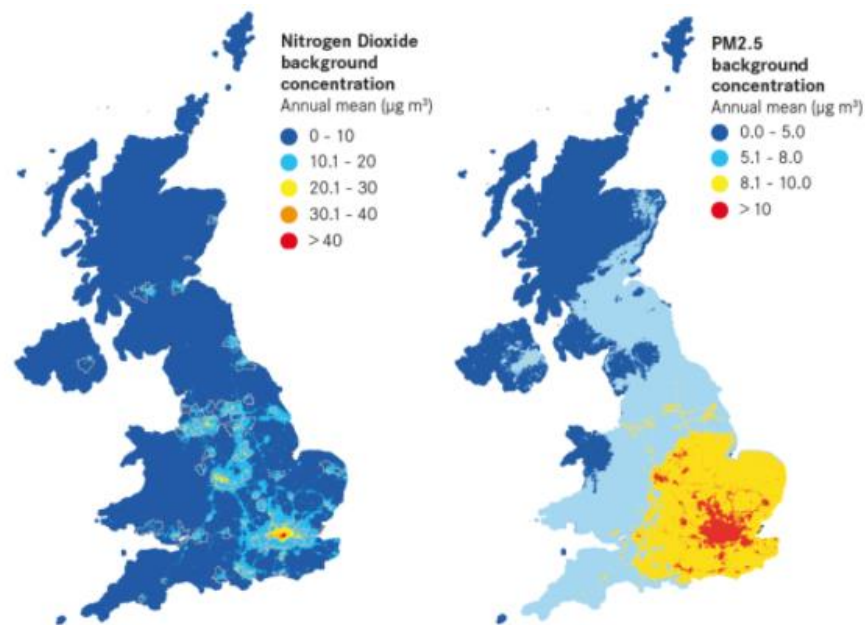


Figure 1.2: UK ambient air quality. Left, NO₂ particle concentration annual mean. Right, PM_{2.5} particle concentration annual mean

1.1. Electric-powered aviation

Environment is a sensitive issue for international politics and has a relevant impact on companies and organisms decision making. Although controversial, the effect of emissions on global warming is a potential risk to the planet. Thus, reduction of emissions should be a focus for future technology. Electric powered aviation could be an alternative for this reduction, as it can be considered as locally emission free.

Lithium-Ion batteries are the most extended for every electric application constrained by mass, from mobile devices to electric aviation. Other types of Lithium based battery systems are being developed right now, like Li-S or Li-O₂,

which provide energy densities from 3 to 10 times the Li-ion. However, these technologies are not expected to be available within the next few years (Hepperle, 2012). Other options like Hydrogen require high pressure tanks, extremely heavy and voluminous, apart from the safety issues related to its use. Electric batteries seem the most realistic alternative to conventional kerosene, given the safety requirements and space restrictions in air transportation.

The current problem with Li-ion batteries is their relatively low energy density. Current most advanced Li-ion batteries present a specific energy around 230Wh/kg (Hohm Tech, 2020), compared to the kerosene values around 12000Wh/kg (Vratny et al. (2013)). Thus, kerosene values of specific energy are above 50 times the provided by the Li-ion battery. Compared to conventional aviation, electric-powered aircraft are expected to suffer considerable mass penalties.

In battery systems, the energy is stored in batteries allowing for direct extraction of electric power. The efficiency is limited by the chemical processes occurring during charging and discharging. Another difference to conventional aviation is that the battery mass does not change as its discharged. Thus, the benefit of loss of weight during the operation is lost (Vratny et al., 2013).

On the positive side, electric propulsion systems present better efficiency in the energy conversion chain. Estimations in the whole conversion cycle yield results over 70% of efficiency compared to the around 40% from conventional combustion systems (Hepperle, 2012). This is backed up by the high maximum efficiency of current electric motor technology. Integral Powertrain (2020), based on liquid cooling technology, present a model with a maximum efficiency over 98%. Emrax(2020) models present minimum efficiency levels over 90% at off-design conditions.

In 2012, Hepperle (2012) stated that battery technology limited practical flight to small vehicles with up to 2 passengers. A more recent work by Bacchini and Cestino(2019b) estimated that the range achievable by electric VTOLs with the current battery technology is in the order of 200 km for 2 passengers.

1.2. Urban Air Mobility

Multiple configurations have been developed and tested during the last years. These different configurations address different needs. Depending on the mission it is designed for, the configuration will considerably vary. Wingless Multicopters will provide better hover performance, while vectored thrust, tilt-wing and tilt-rotors will provide longer ranges and airspeeds. In the middle, vehicles with two different propulsion systems for hover and cruise flight provide a trade-off between both conditions.

As an example of the multirotor configuration, CityAirbus (Airbus, 2020b) UAM project was conceived as an electric multirotor flying taxi. Ducted counter-rotating propeller rotating at around 950rpm were used to ensure low noise levels. With an autonomy of 15 minutes, it is designed to carry 4 passengers at a cruise speed of 120km/h. EHang(2020) have developed a single-passenger wingless Multicopter able to maintain flight for 24 minutes. Volocopter (2020), with their Volocity aircraft, provided a range of 35km for a payload of 200kg. Maximum airspeed of these two vehicles is limited to 130km/h.

In the field of tilt-wing and tilt-rotors, Boeing with Kitty Hawk(2020) are developing a tilt-rotor aircraft able to transport 1 passenger 160 km at 350km/h., Another tilt-wing project has been launched by Airbus with the name of Vahana (Airbus,2020c). This single-seat aircraft would range 50km at a cruise speed of 190km/h.

Lilium Jet (2020) is developing a vectored thrust aircraft able to carry 4 passengers and a pilot at 300km/h during 60 minutes. This aircraft presents 36 electric engines integrated into the wings to reduce drag and provide optimum efficiency. This aircraft is currently being certified by EASA and FAA.



*Figure 1.3: EHang 184(2000), Airbus Vahana(2019c), Kitty Hawk(2020) and Lilium Jet(2020).
Top-left, top-right, bottom-left and bottom right respectively.*

The main benefit of these vehicles when compared to helicopters is the possible reduction in noise and price. Cost associated to propellant, maintenance and pilots could be reduced or eliminated for electric VTOLs. Meanwhile, Ducted fans and a proper optimization of the configuration can lead to significant noise reduction (Bacchini and Cestino, 2019b).

A market study requested by NASA (2018) defined the localized niche market scenarios where these vehicles could be profitable by 2030. Highly- populated areas could be able to implement 'vertiports'. These locations would function as air metro services located in heavily trafficked areas. Another niche would be transportation services, similar to the current urban helicopter transportation, focused on businesses and wealthy individuals.

Regarding the viability with current technology and infrastructure, development must be made in some areas. First would be the improvements required in electric battery and propulsion technologies. Then, autonomous flight must be consolidated, safely implementing detect-and-avoid systems like LIDAR and camera vision. In terms of infrastructure, a proper density of operational and charging stations is needed for optimal operability. Apart from this, a traffic management system, similar to the conventional air traffic management system, would be required both for unmanned and manned aircraft. (NASA, 2018) (Airbus, 2020b)

1.3. Current project configuration

The configuration assessed in this project is based on the concept of Aston Martin's Volante UAM project: A three tilt-rotor EVTOL canard configuration aircraft. Both forward propellers are tilting propellers, while back propeller is fixed. Counterrotating propellers are chosen due to the increase in efficiency and torque cancellation, facilitating control.

The aircraft MTOW is estimated as 2000kg for a payload of 300kg with two passengers and a pilot. The performance mission is defined as a range of 300km in one hour. Power source will be electric Li-ion batteries, limited to an initial estimation of 400kg.

Limitations on span and length were

A degree of uncoupling is added by optimizing the back propeller for hover while the forward propellers are more focused on cruise performance. This uncoupling is expected to provide improvements in the performance.

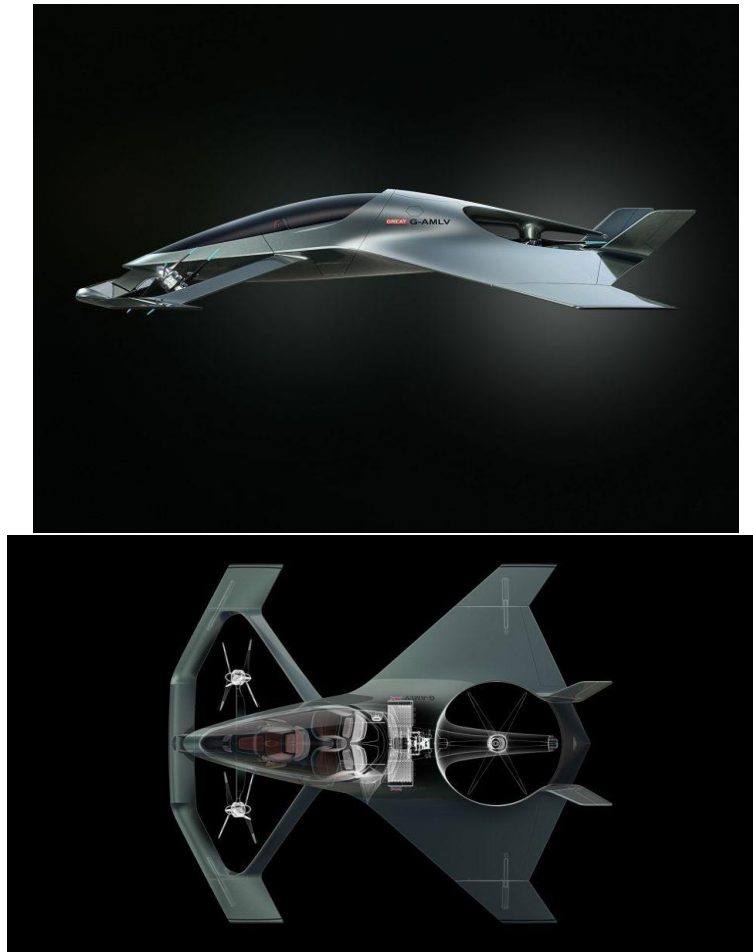


Figure 1.4: Side view(up) and plant view(down) of Aston Martin Volante concept (Aston Martin, 2020).

A description of the whole document is briefly introduced here:

Chapter 2 will introduce the aims and objectives for this project.

The literature review study is presented in Chapter 3. Different aspects about modelling and design will be treated here.

The presentation of the methodology is presented in Chapter 4. First, aerodynamic, propeller, battery and inertia models will be introduced. Then, the Simulink model which will be used for control and handling qualities analysis will be presented. Optimization algorithms and response surface methodology are introduced next. Finally, the whole model integration and the performance analysis methodology will be discussed.

Presentation of results and its discussion are done in Chapter 5. First, problem is decoupled to facilitate understanding before analysing the full aircraft results. Propeller and airframe are optimized separately in Section 5.1 and 5.2 respectively. Then full aircraft optimization results are presented in Section 5.3. Within the full aircraft optimization, a log with relevant insight gained through this project is first detailed. Next, results are presented accompanied by a sensibility analysis. Another section to provide insight about the relation between propeller

CG, diameter and performance is included. Performance is introduced in Section 5.5. Trimming conditions at each flight condition is presented first and then, the mission analysis is executed. Finally, results obtained will be compared against other canard aircraft, rotorcraft and UAM projects in Section 5.6.

To finalize, a summary with the conclusions, key findings and future work will be presented in Chapter 6.

2. Aims and Objectives

In the context of new Urban Air Mobility projects, multiple alternatives are being considered at the moment. A detailed analysis for each of this configuration is necessary. This analysis must be made considering the mission the aircraft is conceived for. The main objective of this work can be defined as:

- Analysis of the feasibility of the following concept: A 2000kg MTOW, three tilt-rotor EVTOL with canard configuration based on Aston Martin Volante UAM concept.

In order to be able to assess the feasibility of a concept, a model for each of the most relevant components is required. At a conceptual design stage, the modelling environment must be able to provide fast estimations while allowing flexibility with the configuration. The main concern with electric-powered aviation is the performance of the battery and its low specific energy compared to conventional sources of energy. Therefore, a Li-ion battery model is included in the simulation framework. The optimization module allows to obtain a set of optimum configurations for a set of flight conditions. The performance module requires the assessment of the viability of this concept with current technology by considering the power expenditure of the aircraft during a mission.

The objectives are summarized into:

- Development of a model of the aircraft for the following components: Airframe aerodynamics, propeller aerodynamics, battery and inertia properties.
- Integration of the model within an optimisation module.
- Development of a performance analysis module with trimming capabilities.
- Analysis of the key parameters and possible improvements to the design.
- Development of a dynamic model for flight control and handling qualities analysis.

Although the work in this project is just focused on a single configuration, this modelling environment can be extended to test any other propeller-powered aircraft design. This tool allows the modelling and optimization of conceptual designs to assess its performance for any operating conditions.

3. Literature review

3.1. Modelling

Given the high interaction between the multiple areas present in the field of aerospace design, constant trade-offs are present during the design process. Simultaneously, time restrictions limit the possibility of performing fully detailed analysis in every relevant area before taking a decision. One of the first tasks during design is to choose the level of interconnection and integration between the different disciplines involved (A.Keane, P. Nair, 2005, p34). The constant trade-off between precision and complexity determines the tools to be used at each design stage. Earlier stages like conceptual design will require low order computational tools that allow for fast redesigning of the configuration. Once the design advances, higher order tools are included in the process for increased accuracy(Gudmundsson, 2013, p12). Keane and Nair(2005, p22) stated that in the traditional design approach, during preliminary design, computational tools are used just for analysis. Decisions on the geometry are left to the designer depending on the outputs of the simulation.

Nigam et al. (2015) state that, with all the current regulation restrictions, performance requirements and the variety of design options, multi-disciplinary analysis becomes a must. Models should be able to provide, at least, aerodynamics, structural, propulsive and acoustic estimations in order to select the best option that complies with the regulation. A multidisciplinary analysis also increases flexibility in the definition of the cost functions and facilitates trade-off analysis. That way, complex compromises between different goals can be achieved simultaneously in the same optimization (Gur and Rosen, 2009). Regarding the number of points evaluated in the flight envelope, conventional single-point designs are being displaced by multi-point designs. This type of designs allows to analyse the trade-offs between different flight conditions (Nigam et al., 2015). In the case of this project, a multi-point design analysis is required, as aircraft must meet strict requirements for the whole flight envelope.

NASA, in their rotorcraft design and analysis environment NDARC (Johnson, 2010), introduce low fidelity models during conceptual design. Johnson's codes are built around the use of momentum theory for rotors, classical finite wing theory, a referred parameter engine model, and semiempirical weight estimation techniques. Gur and Rosen (2009) also introduce low fidelity codes in their propeller optimization methods. Their model is based on blade element method for aerodynamic estimation, Ffowxs-Williams equation for noise and a rod model for structural forces estimation.

Johnson (2010) stated that flexibility is a requirement to test new technology. A flexible architecture allows for the introduction of higher fidelity models if needed (Nigam et al., 2015). Furthermore, decomposition of the aircraft into fundamental components accelerates iteration and changes in the configuration.

Interactions effects between the different components can be relevant and cause relevant changes in the configuration. For example, propeller slipstream can be used as a lift generation mechanism. In some designs, disk-loading becomes a relevant parameter that leads to changes in wing surface to adapt for the increased levels of lift (Borst, 1973).

According to the guidance gathered in this section, model was conceived following a modular approach for the sake of flexibility. Each of the blocks would include different tools to model different components. That way, current tools can easily be replaced if needed. Even though the intention was to aim for a multidisciplinary model, time restriction limited the scope to aerodynamic modelling of propellers and airframe, inertia properties, battery modelling and performance analysis.

3.2. Aerodynamic modelling

A great number of aerodynamic modelling methods are present in the literature, each of them with different assumptions and simplifications. These assumptions and simplifications determine their accuracy, applicability and computational cost. Higher-fidelity codes provide more accurate estimations at the expense of an increase in computational resources (Keane and Nair, 2005, p22). Aerodynamic predictions must be updated through the flight cycle, varying from numerical methods to wind tunnel tests as soon as the design is defined. Main inaccuracy sources in these predictions are associated to simplifications in numerical methods and geometry uncertainty (Jobe 1984).

When deciding on the aerodynamic model to use, the first thing is to define the objective of the model and the conditions in which is going to be used. The objective of this model is to assess the performance so the viability of this concept can be evaluated. At the same time, during conceptual design evaluation, little detail is known and the aim is to determine the general trends and trade-offs. Furthermore, an optimization process must be implemented. All these statements lead to the selection of relatively fast tools. To be consistent with the objective of the optimization, 3D configuration must be evaluate for somewhat accurate performance estimations. Being coherent with the level of information available during conceptual design, linear, steady-state models seem reasonable. Given the relatively low Mach numbers, transonic effects are not relevant.

Furthermore, posterior handling qualities analysis and flight control design must be executed with this mode. Therefore, the aerodynamic characterization of the aircraft needs to include not only lift, drag and moments but also an estimation of its dynamic behaviour.

Possible solution methods that complied with these characteristics were Lifting Line Theory, Vortex-Lattice Method and Panel Method. More accurate methods involved CFD, whose computational time is orders of magnitudes above the desired. Less accurate solvers, XFOIL or VGK, included only 2D estimations, too inaccurate for the objectives of this project. Therefore, Lifting Line Theory and Vortex-Lattice methods will be studied in the following subsection.

3.2.1. Solvers

The solvers available for Vortex Lattice Method are AVL(Drela and Youngren, 2017) and Tornado(2020). Applicability of both softwares is similar and have almost the same capabilities. Both are only valid for thin wings and neglect viscous effects, thus having limited accuracy in drag and moments prediction. The difference is in the vortex modelling. AVL uses traditional horseshoe vortices, while Tornado uses vortex slings with seven filaments. Both programs include aeroderivatives calculation. Based on comparison made by Peerlings(2018), AVL accuracy is higher and running times are lower.

One of the problems with the previous solvers is the simplifications of the geometry. These programs. VSAero, based on 3D panel method, provide modelling capabilities for arbitrary geometries. Furthermore, higher accuracy results for relatively low increases in computational time are obtained (Peerlings, 2018). This code can be an interesting option once an initial geometry has been defined with the previous codes. Full airframe can be included in the design. Then, drag and moments could be estimated more accurately.

Considering the requirements of low runtime and the possibility of including drag corrections to account for viscous effects, AVL is chosen as the main tool for aerodynamic analysis. Furthermore, Cranfield Flight Dynamics Group had already developed scripts for the automation of the use of AVL with MATLAB.

Lift-induced drag can be calculated by a far field method like the Trefftz plane used on AVL. However, zero-lift drag requires use of the Navier-Stokes equations for accurate predictions. (Keane and Nair, 2005, p432). Approximated calculations with near-field techniques are time consuming and accuracy is not confirmed (Camberos et al., 2014). Camberos et al. developed a simplified method to calculate zero-lift drag. For a certain flight condition, zero-lift angle of attack was obtained. Then, drag was calculated considering 3D and viscous effects. Another approach is the use of empirical drag estimations based on historical data. Torenbeek(1982), Jobe(1984) or Raymer(1992 p281-283) are among the authors which have introduced these corrections for different types of aircraft. Methodology for these correction are very similar in most of the cases, based on statistical inference with historical data.

3.3. Propeller modelling

The benefit of using propellers lies in the high efficiency of as a thrust generation mechanism. This is due to the relatively low induced velocity to the flow compared to the large mass of air in-taken. Although velocity decays at higher speeds, for the airspeed where the current aircraft is designed for propellers are the most efficient option. (Hubbard,2010).

One factor leading to loss of efficiency in propellers is swirl in the wake resulting from engine torque. Generation of swirl uses energy but does not contribute to thrust. The amount of swirl generated is directly related to the power loading. To reduce the energy loss, a second rotor can be added behind a propeller rotating, resulting in a counterrotating propeller. Counterrotating propellers would increase efficiency by recovering the rotational energy losses from the front propeller. This cancellation can result in performance increases of 8 to 15 percent compared with that of single rotation propellers (Mikkelsen, Mitchel and Bober, 1984) (Hubbard,2010) (Borst, 1973). Counterrotating propellers allow for more efficient thrust production with lower loading per blade. Torque cancellation between the two stages eliminates the need of compensating torque. Drawbacks are the increase in shafting and gear systems complexity (Siddappaji and Turner, 2015).

Blade Element Momentum theory with Vortex theory is the preferred method to model both conventional and counterrotating propellers aerodynamics by many authors techniques (Drela and Youngren, 2003) (Molter and Cheng, 2017) (Thiele, Obster and Hornung, 2019)(Siddappaji and Turner, 2015). Prandtl's tip loss factor must be included to account for 3D effects in lift distribution. The problem with this theory is the inaccuracy at high disk loading due to swirl effects (Nigam et al., 2015).

For counterrotating propellers modelling, methodology vary depending on the author. Thiele, Obster and Hornung (2019) model axial gap and wake contraction with empirical methods, modelling each rotor individually. However, this approach requires further wind tunnel testing for accurate parameters adjustment. An alternative is the iterative process of convergence of the slipstream of both propellers. Front propeller is analysed first in isolation, obtaining the slipstream velocities. Then, forward propeller is analysed with these slipstream velocities accounted. This process is repeated until convergence, allowing to capture first order effects like swirl recovery. CROTOR (ESOTEC, 2011) and Nigam et al. (2015) follow this approach.

For operation at a certain propeller angle of attack, corrections are required for accurate estimations. Cooke(2013) in the Jetstream 31 model used an empirical correction to account for propeller inclination (ESDU,2006). Molter and Cheng (2017) tested both blade element method and BEMT method with a semi-empirical correction. The former provided errors below 10% against wind tunnel measurements. However, BEMT method, even with the empirical correction, provided more inaccurate results. Further tuning of the blade element method with wind tunnel data further increased accuracy.

Although structural modelling is not including in this project, Gur and Rosen (2009) reported that considerable reductions in von Mises stresses can be obtained for low reductions of propeller efficiency. In their study, a 90% reduction in Von Mises stress was reduced by a 90% for an increase of power required below 1%. This estimation seems excessively optimistic and should be further validated. Furthermore, different propeller designs and operating conditions will cause variation in the results.

3.3.1. Blade Element Momentum Theory solvers

A great number of solvers are available for BEMT method. Wisniewski et al. (2015) collected data of all these solvers. Different aspects were evaluated: applicability, accuracy, integration with other software and running time. Among all the options, QPROP and XROTOR seem to be the more viable choice for this current project. Apart from the validation and the available data for it, scripting method is similar to AVL, facilitating its implementation.

XROTOR(Drela and Youngren, 2003) and QPROP(Drela, 2006) are both softwares created by the same author and based on the same Blade Element Momentum/Vortex formulation. Moreover, corrections to account for swirl effects are included, providing accurate estimations for high disk loading. Thus, results are expected to be the same. The difference comes in the functionalities. QPROP

Validation on QPROP has been made by Van Kuijk(2015), De Leeuw(2013) and Dimchev(2012). Authors' results showed a good agreement with experimental data for high advance ratios, while divergence occurred at lower advance ratio, approximately $J < 0.6$ but varies depending on the propeller. This divergence could be explained by flow separation due to the high effective angles of attack. This situation may be especially relevant for the present study. Forward propellers will be optimized for both conditions but will focus more on cruise performance, therefore presenting relatively high pitch angles. At hover, the lower induced angle will cause high effective angles of attack, which may lead to separation not included into QPROP. Apart from lack of stall dynamics, low-fidelity software like QPROP neither accounts for transonic effects (Nigam et al., 2015).

3.4. Design considerations

The concept evaluated in this project is a propeller-driven EVTOL with a canard configuration. Considerations on the design of each of these categories will be introduced in this section.

3.4.1. EVTOL configurations

Being a relatively new concept, available information on UAM EVTOL projects is limited. A possible classification for UAM projects as a function of thrust type is made by the Vertical Flight Society(2020). The aircraft are divided in Vectored thrust, Lift+cruise, Multicopter, Hover bikes&Personal flying devices and electric helicopters.

The current project falls in the Lift + cruise category. Lift + cruise vehicles have two different propulsion systems, one for hover and another for cruise. Also, they are aerodynamically designed for an efficient cruise. Vectored thrust configurations present the same propulsion system for every condition and are aerodynamically designed for an efficient cruise. These vehicles present the most efficient cruise of all the vehicles, but poor hover performance. The aerodynamic advantages of this configuration are balanced by higher demands on the batteries and on the power electronics during hover. Lilium Jet is an example of this configuration (Lilium, 2020). On the other extreme, the Multicopter configuration present larger rotor area and no wings. Hover efficiency of this vehicles is the best of all the types at the expense of limitations in the range. EHang(2020) is an UAM multicopter project. The last configuration seems to be closer to the market due to the lower complexity compared to the other types of vehicles. (Cestino and Bacchini,2019a) (Vertical Flight Society,2020) (Finger, F., Braun, C., Bil, C. 2017).

Therefore, trade-off between hover and cruise performance seems to be the main concern when choosing the configuration. The mission objective will define what configuration is the best to use.

3.4.2. Airframe design

Aston Martin's original concept is conceived as a canard aircraft. Therefore, characteristics associated to those aircraft were compared in this section.

First, an analysis of the MTOW against span, wing area and aspect ratio for different aircraft is shown in Figure 3.1. Table with the plotted values can be found in Appendix A. Limitations in the expected use of the aircraft in heliports will limit the span to a maximum of 10m, with the following limitations in aspect ratio. As observed, wing surface around 2000kg MTOW is between 15 and 20 m² and the aspect ratio ranges between 6 and 9, while span is slightly higher than the restrictions, from 10 to 13m.

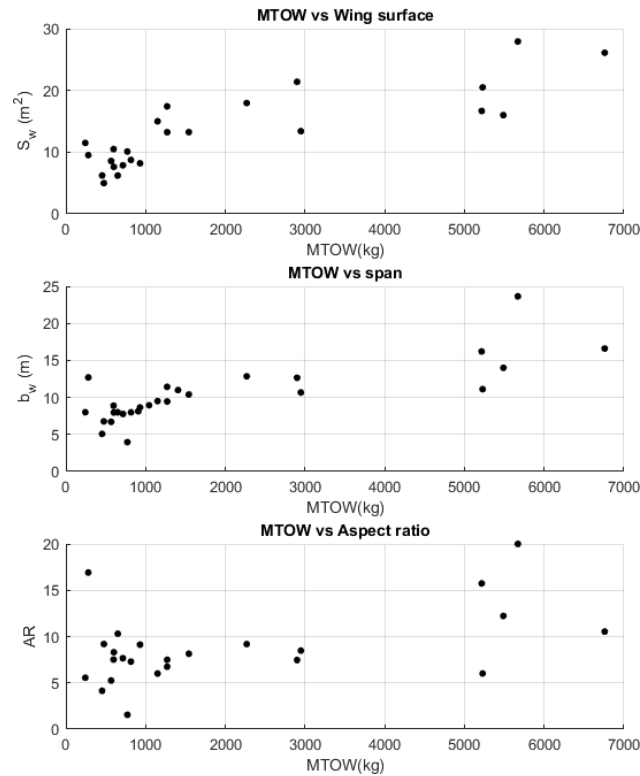


Figure 3.1: Canard aircraft wing area, wingspan and aspect ratio comparison as a function of MTOW.

3.4.2.1. Advantages respect to conventional aircraft

Canard aircraft present some aerodynamic advantages against conventional aircraft, although it must be stated that the interaction between components complicates the analysis, as the forward propellers are located between canard wing and main wing. Nevertheless, guidance from different authors regarding canard aircraft design is gathered below. This is accompanied by the positive and negative effects on performance when compared to conventional configurations.

First, a necessary condition for a proper canard aircraft design would be the canard to stall before the wing, as the opposite would lead to catastrophic stall characteristics. If wing stalls before the canard, the considerable loss of the positive pitching moment generated by the wing leads to a further increase in angle of attack and stall. The problem is that stall analysis is considerably complicated. Not only airfoil selection is involved but also three dimensional and interference effects are present, needing a whole integrated model to obtain acceptable results. For further study, lifting line theory provides a good match with experimental data for aspect ratios over 6 according to McVeigh and Kisielowski (1971).

Given the current design, two aspects must be further considered. First, given the characteristics of the aircraft, forward tilt rotors can be used to add further control into stall. Then, forward propellers slipstream could have positive effect on stall.

By adding further turbulence and energy into the boundary layer, stall can be delayed as seen on Jetstream 31 (Valdes et.al., 2019).

Therefore, two hard constrain implemented in the design related to stall: Forward canard wing root angle of attack must always be higher than the wing root angle of attack. Forward canard wing maximum camber must always be higher than the wing maximum camber.

It is widely known that the main advantage of the canard is that it contributes to lift generation when compared to a conventional aircraft where the horizontal tail generates negative lift. This leads to the aircraft flying at a lower angle of attack during cruise and, thus, reduced lift-induced drag. According to wind tunnel test data gathered by Yip (1985), it is confirmed that a lower angle of attack is required to generate the same lift as for conventional configuration. However, the elevator angle of attack required is higher for the same values of wing and canard surface. Due to the possibility of altering both canard and wing surfaces during the optimisation, this should not pose a problem. Otherwise, if the elevator is located on the canard, high cambered airfoils are recommended to neutralize this.

Another positive effect is the natural stall protection mechanism. As mentioned before, canard is designed so that the wing stalls before the canard to avoid undesirable stall characteristics. Moreover, this will provide a stall protection mechanism, with a negative pitching moment provided by the canard stall. For this 'stall protection' to be effective, canard stall should be gentle in order to avoid an abrupt pitch down moment. This is not always applicable as an abused stall entry due to a high rotational momentum would be still possible (Gudmundsson, 2013, p 496).

3.4.2.2. *Disadvantages respect to conventional aircraft*

Some of the drawbacks associated to this configuration are presented in this subsection.

Stall speed is higher relative to conventional configuration due to the canard stalling before the wing, limiting the maximum angle of attack. However, this requirement is less relevant for this aircraft as take-off and transition can be performed solely by the propeller thrust.

Due to the destabilizing moment generated by the canard, stability ($C_{m\alpha} < 0$) has to be maintained by pushing the cg backwards or distancing the mean aerodynamic chord from the CG adding sweep to the main wing. (Gudmundsson, 2013, p 495).

Additionally, interference effects further increase complexity in the design. The downwash effect of the canard wing reduces the effectiveness of the main wing and the lift produced by it. This may reduce the positive effect of the lift generation from the canard. This effect must be considered to maximize the efficiency of the configuration in terms of the stall margin. The wing stall is further delayed while

the canard practically maintains the same stall angle, reducing the maximum lift coefficient. Not only this, but lift distribution along the span is varied, modifying the wing stall behaviour, the Oswald efficiency factor and the structural loads. Propeller is also affected by this, resulting in possible efficiency and thrust variations (Gudmundsson, 2013, p 496-497).

The difference in Reynolds number between canard and main wing may be problematic as in the case of the Rutan Long-EZ aircraft. At low speed, the canard wing low chord value will cause a low Reynolds number as well. This may even result in differences in the type of flow. In the case of the Rutan aircraft, this leads to flow separation problems due to laminar flow. When designing the canard, it must be taken into account that, although increasing aspect ratio reduces induced drag and gives a steeper lift curve allowing for a smaller canard, the stall angle of attack is reduced. Not only this but the mentioned Reynolds effects are more pronounced in higher aspect ratio canards as the chord is smaller. Back sweep and higher taper ratio will reduce the lift curve slope as well but will tip load the canard and lower the stall angle of attack. All of these mechanisms can be used to control canard stall respect to the wing (Gudmundsson, 2013, Appendix C2).

3.4.3. Rotor design

Helicopters, tilt-rotors and tilt-wings have been present in the aerospace industry for a long time. One of the key aspects for hover efficiency is its direct relation with effective disk loading, as presented in Figure 3.2. Hover efficiency considerably increase for reduction in disk loading. This means that, for a constant weight, the larger the diameter of the rotors the more the efficiency during hover. Therefore, for applications where hover or transition stages are predominant, low disc loading is essential. Moreover, high disk loading is associated to higher noise levels. The drawbacks associated to lower disc loadings are related to the penalization in size, both of the rotor and of the structure to support it, and thus in weight (Finger, F., Braun, C., Bil, C. 2017) (Hubbard,2010).

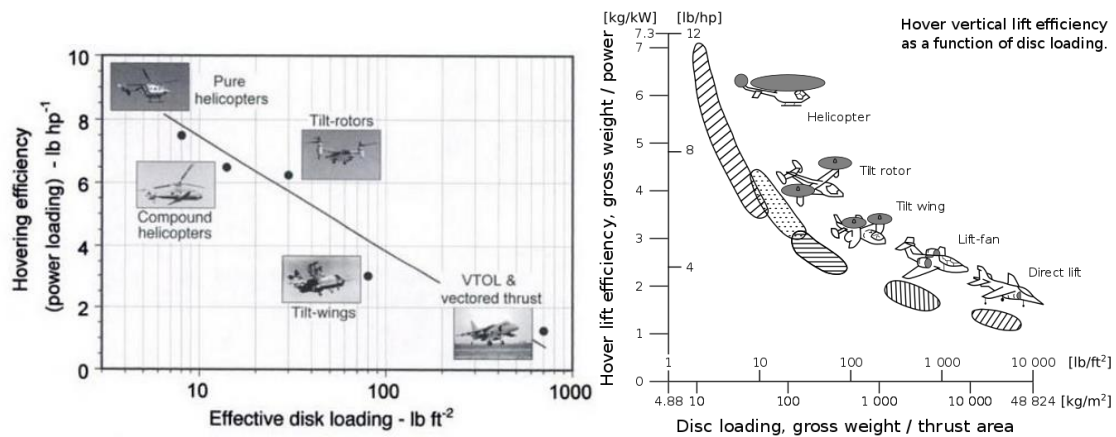


Figure 3.2: Disk loading comparison for different aircraft. Extracted from Leishman(2006), left, and Maisel, Giulianetti and Dugan(2000), right.

While forward propellers should present characteristics similar to general aviation propellers, back propeller is completely focused on hover performance. Therefore, some of the problems observed in conventional helicopter may be present on the back propeller.

Retreating blade stall may be a problem for this propeller at higher airspeeds. For this project, design is conceived so that the back propeller autorotates during cruise. Thus, retreating blade stall should not pose a problem.

Another relevant problem for larger diameter rotorcraft is noise levels. Vibration effects are one of the main sources of noise as it will be mentioned later. These effects do not become relevant until a significant portion of the rotor disk is above the critical Mach number. Usually a margin of 5% to 10% above the section critical Mach number can be tolerated. (Johnson, 2013, p283-284)

Issues like non-linearity, hysteresis of the lift curves and a dominant influence from the presence of the laminar separation bubble may arise at low propeller Reynolds number. In the range of $10^5 - 2 \cdot 10^5$, non-linearity and hysteresis of the lift curves to the laminar separation bubble may appear. For values above $2 \cdot 10^5$, these effects can be avoided since it is possible to make the transition occur upstream of the adverse pressure gradient (De Leeuw, 2013). This could lead to problems while defining the lift and drag aerodynamic curves on QPROP in the case of irregular shapes or 'buckets' formation. Expected propeller Reynolds number on this project are over $5 \cdot 10^5$ and. Even though Re varies depending on the radius, this effect seems non-relevant for full-scale propellers (De Leeuw, 2013). Thus, mentioned laminarity issues are expected to be non-consequential.

Borst (1973) provided some interesting recommendations for propellers design. For high values of disk loading, propellers with three or four blades will be able to operate near optimum efficiency points. However, for higher disk loading in conditions like vertical take-off, from six to eight blades would provide much better efficiency. Prioritizing structural and manufacturing objectives would result in high thickness ratios and low chord widths. For a given thickness ratio, the wider,

higher solidity blades generally have better strength characteristics than propellers with narrow blades. These blades are unsatisfactory and would produce high engine losses. In conventional propeller, non-optimal structural behaviour can be solved with special fairings installed on the blades.

4. Modelling

4.1. Aerodynamic modelling

In this section, the aerodynamic model will be introduced. The structure of the aerodynamic model will be described first, with the inputs and outputs from each block. Then, each of the tools used will be explained, with validation for each of them using Jetstream 31 wind tunnel data from Cooke(2019).

4.1.1. Aerodynamic model structure

Three different tools will be used for the aerodynamic parameters estimation. For a certain geometry at a certain flight condition, AVL will provide values on the aeroderivatives and the lift coefficients C_{L0} and $C_{L\alpha}$. Drag coefficients C_{D0} and K will be given by empirical estimation methods from Torenbeek(1998) and Rayner(1992).

For each of the blocks, flight conditions and geometry of the aircraft are inputted. The parameters required on each block will be explained in the following subsections. Forces, moments and aeroderivatives linearized about the defined flight condition at $\alpha = 0$ and $\beta = 0$ are provided as an output. Figure 4.1 presents a diagram with the structure of the aerodynamic model.

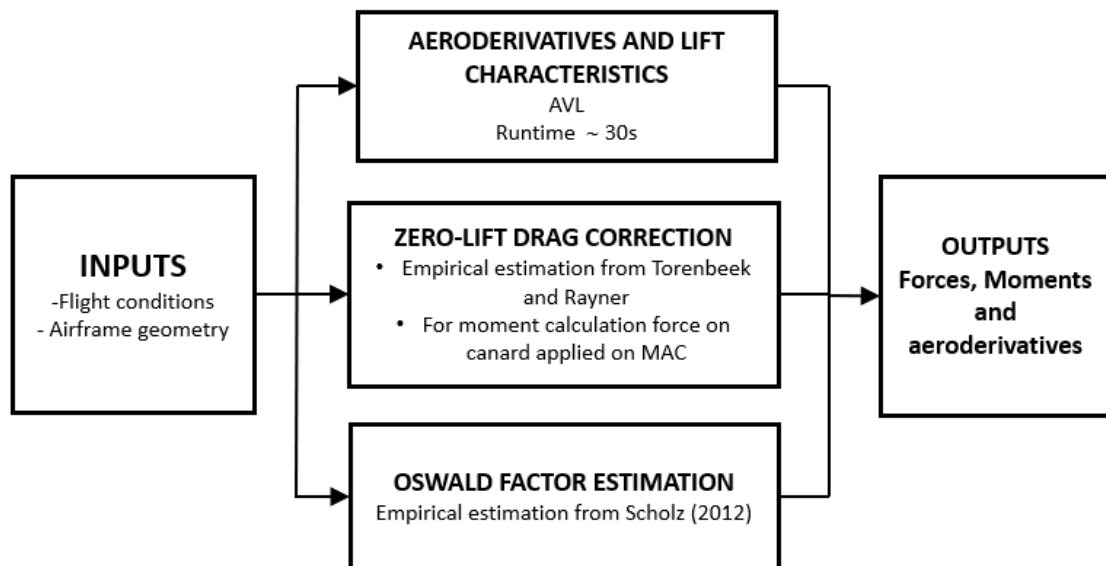


Figure 4.1: Aerodynamic model structure.

While modelling the airframe, some simplifications and assumptions have been made:

- Fuselage is modelled as a NACA 4421 with a plan area of 6x1.8m. Airfoil selection based on ergonomic criteria given by Gudmunsson(2013, p531-532). This will be fixed during the whole optimization process.
- Fins are modelled as a fully movable half wings and will be fixed during the optimization. Defined by $C_r = 0.4m$, $b = 0.8m$, $\Lambda = 15deg$ and located at the back of the fuselage, each of them at 0.9m from the centerline.
- Ailerons and elevator will be given as percentages of the chord and span of the wing and canard respectively. Elevator size (on the canard): From 10% to 90% of the span and 70% to 100% of the chord. Aileron size (on the wing): From 50% to 90% of the span and 70% to 100% of the chord.
- Airfoil is included as a 4-digit NACA with the maximum camber (3rd digit) fixed at the 30% of the chord for the sake of simplicity.
- No interference effects from propeller slipstream are modelled.
- Wings nor canard present no dihedral angle.

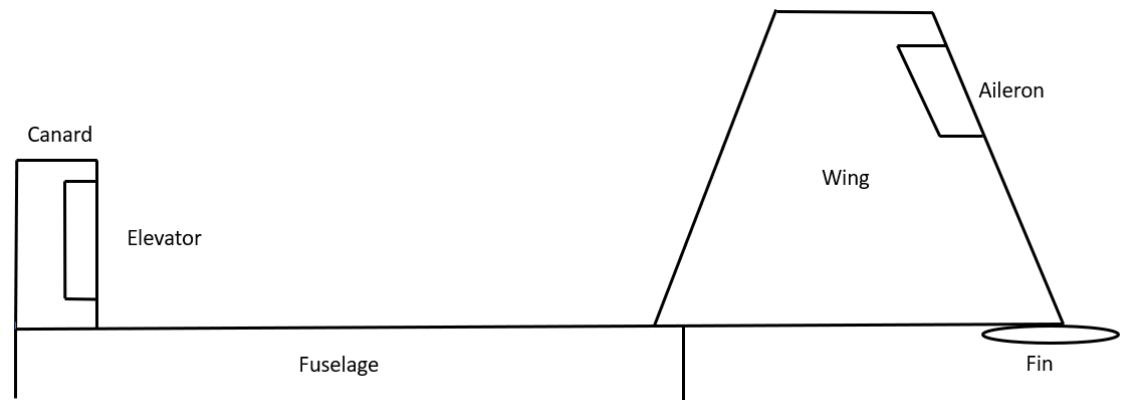


Figure 4.2: Airframe simplified plant geometry.

4.1.2. AVL

Athena Vortex Lattice AVL is a code written by Harold Youngren in 1988 based on different researchers work. Numerous revisions have been added by Mark Drela and Harold Youngren, converting the current software into something completely different from the original version. All the information from this section is based on work by Mark Drela and Harold Youngren(2017).

As a vortex-lattice method, AVL is suited for aerodynamic modelling of thin lifting surfaces at small angles of attack and sideslip. Surfaces and their trailing wakes are represented as single-layer vortex sheets, discretized into horseshoe vortex filaments whose trailing legs are assumed to be parallel to the x-axis.

The strength of each of the vortex sheets (per unit length in the x direction) is denoted by $\gamma = \gamma(x, y)$, which varies in the x and y direction in the same way as circulation Γ varies. These lifting lines are superimposed by the trailing vortices from the other lifting lines. This result in the formation of another vortex sheet of strength $\delta = \delta(x, y)$, which also vary in the y direction since the circulation about each lifting lines does so. These two vortices, the one with vortex lines running parallel to y with strength γ (per unit length in the x direction) and the other with vortex lines running parallel to x with strength δ (per unit length in the y direction), result in a lifting surface distributed over the entire planform of the wing, as presented in Figure 4.3 (Anderson, 2001).

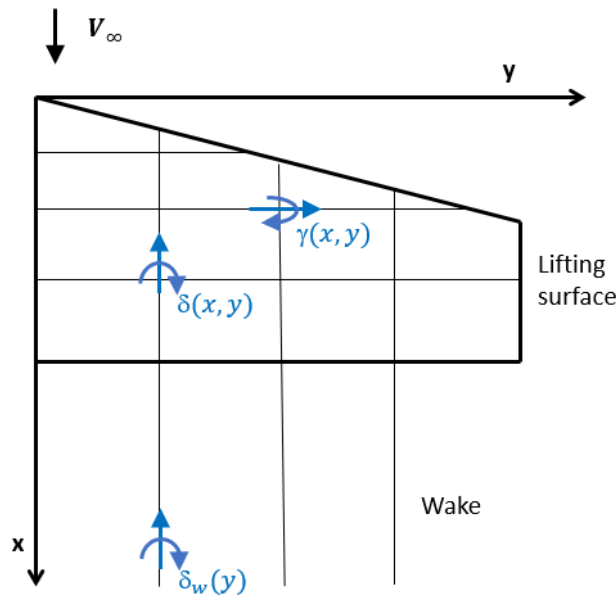


Figure 4.3: Vortex Lattice Method filament diagram. Adapted from Anderson(2001).

Flow tangency condition is that the sum of the induced $w(x, y)$ and the normal component of the freestream velocity must be zero at every point on the wing. Biot-Savart law is used to determine the induced velocity at any point by the vortex filaments. Integrating to account for the effects of all the filaments in the whole wing planform, induced velocity at each point is obtained. This is simplified by discretizing the domain and imposing the control point, where the induced velocities are calculated, at a distance of $1/4$ to the front of each panel. By imposing this flow-tangency condition and satisfying it for every point on the wing, Γ is obtained. With the circulation at each point of the surface known, lift distribution can be obtained (Anderson, 2001).

As these filaments are extended to the whole aircraft, interference and wake effects between surfaces are also included in the model. Furthermore, induced drag can be predicted using a Trefftz-plane wake trace integration in the Y-Z plane on the far-field.

Discretization of the geometry can follow different spacing distributions chord and spanwise. Cosine distributions with tighter spacing in wingtips and leading and trailing edges are recommended by Drela in the user guide. A sensibility analysis

was performed to look for the optimum value of panels in each direction that provide robust estimations.

AVL can model fuselages and nacelles, although experience with this model is stated to be limited. Nevertheless, this capability will not be used as the fuselage will be modeled as a blended wing body.

Vortex-Lattice methods assume quasi-steady flow, not considering unsteady aerodynamics, as well as small reduced frequency. The limits on these frequencies are the following:

$$\begin{aligned} -0.1 < \frac{pb}{2V} < 0.1 \\ -0.03 < \frac{qc}{2V} < 0.03 \\ -0.25 < \frac{rb}{2V} < 0.25 \end{aligned}$$

For the performance analysis and the expected manoeuvres in posterior flight control design, these limits will be respected. Low speed violent motions do not apply.

Compressibility is accounted by using Prandtl-Glauert correction. Flow is solved as incompressible and then correction is added to the solution. Wing sweep is also taken into account for this correction. Assumptions for this correction are irrotationality and linearization about the freestream. This correction proves to be valid until reaching a Mach of 0.7, far above the maximum expected Mach for this project, around 0.35.

Main limitation of this software is on the lack of modelling of viscous effects. Lift slope of the section airfoil is defined as 2π , although a thickness correction can be added manually. Additionally, if section properties are known they can be inputted into the software. Combination of viscous 2D solvers with AVL could potentially enhance predictive capabilities. However, as It will be discussed later with propeller modelling with QPROP, this way of defining aerodynamic curves are somewhat arbitrary, especially at lower Reynolds.

Modelling of the aircraft is performed by dividing the aircraft into surfaces. Each surface can then be defined by different sections along its span. Airfoil discrete variation is allowed by defining a different airfoil, as well as relative angle/twist distributions, for each section. Changing the twist angle only modifies the flow tangency boundary condition on the airfoil camber line. Furthermore, control surfaces can be defined within sections, with its size given as a relative percentage of the chord.

As the outputs, many different options are available with AVL. However, for the current project only the forces and moments coefficients and the aeroderivatives will be used.

4.1.3. AVL Validation

As explained by Peerlings(2018), validation data on this software is scarce. Due to the lack of viscous effects modelling, drag and lift underprediction is expected. However, to gain insight into how big discrepancies are, a validation will be performed.

Dantsker and Vahora(2018) compared XFLR5, AVL and Ansys Fluent results with flight test data for a 62.5m wingspan Great Planes Avistar Elite model unmanned aircraft at 16m/s. XFLR5 results showed a better agreement with flight test data than AVL, probably due to the inclusion of viscous effects. Difference with flight test data became considerably more important for drag estimations, while lift fell within the same order of magnitude. However, relevant different may be explained by the fact that simulations were made without accounting for slipstream effects.

	AVL	XFLR5	Ansys Fluent	Flight Test
C_{L0}	0.3309	0.3575	0.3875	0.5345
$C_{L\alpha}$	0.0810	0.0827	0.0667	0.0606
C_{D0}	0.00633	0.02028	0.05512	0.0489
$C_{D\alpha}$	0.0043	0.0075	0.0067	0.0237
C_{M0}	-0.06364	-0.00799	-0.00659	-
$C_{M\alpha}$	-0.0193	-0.0249	-0.0340	-

Table 4.1: Aerodynamic coefficients results from Dantsker and Vahora(2018).

Further validation of AVL is done against wind tunnel data for a 1:6 scale full aircraft from Cooke's Flight Test report (2019). Tests were performed at a Mach of 0.18 and Reynolds of $1.8 \cdot 10^6$, with free transition on wing and fixed transition on the nose, canopy and nacelles and at 0.05c on tail and fin. Transition on the wing occurred at approximately 65% of the chord. Propellers were not included and, therefore, neither slipstream effects.

Aircraft geometry was obtained from the Jetstream 31 Datapack (Cooke, 2013), accounting for the 1:6 scale effects. Fuselage was not included in the simulation, but its effect was accounted for by the corrections included in the Datapack (Cooke, 2013). As recommended by Drela and Youngren(2017), wing was connected if fuselage was not added. Flight conditions file was set up to match the conditions described in the paragraph above. Resultant geometry is presented in Figure 4.4.

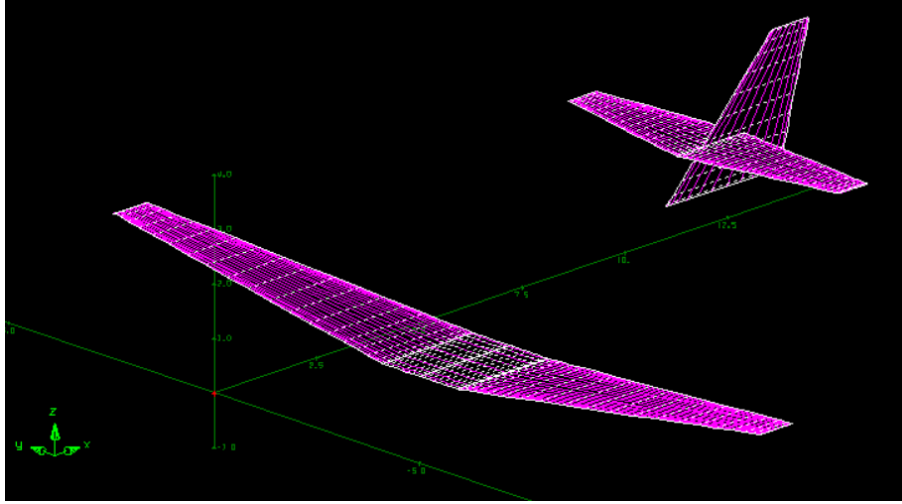


Figure 4.4: Jetstream 31 geometry implemented in AVL.

Fuselage and nacelles corrections from Jetstream 31 Datapack(Cooke, 2013) were introduced to account for these missing elements in AVL: Fuselage and nacelles normal force correction from section 2.3. Drag areas $\frac{D_0}{\bar{q}}$ from Section 3.3 and Table 3.1 in the Datapack.

Furthermore, a thickness correction to account for the effect of increasing lift coefficient slope due to thickens was added. Defined by AVL as $C_{L\alpha} = 2\pi$, new lift slope extracted from Cook(2012, p329) is:

$$C_{L\alpha} = 2\pi \left(1 + 0.8 \frac{t}{c} \right) \cos(\Lambda_{le}) \text{ (rad}^{-1}\text{)}$$

Comparisons with the wind tunnel data are presented in Figure 4.5 and Table 4.2. No correction stands for the results obtained by AVL without corrections. Thickness represents the correction by Cook. Fus the fuselage and nacelles corrections from the Datapack. Fus+Thickness the combination of the last two. WT are the wind tunnel results.

Even with the corrections, AVL underestimates C_{D0} by a 25%. However, it can be seen that the practically all comes from the fuselage correction. Therefore, estimations of this parameter cannot be used for performance analysis. However, K value is overestimated by a 34% with the corrections, being able to use it as a conservative estimate.

Regarding the lift coefficients, both intercept and slope are underestimated by a 9% and 8.5% respectively. For $C_{L\alpha}$, estimations can be considered accurate given the current stage of design and the fact that fuselage influence is almost neglectable on this term. However, C_{L0} may be prone to an increased error, as the lack of viscous effects will affect the fuselage as well on the UAM vehicle simulation. Nevertheless, expected error can be considered as acceptable for both coefficients.

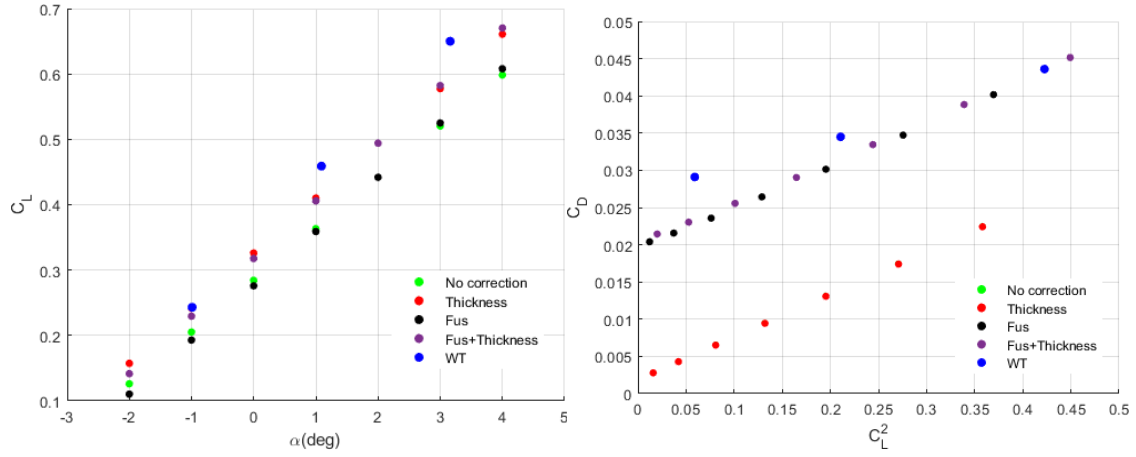


Figure 4.5: Graphical representation of the aerodynamic coefficients for Jetstream 31 validation results.

	AVL no correction	Fuselage	Thickness	Fuselage+Thickness	Wind tunnel
C_{L0}	0.0788	0.0830	0.0839	0.0881	0.0963
$C_{L\alpha}$	0.284	0.2760	0.3258	0.3177	0.3448
C_{D0}	0.0019	0.0195	0.0024	0.0201	0.0262
K	0.0574	0.0573	0.0555	0.0554	0.0414

Table 4.2: Specific values for the aerodynamic coefficients for Jetstream 31 validation results.

As a result of the validation, it has been determined that drag related coefficients C_{D0} and K were prone to larger errors than lift coefficient ones using AVL. K can be acceptable with the 30% expected error, but C_{D0} expected value is 1 order of magnitude lower than the real results. Both lift coefficients terms seem acceptable.

4.1.4. Empirical C_{D0} estimation

Given the underestimation around 1 order of magnitude of C_{D0} using AVL, an alternative was needed. This section will present the two methods that were used for C_{D0} determination. Initially, a 2D viscous drag correction using XFOIL was implemented. However, this resulted in excessive drag values, around 0.045. Thus, an empirical estimation was used as the method to obtain C_{D0} .

This empirical method is based on the work of various researchers. Fuselage is modelled as a wing as mentioned.

$$C_{D0} = C_{D0w} \frac{S_{wetw}}{S_{ref}} + C_{Dc} \frac{S_{wetc}}{S_c} + C_{D0fus} \frac{S_{wetfus}}{S_{ref}} + C_{D0fin} \frac{S_{wetfin}}{S_{ref}}$$

To obtain the wetted area of each of the components S_{wet} , the formula is extracted from Torenbeek(1998):

$$S_{wet} = 2S_{exp} \left(1 + 0.25 \left(\frac{t}{c} \right)_r \frac{1 + \tau\lambda}{1 + \lambda} \right)$$

Where S_{exp} is the exposed wing area, $\left(\frac{t}{c} \right)_r$ the thickness at the root, λ the taper ratio and τ the ratio of tip and root relative airfoil thicknesses $\frac{\left(\frac{t}{c} \right)_t}{\left(\frac{t}{c} \right)_r}$.

The zero-lift drag of each individual component C_{D0c} (c stands for each component 'c') is defined by Raymer(1992, p281-283) as:

$$C_{D0c} = C_{fc} FF_c Q_c$$

Where C_{fc} is the skin friction drag coefficient of the component, FF_c is the form factor of the component and Q_c the interference factor.

The skin friction drag coefficient is defined as the skin friction experienced by a flat plate. Its value depends on Reynolds number, Mach number and skin roughness. Given the low Reynolds number and the current advances in laminar flow technology, a 60% of the flow is assumed as laminar in the canard, $k_{laminar_c} = 0.6$. For the wing, due to interference effects and turbulent slipstream from the propeller, a 30% of laminar flow is chosen as a conservative prediction. Selected values for the other components are 30% of laminar for the fuselage according to guidance by Raymer(1992, p282) and a 60% for the fins due to its low chord.

The value for the laminar skin friction drag coefficient $C_{f_{laminar}}$ is given by:

$$C_{f_{laminar}} = \frac{1.328}{\sqrt{Re}}$$

The value for the turbulent skin friction drag coefficient $C_{f_{turbulent}}$ is given by:

$$C_{f_{turbulent}} = \frac{0.455}{(\log_{10} Re)^{2.58} (1 + 0.144M^2)^{0.65}}$$

And the total skin friction drag coefficient for each component C_f will be given by:

$$C_f = C_{f_{laminar}} k_{laminar} + C_{f_{turbulent}} (1 - k_{laminar})$$

The form factor estimates pressure drag of the component due to viscous effects. Given by:

$$FF = \left[1 + \frac{0.6}{\left(\frac{x}{c} \right)_m} \left(\frac{t}{c} \right) + 100 \left(\frac{t}{c} \right)^4 \right] [1.34M^{0.17} \cos^{0.28}(\Lambda_m)]$$

Where $\left(\frac{x}{c}\right)_m$ is the chordwise location of the airfoil maximum thickness point, averaged as the mean of the root and the tip values. Λ_m is the sweep of the maximum thickness line.

Finally, the interference factors will only be included for the wing. An interference factor of $Q_w = 1.04$ is included to account for the interference on the wing caused by the canard.

Skin roughness effects are not accounted in this estimation. Nacelles or propeller interference effects are neither included here. Maximum camber effect is neither included, which will affect the optimization results, always tending to the maximum camber value.

4.1.5. Empirical K estimation

Another empirical correction, this time of K was tested and validated against Jetstream 31 data. Method was obtained from Scholz(2012) and makes use of statistical aircraft data to account for geometrical parameters and fuselage, zero-lift drag and Mach influence. Aircraft types and missions used for this analysis are varied.

Defining K as:

$$K = \frac{1}{\pi AR e}$$

This paper gave a calculation method for the Oswald efficiency factor e :

$$e = e_{theo} k_{e,F} k_{e,D_0} k_{e,M}$$

The e_{theo} accounts for the coupling between taper ratio and sweep angle and its relation with elliptical loading.

$$e_{theo} = \frac{1}{1 + f(\lambda - \Delta\lambda)AR}$$

$$\Delta\lambda = -0.357 + 0.45 e^{0.0375\Lambda_{25}}$$

Where Λ_{25} is the sweep of the 25% chord line.

$$f(\lambda) = 0.0524\lambda^4 - 0.15\lambda^3 + 0.1659\lambda^2 - 0.0706\lambda + 0.0119$$

$k_{e,F}$ accounts for the fuselage of the aircraft. As conservative value of 0.118 is chosen according to guidance from the author.

k_{e,D_0} is an statistical factor that accounts for the change of Oswald factor based on zero-lift drag. Chosen as 0.804, again the most conservative value and the used in general aviation.

$k_{e,M}$ includes compressibility effects. For Mach below 0.4, it is negligible and therefore is eliminated.

This correction was validated against Jetstream 31 data, including the dihedral angle. Error in the estimation was below 8% with the wind tunnel data. Therefore, the decision to adopt this method was taken, as it looked more promising than AVL results.

The problem with this method is the lack of influence of the airfoil used, the twist angle nor any parameter on the canard. During the optimization, this will translate into twist angles of 0deg and maximum camber tending to the maximum possible.

4.2. Mass distribution and inertia calculation

For the sake of posterior handling qualities analysis with this aircraft, inertia properties are needed. It is therefore necessary to connect the changes in the aircraft configuration with the inertia properties. At conceptual design stage, uncertainty in the components location will be large and methods based on geometrical analysis seem suitable. Mass distribution is defined with the help of Cranfield's Flight Dynamics group estimations and traditional aircraft data. Inertia model is based on Lanham(1979) work, which will be validated against Jetstream 31 data.

4.2.1. Mass distribution

Mass distribution is defined with guidance from Lanham(1979), Gudmundsson(2013) and the design specifications accorded by Cranfield Flight Dynamics group.

The initial estimation of mass of each relevant group in the aircraft was determined by the Flight Dynamics group from Cranfield University:

	Passengers	Systems	Propulsion	Airframe	Propellers	Battery	Total
Mass(kg)	300	200	200	800	100	400	2000

Table 4.3: Mass distribution along aircraft groups.

From Lanham(1979) the following mass distribution of the systems is expected in military aircraft. This project configuration can be considered more similar to military than passenger aircraft.

Systems distribution					
	Hydraulics (%)	Electrical (%)	Electronics (%)	Air conditioning (%)	Control Surface (%)
Fuselage	67	75	100	100	46
Wing	0	0	0	0	19
Canard	0	0	0	0	11
Fin	0	0	0	0	25
Engine	33	25	0	0	0

Table 4.4: Systems distribution for conventional military aircraft. Extracted from Lanham(1979).

However, this distribution should be adapted to the fact that wings do not contain fuel inside, therefore allowing for a higher percentage of the systems weight.

Final mass distribution is described in Table 4.5. Furthermore, an approximation of the CG position calculation is included. This calculation changed every time the design was modified. During the optimization, an interval of $\pm 0.4\text{m}$ was defined as the possible variation of the CG. For the final configuration, CG estimation yielded 4.81m .

	Volume (m³)*	Mass (kg)	Systems Weight percentage (%)	Systems Weight (kg)	Total mass (kg)	CG Longitudinal (m)**
Airframe						
Fuselage	10.2	636	60	180	816	4
Wing	2.2	138	30	90	228	8
Canard	0.4	22	5	15	37	0.5
Fin	0.02	3	5	15	18	9.5
Point masses						
Pilot					100	3
Passengers					200	4.3
Battery					400	5.4
Powerplant Forward					150	2
Powerplant Backward					150	8

Table 4.5: Mass distribution for the whole aircraft.

*Volume defined as planform surface multiplied by maximum thickness.

**CG is approximated based on the diagram of the aircraft, it varies for each different configuration.

4.2.2. Inertia calculation

With the mass allocated, inertia can be obtained with the inertia model extracted from Lanham (1979). Lanham derived a series of equations from a geometric simplification of the different components in the aircraft. Given the current level of detail in this stage of design this method seemed appropriate and sensible for the level of information available.

The inertia matrix of each component is calculated about its own centroid with the formulas extracted from Lanham(1979). Then, inertia matrix about aircraft CG is calculated by transferring each component to the CG with Steiner's theorem.

Components of the aircraft can be modelled as surfaces, fuselage or point masses. As the fuselage is modelled as a 'wing', the whole airframe is modelled as surfaces. Figure 4.7 shows the simplified representation of these surfaces in manufacturer axis (x_{man} starting at the nose of the component and going backward, y_{man} to the right, z_{man} upwards).

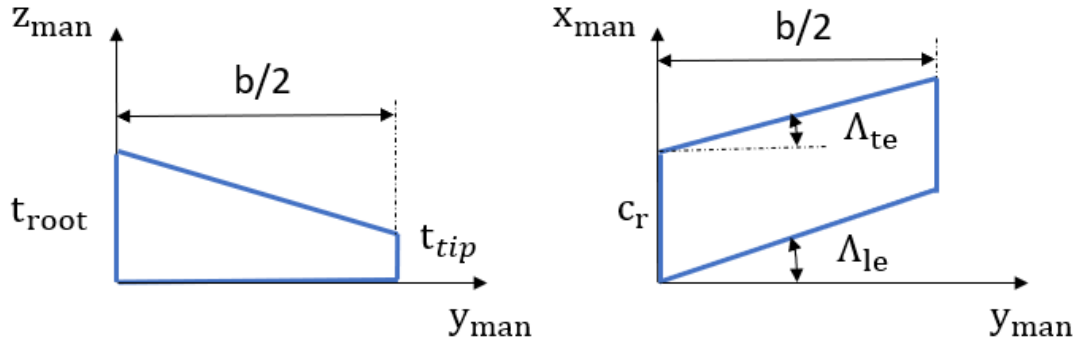


Figure 4.6: Diagram representing the simplified surfaces for inertia calculation.

Equations are derived for a trapezoidal panel with the thickness varying linearly from root to tip. Thickness is assumed constant from leading to trailing edge equal to the maximum of that section. Only exposed area of each surface will be taken into account for this model simulation. Resultant equations without including dihedral effect are:

$$I_{xx} = \frac{Wb^3}{V} \left[(t_{root} - t_{tip}) \left(\frac{c}{4} + \frac{btan(\Lambda_T)}{5} - \frac{btan(\Lambda_L)}{5} \right) + t_{root} \left(\frac{c}{3} + \frac{btan(\Lambda_T)}{4} - \frac{btan(\Lambda_L)}{4} \right) \right]$$

$$I_{yy} = \frac{Wb}{V} \left\{ t_{root} \left(\frac{c^3}{3} + bctan(\Lambda_T) \left(\frac{c}{2} + \frac{btan(\Lambda_T)}{3} \right) + \frac{b^3}{12} (\tan^3(\Lambda_T) - \tan^3(\Lambda_L)) \right) \right. \\ \left. - \left[(t_{root} - t_{tip}) \left(\frac{c^3}{4} + bctan(\Lambda_L) \left(\frac{c}{3} + \frac{btan(\Lambda_T)}{4} \right) \right) \right] \right. \\ \left. + \frac{b^3}{15} (\tan^3(\Lambda_T) - \tan^3(\Lambda_L)) \right\}$$

$$I_{zz} = I_{xx} + I_{yy}$$

$$V = b \left\{ t_{root} \left[c + \frac{b}{2} (\tan(\Lambda_T) - \tan(\Lambda_L)) \right] \right. \\ \left. - (t_{root} - t_{tip}) \left[\frac{c}{2} + \frac{b}{3} (\tan(\Lambda_T) - \tan(\Lambda_L)) \right] \right\}$$

Where W is the weight and V the volume.

Next, centroid position from the leading edge (X_C, Y_C) for each component is determined. Z component is negligible due to small thickness of surfaces compared with their length and span.

$$X_C = \frac{-c_a^2 + c_b^2 + c_b c_c + c_c^2}{3(c_b + c_c - c_a)} \sqrt{k_0}$$

Where c_a , c_b and c_c are respectively the smallest, intermediate and largest values from: $[c, btan(\Lambda_L), btan(\Lambda_L) + c]$. k_0 is 0.703 for a wing and 0.771 for canard and vertical tail.

$$Y_{CG} = \frac{b^2}{V} \left[t_{root} \left(\frac{c}{2} + \frac{b}{3} (\tan(\Lambda_T) - \tan(\Lambda_L)) \right) - \frac{(t_{root} - t_{tip})c}{3} \right. \\ \left. + \frac{b}{4} (\tan(\Lambda_T) - \tan(\Lambda_L)) \right]$$

With the inertia about its own centroid for each component and its centroid position, inertia matrix about the CG can be calculated for the whole aircraft using the Parallel Axis Theorem for each component. With it, inertia about each component is translated to the CG and added up, obtaining the inertia matrix used within Simulink model.

$$I = \begin{bmatrix} I_{xx} & -I_{xy} & -I_{xz} \\ -I_{xy} & I_{yy} & -I_{yz} \\ -I_{xz} & -I_{yz} & I_{zz} \end{bmatrix}$$

4.2.3. Inertia model validation

Validation is performed again using Jetstream 31 Datapack data(Cooke, 2013) for the wing. Geometric characteristics and an estimation of the wing mass properties of the aircraft are extracted. Using the geometry from this source, a wing is modelled following the inertia model extracted from Lanham (1979).

b	15.85m
t_{root}	0.4279m
t_{tip}	0.09504m
c_r	2.377m
Λ_{le}	10deg
Λ_{te}	-22deg

Table 4.6: Geometric properties extracted from Jetstream 31 Datapack(Cooke,2013)

To include dihedral angle effect on the inertia matrix, the following equations are included:

$$I_{xx} = I_{xx_{straight}}$$

$$I_{yy} = I_{yy_{straight}} \cos(7deg) + I_{zz_{straight}} \sin(7deg)$$

$$I_{zz} = -I_{yy_{straight}} \sin(7deg) + I_{zz_{straight}} \cos(7deg)$$

The obtained results are presented in the table below. Considerable differences are observed, with at least 1 order of magnitude between results. Geometry simplifications included in the model are not the only explanation for these discrepancies, as neither the systems, the fuel tanks nor the structural distribution across the wing is known for the Jetstream 31. In the model, the total wing mass of 2090 lb is assumed to be evenly distributed across the wing depending on the local thickness and chord. This is not true, as the 2090lb includes systems and tanks distribution, which should be established as additional mass points. This can be confirmed by the position of the centroid, located way closer to the leading edge that the correspondent to uniform mass distribution.

	I_{xx} (lb.in ²)	I_{yy} (lb.in ²)	I_{zz} (lb.in ²)	X_c from le (m)
Datapack	$3.28 \cdot 10^7$	$2.15 \cdot 10^5$	$3.27 \cdot 10^7$	0.834
Inertia model	$3.67 \cdot 10^8$	$7.84 \cdot 10^6$	$3.76 \cdot 10^8$	1.5

Table 4.7: Validation of inertia model against Jetstream 31 data for the wing.

Considering the UAM vehicle evaluated in this project lacks fuel tanks in the wings, the assumption of mass distributed evenly across the wing does not seem inappropriate.

Additionally, the final configuration of this Urban Air Mobility project is evaluated against validated Fokker 100 data extracted from Mutluay(2015). To evaluate results for different aircraft, non-dimensional inertia matrix values, divided by mass and wing surface, are studied. Results yielded values within the same order of magnitude except for I_{xy} , whose importance can be considered as negligible when compared to the other terms.

	$\frac{I_{xx}}{S_w mass}$	$\frac{I_{yy}}{S_w mass}$	$\frac{I_{zz}}{S_w mass}$	$\frac{I_{xy}}{S_w mass}$
Fokker 100	0.06	0.39	0.43	0.002
UAM model	0.04	0.13	0.16	0.02

Table 4.8: UAM vs Fokker 100 non-dimensional inertia values comparison.

Mass distribution and inertia calculation present questionable accuracy. For the current stage of development these uncertainties can be assumed. However, if more detailed an accurate data is wanted, a whole mass and inertia module with more complex methods should be introduced in the model.

4.3. Propeller model

Propellers modeling will be described in this section. QPROP, the software used for this purpose will be explained first, along with the limitations associated to its use. Then, the ESDU(2006) correction to account for propeller angle of attack will be included.

It must be noted that counter-rotating propellers will be modelled as a conventional propeller assuming the number of blades is equal to the number of blades in the two stages. This simplification may yield an underestimation in efficiency from 8 to 10% (Borst, 1973).

The geometry needed for QPROP is defined by a piecewise spline distribution pchip through 4 different points: 10%, 35%, 70% and 100% of the tip radius. The first point of the blade at 10% of the tip radius is selected to account for the hub. Airfoil is included as a 4-digit NACA with the maximum camber (3rd digit) fixed at the 30% of the chord for the sake of simplicity. Thus, four distributions must be defined: Chord, pitch angle, maximum camber and maximum thickness.

4.3.1. QPROP theory

QPROP is an analysis software for predicting propeller performance. Model is based on an advanced blade-element/vortex formulation that includes self-induced velocity, which allows for heavy disk-loaded consistent predictions. All

the theory summarized here can be found in Drela's QPROP formulation guide (2006).

Velocity decomposition including the induced velocities is presented in Figure 4.8. v_a and v_t will be positive for a propeller with positive thrust and torque. These induced velocities will be considerably relevant at lower airspeeds. Externally-induced velocity u_t will be negative if it comes from an upstream counter-rotating propeller.

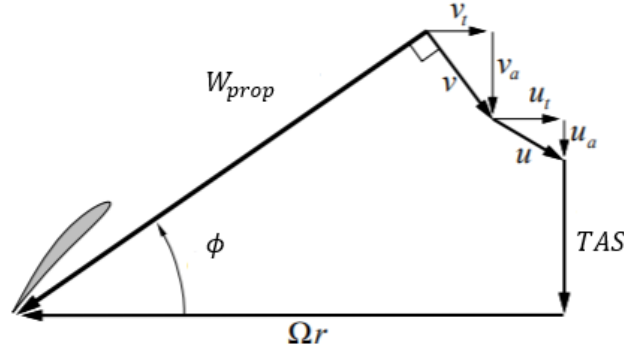


Figure 4.7: Propeller blade velocity decomposition at a certain radial location r . Adapted from Drela(2006)

$$W_a = TAS + u_a + v_a$$

$$W_t = \Omega r - u_t - v_t$$

$$W_{prop} = \sqrt{W_a^2 + W_t^2}$$

Swirl v_t is calculated by relating the torque provided by the rotor with the circulation on the rotor blades with the Helmholtz's Theorem. Biot-Savart integration used in the Vortex-Lattice-Method is substituted by empirical relations in order to simplify calculations. By using the empirical corrections, Goldstein's circulation distribution is assumed. Developing these conditions, a relation between local circulation and local tangential induced velocity is obtained.

$$v_t = \frac{B\Gamma}{4\pi} \frac{1}{F \sqrt{1 + \left(\frac{4\lambda_w R}{\pi B r}\right)^2}}$$

Where F is the modified Prandtl's correction factor to account for tip losses.

The local angle of attack defined by the blade section at a radius r is given by the following diagram and equation:

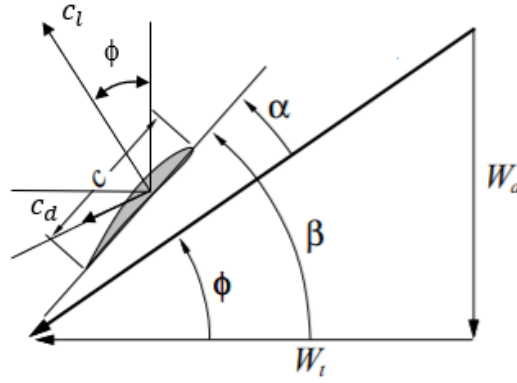


Figure 4.8: Propeller blade velocity triangle and forces at a radius r . Adapted from Drela(2006)

$$\alpha_{prop}(r) = \beta_{prop} - \arctan\left(\frac{W_a}{W_t}\right)$$

Lift coefficient is different depending on the location along the radius, as not only effective angle of attack changes but also Reynolds and Mach vary. Therefore, the circulation at each radius will vary:

$$\Gamma = \frac{1}{2} W_{prop} c c_l(\alpha_{prop}, Re, M)$$

Newton's iterative scheme is used to calculate the required circulation at each radius by solving the nonlinear equations described in the theory document (Drela,2006). Convergence is really fast, as confirmed by the low running time for a single evaluation, less than 0.1s. Once converged, thrust and torque are obtained by integrating lift and drag along all the blade and applying angular conversions.

4.3.2. Limitations

The main causes of inaccuracy for QPROP will be discussed in this subsection. First, the way aerodynamic properties of the airfoil are inputted will be treated. Then, low advance ratio errors during validations and stall will be linked. Finally, transonic issues will be discussed.

QPROP allows the user to introduce the airfoil at each section by inputting their aerodynamic properties. The problem comes in the way they are defined, presented in Figure 4.10. Lift coefficient curve is defined by the intercept at 0deg, the lift slope and the maximum lift coefficient of the linear region; CL_0 , $\Delta CL/\Delta\alpha$ and $(\Delta\alpha, CL_0 + \Delta CL)$ in the figure. When angle of attack is inside the linear region, lift coefficient is determined by the linear fit calculation. For angles outside that region, QPROP computes the value based on empirical approximations. Then, drag is calculated by defining a parabola that passes through 3 points: the minimum drag coefficient ($CD_0, CLCD_0$) and two points that define the equivalent

linear region of the CL^2 vs CD curve, $(CD0 + \Delta CD_{upper}, CLCD0 + \Delta CL_{upper})$ and $(CD0 + \Delta CD_{lower}, CLCD0 - \Delta CL_{lower})$.

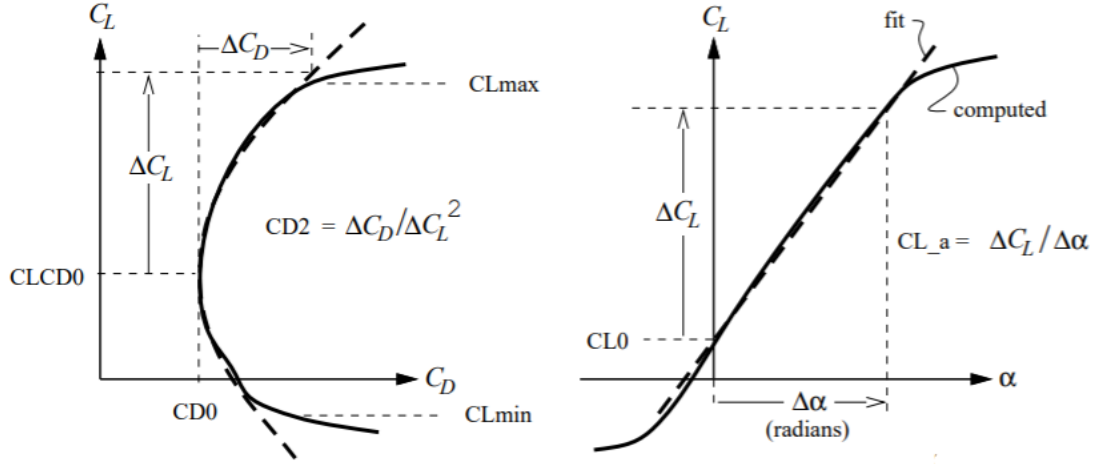


Figure 4.9: Aerodynamic coefficients curves definition on QPROP. Extracted from Drela(2005).

The problem with this method is the arbitrary character of these curves definition. Depending on the airfoil, the decision of the points to choose may not be straightforward. As it was stated by De Leeuw(2013), different authors define different values for the same airfoil. Even if small, these perturbations cause estimation errors.

In the case of this project, an automated algorithm that extracted the curves from XFOIL was used. This algorithm performed a linear fit for a low angles interval $[-2\text{deg}, 2\text{deg}]$ of the lift coefficient curve and extracted the slope and the intercept at 0deg . The maximum lift coefficient for the linear region was chosen as the point where the difference between the linear fit and the XFOIL values exceeds a 10% of the linear fit value at that angle. A similar procedure was defined for the CL^2 vs CD curve, determining the three points mentioned before.

Even with an automated algorithm, uncertainty and errors in the curves definition can be expected. Furthermore, errors associated to using XFOIL instead of wind tunnel data will further increase inaccuracy.

Moving to stall problems, QPROP has an empirical correction for the lift coefficient and an additional term added to the drag when lift coefficient is determined to be inside the stall region.

$$CD_{stall} = 2 \sin^2 \left(\alpha - \frac{CLCD0 - CL0}{\frac{\Delta CL}{\Delta \alpha}} \right)$$

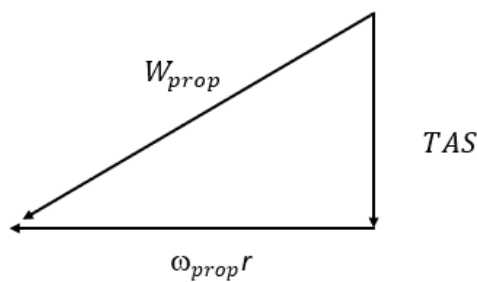
Therefore, considerable errors can be expected for stalled blade regions. As mentioned in the literature review, De Leeuw(2013) and Dimchev(2012) provided evidence of the inaccuracy of QPROP at low advance ratios, where airspeed is low. At this condition, effective propeller angle of attack is higher as the induced

angle ϕ is reduced as the airspeed decreases. Therefore, stalled regions along the blade increase in size and cause divergence between QPROP and experimental results.

However, there is one factor that should be considered for this aircraft. Forward propellers will be optimized both for hover and cruise condition. Therefore, pitch angle and effective propeller angle of attack will be lower than for propellers used in conventional aircraft.

Propeller tip speed is another aspect to consider as a limitation, as QPROP does not include transonic effects modelling capabilities and noise levels would be negatively affected. Therefore, upper bounds on the propeller rpm could be implemented to comply with transonic limitations, but before it is necessary to decide on this upper bound. Different authors establish transonic region limits from M above 0.7 to 0.8 depending on the propeller (Johnson, 2013) (Gudmundsson, 2013), but for accurate propeller selection a transonic regime analysis tool should be included in the optimization.

At the current stage of this project, one of the options available is to include constrains in the optimization by establishing upper bounds on the propeller angular velocity. As a first approximation and without considering swirl effects, Mach number can be limited by establishing an upper bound on propeller rotation speed as a function of M, speed of sound a, tip radius and true airspeed TAS.



$$M = \frac{\sqrt{TAS^2 + (\omega_{prop} r)^2}}{a}$$

$$\omega_{prop} < \frac{\sqrt{M_{lim}^2 a^2 - TAS^2}}{r_{tip}}$$

Figure 4.10: Simplified propeller velocity diagram.

$$W_{prop} = \sqrt{TAS^2 + (\omega_{prop} r)^2}$$

Depending on the Mach limit defined, different boundaries will be established, as in the figure below. Thus, boundaries will vary with flight condition, altitude and propeller size.

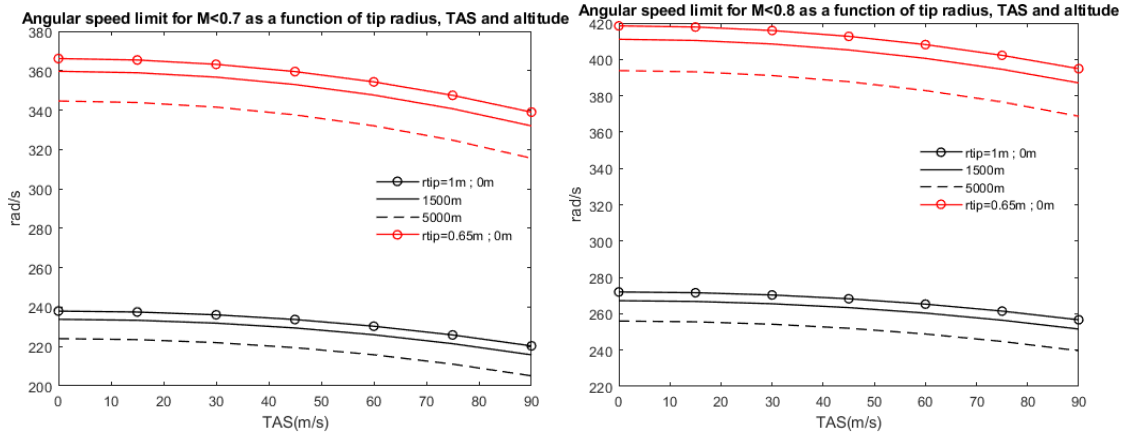


Figure 4.11: Rotational speed limits as a function of airspeed, altitude and propeller diameter for $M < 0.7$ (left) and $M < 0.8$ (right) constraints.

4.3.3. Propeller angle of attack correction

ESDU 89047(2016) correction provides a semi-empirical method for estimating forces and moments at low forward speeds. Validation is provided for up to $M=0.15$ (ESDU,2016). However, correction has been used for modelling of the Jetstream 31 by Cooke(2013), whose operational speed is higher than the expected for this project. Regarding the limits of propeller angle of attack, validity of the method is expected up to $\pm 20^\circ$.

This correction estimates the time-averaged forces and moments caused by changes in propeller loading due to incidence angles. As counter-rotating propellers are used in this project, moments will be cancelled. Resultant forces and moments are defined in Figure 4.13 along with their signs criteria. Too negative C_T will cause inapplicability of the correction due to irrational numbers.

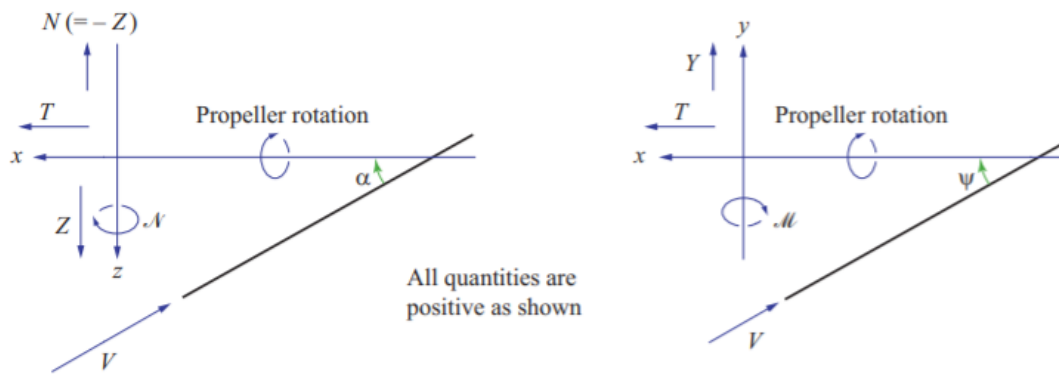


Figure 4.12: Propeller corrections for angle of attack and sideslip. Extracted from ESDU 89047(2016).

$$\frac{dC_N}{d\alpha_{prop}} = -\frac{dC_Z}{d\alpha_{prop}} = \frac{dC_Y}{d\beta_{prop}} = \frac{3.86\sigma}{1+\sigma} \sin(\beta_{75}(\text{deg}) + 9) \left[\frac{\pi J^2}{8} + \frac{3\sqrt{\frac{\pi J^2}{8}} C_T}{8\sqrt{\frac{\pi J^2}{8} + \frac{2}{3} C_T}} \right]$$

$$\frac{dC_N}{d\alpha_{prop}} = \frac{dC_M}{d\beta_{prop}} = 0$$

Solidity of the propeller is obtained with the following equation:

$$\sigma = \frac{4\bar{c}_b B}{3\pi D}$$

Where \bar{c}_b is the average blade chord from $0.2 R$ to the tip.

$$\bar{c}_b = \frac{1}{0.8} \int_{0.2}^1 c(r) d\left(\frac{r}{R}\right)$$

The resultant forces in body axis will be:

$$Z = \rho n^2 D^4 * \frac{dC_Z}{d\alpha_{prop}} \alpha_{prop}$$

$$Y = \rho n^2 D^4 * \frac{dC_Y}{d\beta_{prop}} \beta_{prop}$$

It must be noticed that, as installation effects are not considered, effective propeller angle of attack estimation may be inaccurate.

4.4. Battery

Electric Li-ion batteries will be used for this UAM project, as they are the most extended option in the industry. The battery is composed by cells connected in series and in parallel. First, the cell model will be introduced, which will define the dynamics of the battery. Then, arrangement of cells in a battery pack will be described.

4.4.1. Cell model

The cell model, based on Chen and Rincón-Mora(2006), captures transient and steady-state dynamics of a polymer Li-ion battery. First, an equivalent circuit able to include the necessary dynamics is defined. Then, parameters identification is performed based on low power measurements. From this model, temperature effects, storage time and cycle number will be neglected.

Model is presented in Figure 4. 14. The resistors and capacitors network in the right account for transient response. These parameters will be defined with a parameter estimation against low power tests of real batteries. Left part of the model will determine usable capacity with the capacitor $C_{capacity}$.

V_{SOC} represents the state of charge(SOC) of the battery, a measure of the available energy inside the battery. A value of 1 o 100% represents the battery is completely charged, while 0/0% means fully discharged. The open circuit voltage V_{OC} is a function of the SOC. This term's value will decrease as the SOC decreases, meaning that the operational voltage of the battery will be lower at lower SOC. All the resistors and capacitors used to model the dynamics of the battery will be also a function of SOC.

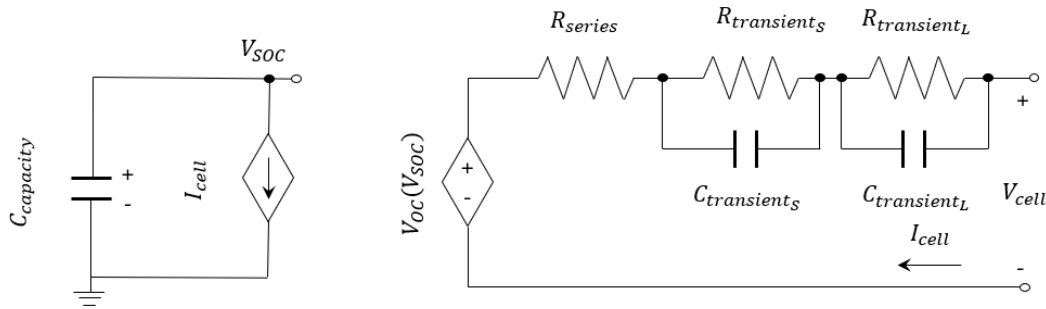


Figure 4.13:Cell electric diagram. Adapted from Chen and Rincón-Mora(2006).

The internal resistor of the cell will be defined as:

$$R_{Total} = R_{series} + R_{Transient_S} + R_{Transient_L}$$

At each moment, a certain amount of power will be demanded. The cell has to provide the same amount of power by regulating I_{cell} .

$$P_{req} = V_{cell} I_{cell} \text{ (Eq. 4.4.1)}$$

The voltage of the cell V_{cell} is a function of the voltage of the internal battery and a term that depends on internal resistors and current. It is relevant to note that I_{cell} reduces the voltage of the cell, which will have negative consequences for high power demands.

$$V_{cell} = V_{OC} - (R_{series} + R_{Transient_S} + R_{Transient_L}) I = V_{OC} - R_{Total} I_{cell} \text{ (Eq. 4.4.2)}$$

The current across the battery I_{Batt} will determine the discharge rate of the battery. C_{nom} is the nominal capacity and is obtained from the manufacturer.

$$\zeta_{discharge} = \frac{I}{C_{nom}}$$

Then, the variation of SOC at each time step is given by the following equation. It must be noted that iteration is required to be able to determine the proper value of I_{cell} that solves Eq. 4.4.1 and Eq. 4.4.2.

$$SOC(t + \Delta t) = SOC(t) - \int_t^{t+\Delta t} \frac{I_{cell}(t)}{C_{Nom}r_c} dt$$

The available battery capacity r_c at each time step is a function of I_{cell} and $\zeta_{discharge}$. This data can be extracted from discharge curves as shown by Vratny et al.(2013), presented in Figure 4.15. For high values of current and discharge rate, as the expected for high power demand, the available capacity of the battery is reduced. Therefore, apart from the higher current value, this term increases the battery energy consumption at high power demand.

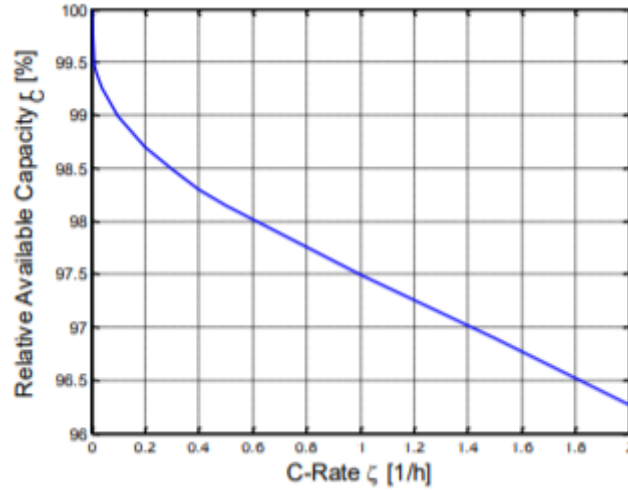


Figure 4.14: Relative available capacity r_c as a function of discharge rate. Extracted from Vratny et al.(2013).

Two more variables should be considered within the simulation. Cut-off voltage and maximum current intensity define the lower and upper limits respectively on voltage and current. If boundaries are surpassed, simulation is stopped. These values can be obtained from the manufacturer data.

The parameter estimation performed by Chen and Rincón-Mora(2006) for a low power Li-ion battery are presented below. As it can be observed, all the parameters inside the battery equivalent circuit vary as a function of SOC.

$$V_{OC}(SOC) = -1.031e^{-35 SOC} + 3.685 + 0.2156 SOC - 0.1778 SOC^2 + 0.3201 SOC^3$$

$$R_{Series}(SOC) = 0.1562 e^{-24.37 SOC} + 0.07446$$

$$R_{Transient_S}(SOC) = 0.3208 e^{-29.14 SOC} + 0.04669$$

$$R_{Transient_L}(SOC) = 6.603 e^{-155.2 SOC} + 0.04984$$

$$C_{Transient_S}(SOC) = -752.9 e^{-13.51 SOC} + 703.6$$

$$C_{Transient_L}(SOC) = -6056 e^{-27.12 SOC} + 4475$$

Validation with experimental data performed by the authors showed less than 0.4% runtime error for lower power application. The main limitation of the cell model is the behavior at high power output for each cell. The system identification for this model was performed using low power demand. Identification for high power demand may be inaccurate, especially considering that thermal effects are not included in the model.

4.4.2. Battery pack modelling

Cells are assembled into a battery pack following the methodology from Vratny et al(2013), represented in Figure 4.15. This simplified approach does not differentiate effectively between number of cells in parallel and number of cells in series. The output power is the power at each cell multiplied by the number of cells. Voltage will be given by the number of cells in series multiplied by the voltage of one cell. Current will be defined by the number of cells in parallel multiplied by the current from one cell. The logic behind this model is the following:

If number of batteries in series is increased, output voltage of the battery increases but total capacity maintains. For a constant power demand, the rise in voltage will cause the current demand to be lower. In the end, each cells discharges at a current of $\frac{P_{req}}{V_{cell}N_{series}}$. Therefore, in the end this will increase battery life also, as the energy required at each cell is lower.

If number of batteries in parallel is increased, output voltage of the battery is maintained but total capacity and current intensity rise. For a constant power demand, voltage will be the same but the current demand on each cell will be divided by the number of cells in parallel $\frac{\frac{P_{req}}{V_{cell}}}{N_{parallel}}$. This will result in an amplification of the total effective capacity. Therefore, in the end this will increase battery life also, as the energy required at each cell is lower.

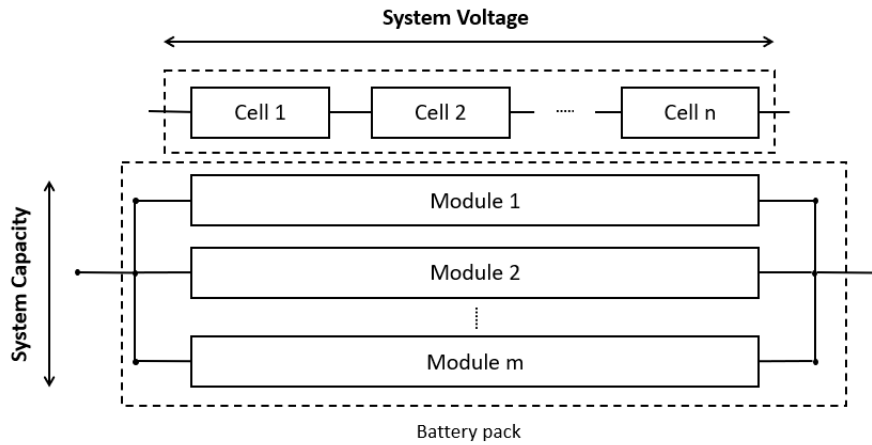


Figure 4.15: Battery model diagram. Adapted from Vratny et al(2013).

Second order effects of the number of cells in parallel and series are not included in this model. Thus, limitations for high power demand nor thermal effects will be addressed here. This may be problematic for hover phase, as the power required levels are elevated. Landing may be the worst part, not only due to the power demand but also because of the low levels of state of charge that will decrease output voltage, greatly increasing current demand.

To validate if model works as expected, a study showing the effects of increasing both number of cells in parallel and series is performed, presented in Figure 4.17. The results match with the expected results explained in the paragraphs above. It is confirmed that increasing the number of cells in series and in parallel has the same effect on SOC. The variation is found on the voltage and current intensity. Total voltage output is given by the voltage of one cell multiplied by the number of cells in series. Total current is obtained by multiplying the current in one cell by the number of cells in parallel.

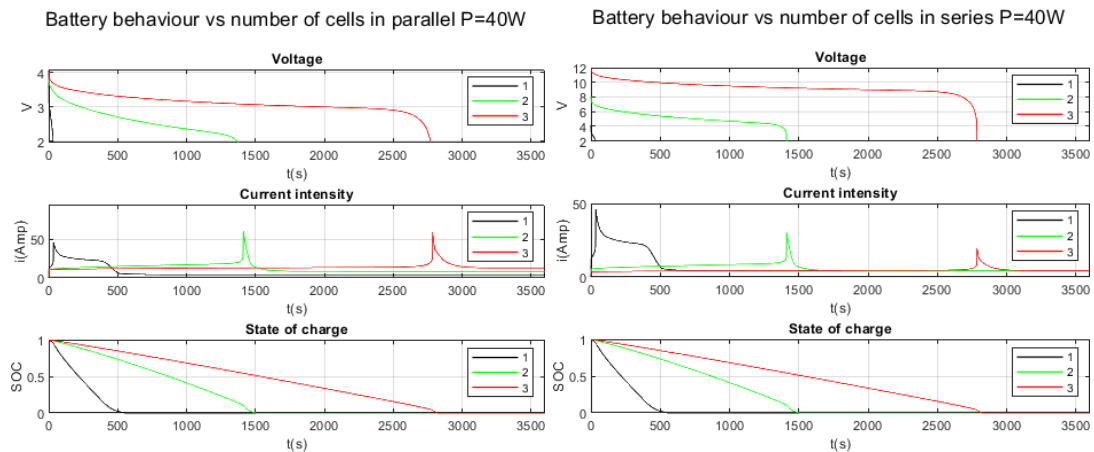


Figure 4.16: Battery study for increase in the number of batteries in series and in parallel.

4.5. Simulink model

For the sake of handling qualities analysis and control system design, a Simulink-Simscape model was developed. Model included all the components before mentioned or the results obtained with those models. It is divided mainly in blocks: Aeroderivatives, Powerplant, Control actuation, Forces and moments and Equations of motion. The structure is presented in Figure 4.17.

The aircraft inputs are the following:

- Control surfaces: Elevator deflection η , Aileron deflection ξ , Left rudder deflection ζ_{left} , Right rudder deflection ζ_{right} .
- Propeller: Left propeller tilt angle θ_{Lprop} , Left propeller rpm rpm_{Lprop} , Right propeller tilt angle θ_{Rprop} , Right propeller rpm rpm_{Rprop} and Back propeller rpm rpm_{Bprop} .

Control actuation block includes transfer function to account for delays in the inputs of the control surfaces due to the actuators. Delays are modelled as transfer function, different depending on the control surface.

Aeroderivatives block estimates the aeroderivatives values depending on the flight condition. Aeroderivatives obtained with AVL are inputted as look-up tables. The inputs in the look-up tables are CG position, Mach and altitude. Only first order linear terms will be obtained. Aeroderivatives included are:

- Lift: C_{L0} , $C_{L\alpha}$, C_{Lq} .
- Drag: C_{D0} .
- Lateral force: C_{Yp} , C_{Yr} , $C_{Y\beta}$.
- Pitch moment: C_{m0} , $C_{m\alpha}$, C_{mq} .
- Roll moment: C_{lp} , C_{lr} , $C_{l\beta}$.
- Yaw moment: C_{np} , C_{nr} , $C_{n\beta}$.

In Forces and moments block, all the forces within the aircraft are combined to obtain the total forces and moments at each time step. Aerodynamic forces and moments are a function of the aeroderivatives, the flight condition, the state of the aircraft and the control surfaces deflection. Propeller forces and moments will be obtained from the Powerplant block, described later. Gravitational forces are obtained from the product of the DCM matrix and the weight vector of the aircraft. Ground effect block has been developed by Cranfield's Flight Dynamics Group to account for additional forces and moments during take-off and landing.

The Equations of motion block calculates the state of the aircraft as a function of the forces and moments. Equations used are embedded in Simulink's block 'EoM Body Euler Angles'. This block further calculates Reynolds, Mach, altitude and dynamic pressure. Considerations for this block:

- Constant mass and inertia properties.
- Forces and moments about the CG
- CG is assumed to be equal to the Body Axis Centre where the aeroderivatives are defined about.

SIMULINK MODEL

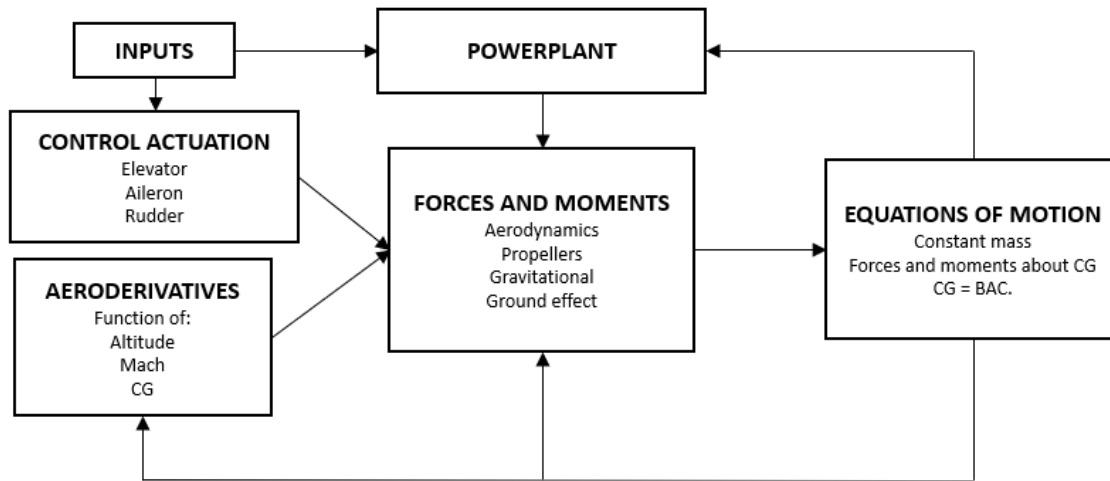


Figure 4.17: Simulink model global structure.

Powerplant, presented in Figure 4.19, contains the electric battery, the motor and the propeller. Motor and propellers are different for forward and back propellers. Effective angles and airspeed for each propeller is calculated as described in the following paragraphs. These values will be inputted to the Propeller forces and moments block and to the ESDU correction block. Meanwhile, motor is included as a time delay. An rpm integral time controller corrects possible deviation in the results if a more complex motor model is included.

Inside the Propeller forces, moments and power block, advance ratio is calculated considering the effective airspeed and the rpm. C_T and C_P look-up tables as a function of J are used to interpolate the value of power and thrust. Then, forces and moments in propeller axes about the propeller CG are obtained. The ESDU correction accounts for propeller effective angle of attack and sideslip effects. This correction only applies for propeller angles of attack and sideslip below 20deg. Finally, forces and moments are calculated about the CG in body axes.

Battery is implemented in Simscape following Section 4.4. The battery demand at each moment is the sum of the power demand by the three propellers.

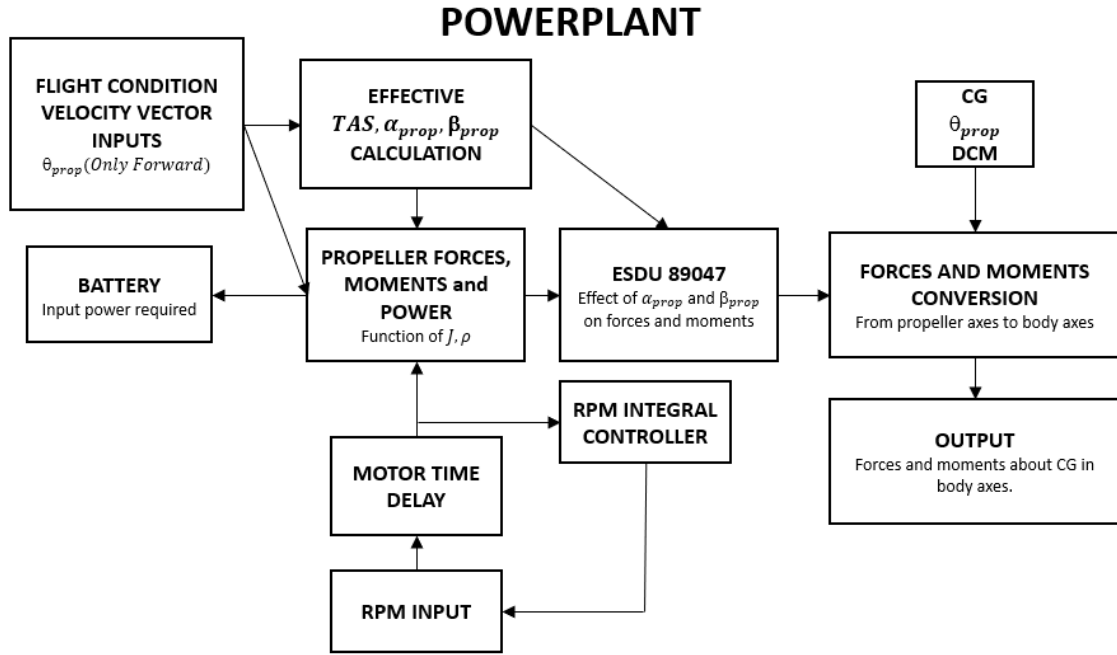


Figure 4.18: Simulink model powerplant structure.

Figure 4.20 shows the difference between the body and the propeller axes. Body axes centre is defined as the CG, with the X_B direction aiming to the nose of the aircraft, the Y_B direction to the right wing and Z_B downwards. Propeller axes centre is the propeller CG location. For the forward propellers, the X_{Fprop} direction is the normal to the propeller rotation plane. X_{Fprop} and Z_{Fprop} defined by the propeller pitch angle θ_{Fprop} rotation of the body axes about the Y_B axis. Back propeller pitch angle is always fixed to 90deg. Therefore, back propeller X_{Bprop} is always in the opposite direction to Z_B .

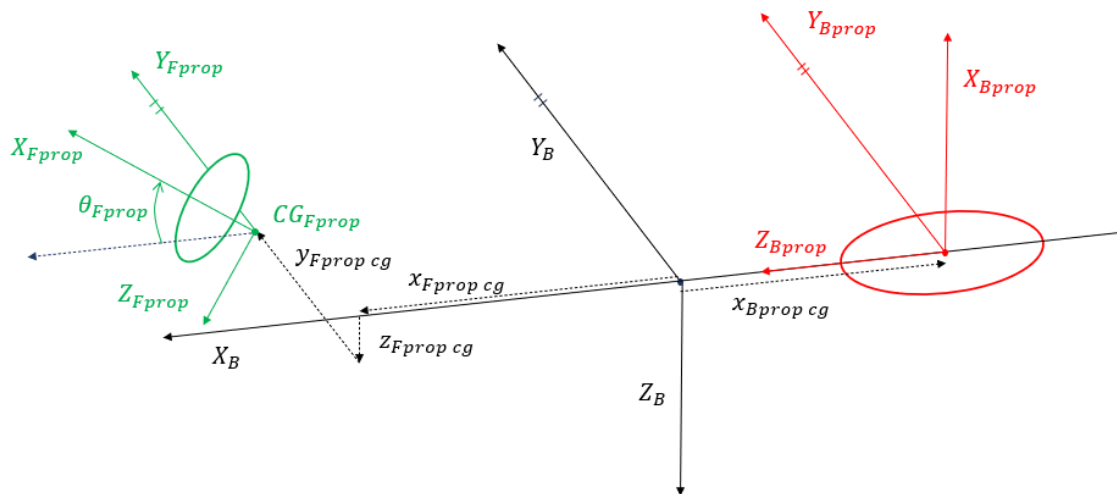


Figure 4.19: Propellers and body axes diagram.

The calculations inside the Effective angle of attack, sideslip and airspeed calculation block are described below. For the forward propeller, equations are:

$$\begin{aligned}
UVW_{Fprop} &= UVW + (PQR \times xyz_{Fprop}) \\
TAS_{Fprop} &= |UVW_{Fprop}| \\
\alpha_{Fprop} &= \theta_{prop} + atan\left(\frac{W_{Fprop}}{U_{Fprop}}\right) \\
\beta_{Fprop} &= asin\left(\frac{V_{Fprop}}{TAS_{Fprop}}\right) \\
DCM_{Fprop} &= \begin{bmatrix} \cos(\theta_{Fprop}) & 0 & \sin(\theta_{Fprop}) \\ 0 & 1 & 0 \\ -\sin(\theta_{Fprop}) & 0 & \cos(\theta_{Fprop}) \end{bmatrix}
\end{aligned}$$

Meanwhile, back propeller equations are:

$$\begin{aligned}
UVW_{Bprop} &= (DCM_{Bprop}UVW) + DCM_{Bprop}(PQR \times xyz_{Bprop}) \\
TAS_{Bprop} &= |UVW_{Bprop}| \\
\alpha_{Bprop} &= \theta_{prop} + atan\left(\frac{W_{Bprop}}{U_{Bprop}}\right) \\
\beta_{Bprop} &= asin\left(\frac{V_{Bprop}}{TAS_{Bprop}}\right) \\
DCM_{Bprop} &= \begin{bmatrix} 0 & 0 & -1 \\ 0 & 1 & 0 \\ 1 & 0 & 0 \end{bmatrix}
\end{aligned}$$

4.6. Optimization

Complexity and nonlinearities of the full aircraft problem make the task of selecting the appropriate configuration by iterative procedure extremely complicated and time consuming. Optimization techniques allow the automation of this task. By establishing a series of cost functions, the optimality conditions are defined.

Single-objective optimization returns the best possible individual for a certain objective function. Multi-objective optimization techniques yield as a result a Pareto front with the best possible solutions for a set of objectives. It is impossible to reduce any of the objective functions without increasing at least one of the other objective functions (Liu, Yang and Whidborne, 2006).

4.6.1. Genetic Algorithm

Genetic algorithms are probabilistic search procedures based on the evolutionary process in nature. This population approach is based on the iteration and evolution of the solutions in each generation via different mechanisms. The benefits of using these algorithms are that no derivative information is required and the flexibility in its application (Deb, 2011) (Liu, Yang and Whidborne, 2006).

The operations to evolve the current population can be classified into selection, crossover and mutation. However, different mechanism can be available in more complicated algorithms due to the flexibility of evolutionary algorithms. The selection of the individuals is done so that the fitter individuals with the lower cost associated have more possibilities to be selected for crossover and mutation. Crossover corresponds to combination of two individuals. Mutation is the variation of one individual. The objective in a multi-objective genetic algorithm optimization is to develop a population of Pareto-optimal solutions (Liu, Yang and Whidborne, 2006).

For the current project, MATLAB embedded algorithms 'multiobj' and 'gamultiobj' are used for single-objective and multi-objective respectively. These algorithms allow for implementation of linear and nonlinear constraints for the parameters. Stopping criteria can be modified to be a function of stalled generations, time or number of generations among others. The criterion used for most of the optimizations was defined by the number of stalled generations. This means the number of generations without a change in the Pareto Front below a certain value.

Furthermore, seeding options for the initial population matrix are available. Seeding will be used inside the optimization scheme defined in 4.8.1 to improve the optimization process efficiency. Population size is another relevant parameter. Too high populations will allow for a wider inspection of the evaluated space, but the time to process each generation will be lower. As a result, convergence time will be increased as the population size increases.

Different crossover and mutation algorithms were tested, but no relevant effect on computational time was noted.

The limitation of these algorithms is the random character in its initial search. For a high-dimensional space like the present in this project, this can lead to an increase in computational resources and problems with convergence to an optimum solution. Nevertheless, this can be solved with a proper initial seeding

with sensible points based on experience. Another problem is the slow convergence rate compared to pattern search or goal attain methods. Therefore, a hybrid optimization was implemented. After finishing the first genetic algorithm optimization with relaxed convergence criteria, a second fast optimization was run. Given the complexity of the current problem, the use of a pattern search was recommended by MathWorks(2020d)

4.6.2. Pattern search algorithm

Pattern search optimization methods are used in this project as a complement to the genetic algorithm optimization. This optimization grants faster convergence rates, accelerating the obtention of the optimum Pareto front when the optimum area seems to be located.

This algorithm evaluates non-dominated points within its population. Once a point is dominated, it stops being evaluated. Dominance criteria is established by Hypervolume. The Pareto front points create a volume/area that defines the dominated area as in Figure 4.21.

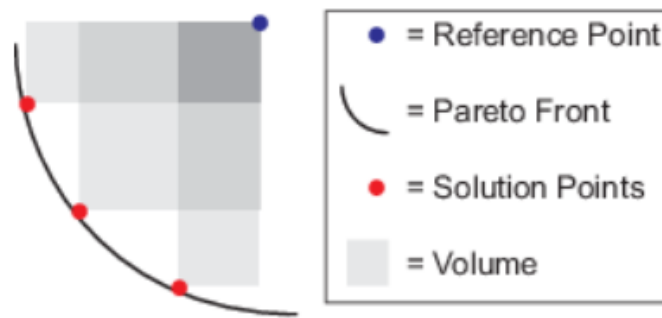


Figure 4.20: Pattern search dominated area defined by Hypervolume criterion.

Each iteration, every non-dominated point inside the boundaries that complies with the linear and non-linear constraints is evaluated and polled. A poll is obtained by varying the different variables in the function. After each run, all the dominated points are eliminated and the iteration re-starts. Mesh size varies depending on the results. If none of the polled points provide an improvement in cost, mesh size is reduced in the next iteration. Otherwise, it keeps iterating until finding an unsuccessful poll (MathWorks, 2020d).

The algorithm used is 'paretosearch' embedded in MATLAB. This algorithm is seeded with the previous genetic algorithm optimization Pareto front.

4.7. Response surface

One of the main problems during the optimization is the elevated amount of computational resources required, which translates to extensive time consumption. Response surfaces arise as a solution to reduce calculation time, as AVL, XFOIL or any other software are substituted by an equivalent mapping. By creating a database, curve fit or metamodel, the cost function or any parameter can be evaluated almost instantaneously for any value inside the optimization domain.

Many different models can be used, from linear regression to neural networks, depending on the function treated and its degree of complexity. As the number of dimensions increases, so does the number of points and the computational cost required to model the response surface.

Procedures to establish response surface are usually iterative, starting with a wide mapping of the whole optimization domain. Then, response surface precision should be further increased, picking relevant points within the most interesting zones. Keeping in mind the impossibility of mapping the whole domain accurately, selection of points should be done focusing on the best performance areas.

Keane and Nair (2005, p153-155) provide some guidance on the elaboration of response surfaces and the important aspects within metamodeling. Decisions should be made for seeding and fitting methods, gradient determination and the number of models used in the optimization. Some others relevant aspects include calculation errors treatment and data cleansing. Then, iteration methods, points search and updating procedures should be included for further accuracy enhancement.

Also, the applicability of parallel computing is incredibly important here, considerably reducing computation time. Fortunately, MATLAB allows several programs running at the same time, allowing to increase the number of datapoints gathered at the same time.

A diagram with the procedure for response surface identification is presented below. In the following subsections, each of the steps in this diagram will be explained.

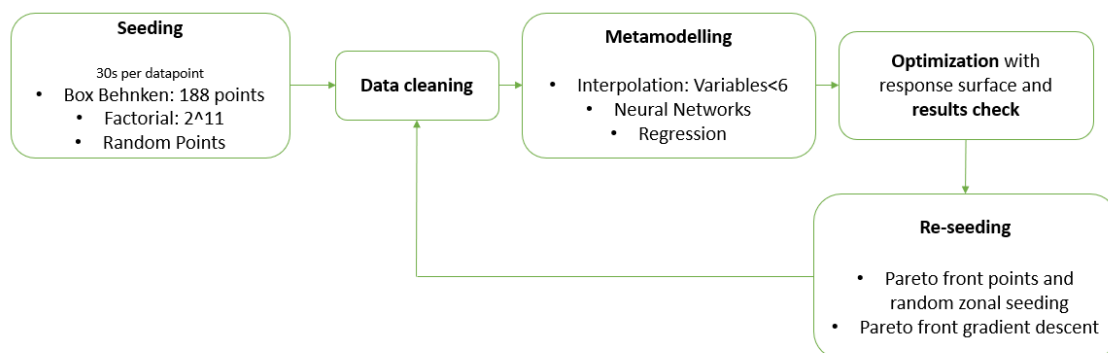


Figure 4.21: Response surface creation diagram.

4.7.1. Seeding

To obtain the first metamodel approximation, it is necessary to evaluate a certain number of points within the domain. Ideally, a 3 factorial design would be implemented for an accurate function determination. However, this would require an incredible high number of data points 3^n , where n is the number of dimensions. Therefore, other procedures that require lower computational time must be implemented.

2 Factorial seeding maps the extremes of the domain, evaluating the lower and upper bounds of each parameter. Thus, 2^n points are computed. To map intermediate points, a Box-Behnken seeding is implemented. This evaluates combinations of the mean values for each of the variables, with 188 points for 11 parameters. The representation of these seeding methods can be observed in Figure 4.23.

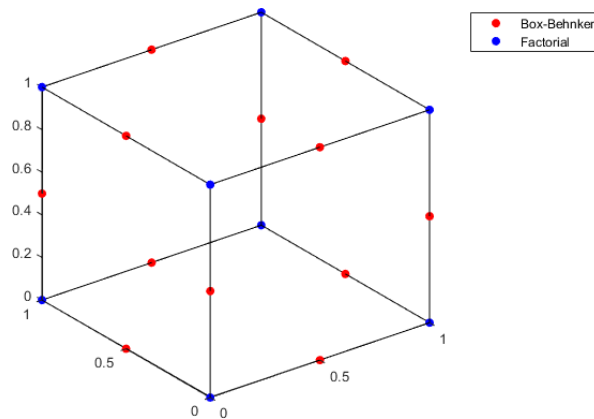


Figure 4.22: Box-Behnken and factorial design seeding diagrams.

In combination with the previous methods, random points are obtained evaluated inside the boundaries. The number of points depends on the available time at that moment.

For the re-seeding and response surface update, an steepest descent algorithm that improved optimization results while saving the evaluated points was used.

It is interesting to note that parallel computing considerably reduces computational time. Simultaneous evaluations can be obtained with up to 4 MATLAB programmes running at the same time. Although running time for each point evaluation is increased up to 5s when running various simulations simultaneously, the total outcome in time reduction using parallel computing is positive.

4.7.2. Metamodel fitting: Interpolation, regression and neural networks.

With the seeding points evaluated, defining the type of model to be used comes next. Depending on the function to be represented, the choice may vary, as it does not exist a one fits all option. Linear models may serve to model simpler functions rapidly, while nonlinear results like the obtained with AVL would require nonlinear mechanics into the model. The methods that have been tested in this project are interpolation, nonlinear regression and neural networks. A discussion of the different methods results is presented in the third subsection 4.7.2.3.

Multivariable interpolation methods work better for low number of variables, normally below 6. Among the different algorithms were tested: Shepperd interpolation, a robust smoothing of gridded data algorithm by Garcia(2009), a simple nearest neighbor interpolation and embedded in MATLAB 'griddatan'(MathWorks, 2020b). The problem with these algorithms is that for non-gridded data, computational cost surges. This is due to the fact that it is necessary to find the closest data points to the evaluated point before interpolating.

Nonlinear regression is based on a Levenberg-Marquardt nonlinear least squares algorithm implemented in MATLAB with the function 'nlinfit'(MathWorks,2020c). Before running the least squares algorithm, it is necessary to define the regressors of the metamodel. Different models were tested varying the number and the order of the terms.

Being b the regressors and x the independent variables or the parameters, so that $y = bx$:

- Simple: Linear and non-coupled coefficient for each of the parameters:

$$y = b_0 + b_1x_1 + b_2x_2 + \dots + b_nx_n$$
- Complex: Second order terms with wing-canard terms coupled

$$y = b_0 + b_1x_1 + \dots + b_nx_n + b_{ii}x_i^2 + \dots + b_{nn}x_n^2 + b_{ij}x_ix_j + \dots + b_{nm}x_nx_m$$
- Complex Non-coupled: Second order terms with wing and canard uncoupled.
- Complex Only wing terms: Second order coupled terms for only the wing.

There is a trade-off between accuracy and confidence in the results. By increasing the number of terms, accuracy will be increased. However, the confidence in the estimation will be lower, with the confidence intervals becoming wider as the number of variables increase. (Lone, 2020)

When fitting the model, dataset was divided into evaluation and the validation datasets. The size of the validation dataset varied up to a 5% of all the points when number of points were over 20000. The minimum size of the validation size was established as 500 points. After fitting the model, the error of both models was compared for validation of the regression method as in Figure 4.24. Neural network train algorithm has this functionality already embedded in MATLAB.

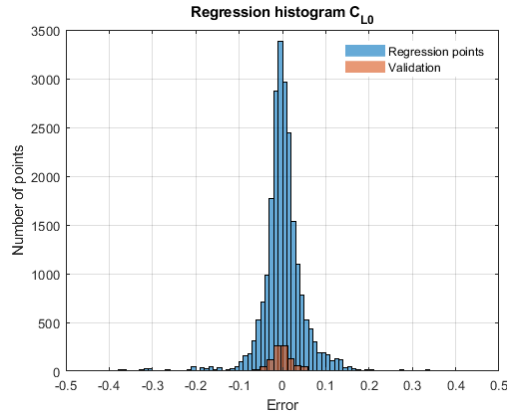


Figure 4.23: Error histogram comparing regression and validation errors.

4.7.2.1. Neural Networks

A section is included for neural networks due to its use being relatively innovative for engineering projects. In the end, neural networks do no more than provide an input-output mapping by establishing a series of connection between the different nodes or neurons in the network (Liu, Yang and Whidborne, 2006).

Neural networks structures tested were Feed-forward and cascade-forward. Due to the relatively low number of variables, a shallow architecture with only one hidden layer will be used. In the feed-forward network, structure is divided into hidden layer and the output layer. For a number of inputs X , the hidden layer receives the X inputs and multiplies each of them by a weight. Another bias term is added to each of the weighted inputs, yielding the hidden layer output. The number of outputs obtained from the hidden layer is given by the hidden layer size. Then, in the output layer, each of the hidden layer outputs is weighted and summed to a bias, yielding the final output. Being the size of the hidden layer n , the total number of weights and biases is given by $n(2X + 1) + 1$.

In the cascade-forward, the structure is the same, but another additional connection between inputs and the output layer is added. Each of the inputs is weighted by Weights 1, while each of the hidden layer inputs is weighted by Weights 2. The total number of weights and biases is given by $n(2X + 1) + X + 1$.

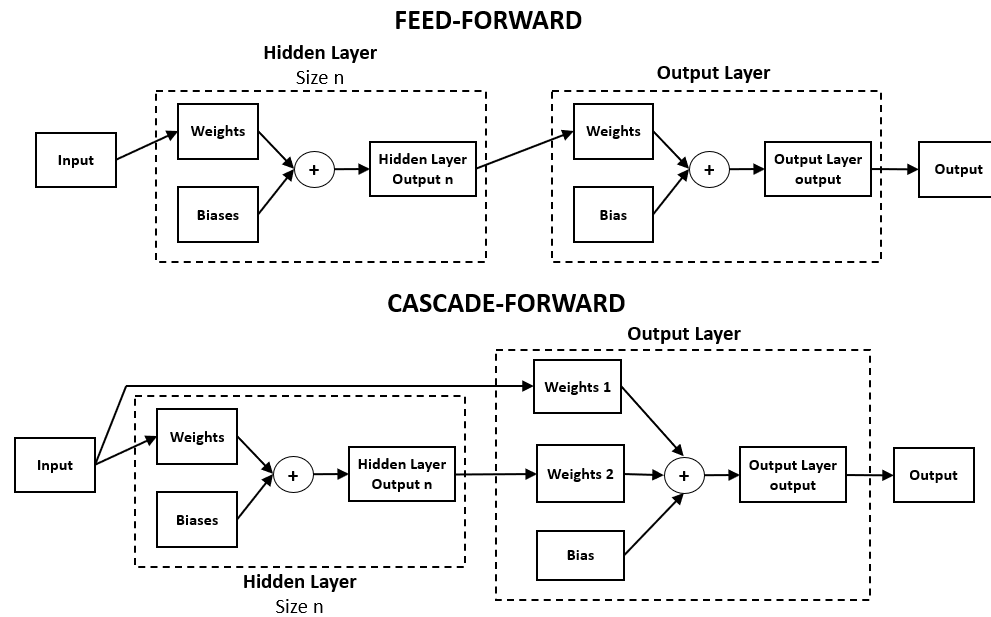


Figure 4.24: Feed-forward and cascade-forward neural network architectures.

Once the architecture is defined, the algorithm to train the neural network must be defined. Training the neural network is just the analogy for decreasing the error between the output and the real value. It is extremely difficult to know which training algorithm will be the fastest for a given problem. Performance is conditioned by many factors: complexity of the problem, the number of data points in the training set, the number of weights and biases in the network, the error goal, and whether the network is being used for pattern recognition or function approximation/regression (MathWorks, 2020a).

For the current regression problem, with networks that contain up to a few hundred weights, Levenberg-Marquardt algorithm 'trainlm' will have the fastest convergence. For most of the cases, 'trainlm' is able to obtain lower mean square errors than any of the other algorithms embedded in MATLAB. However, the storage requirements of this algorithm are also larger.

Other interesting algorithms may be Scaled Conjugated Gradient (SCG), BFGS Quasi-Newton or Variable learning rate backpropagation.

The conjugate gradient algorithms seem to perform particularly well for networks with a large number of weights. The SCG algorithm is almost as fast as the Levenberg-Marquardt algorithm on function approximation problems (faster for large networks), while having relatively modest memory requirements.

The performance of BFGS is similar to that of Levenberg-Marquardt algorithms. It does not require as much storage, but the computation required does increase geometrically with the size of the network, because the equivalent of a matrix inverse must be computed at each iteration.

The variable learning rate algorithm `traindxd` is usually much slower than the other methods and has about the same storage requirements, but it can still be useful for some problems.

4.7.3. Methodology comparison

Creation of the response surface has an enormous influence in the optimization results. It is impossible to obtain appropriate results if the response surface does not represent accurately the full model. In this section, an analysis of the accuracy of different fitting methods is discussed to justify the selection of the model used for every aeroderivative and aerodynamic parameter.

Interpolation methods showed good results if the number of variables was below 6. For more variables, running time rose exponentially. Different algorithms were tested: Shepperd interpolation, a robust smoothing of gridded data algorithm by Garcia(2009), a simple nearest neighbor interpolation and embedded in MATLAB 'griddatan'(MathWorks, 2020b).

With 5 input variables, XFOIL could be easily modelled with an interpolation method. The algorithms mentioned on the previous paragraph were tested. Final decision was to use 'griddatan' with a linear interpolation, as it was the most robust and the fastest. Linear interpolation could be used thanks to the relatively fine grid of 5 factorial points.

For AVL response surface, interpolation methods proved to be ineffective. All these methods presented running times over 20 seconds for 11 variables. Therefore, regression methods and neural networks arose as the only feasible choices. As a way to judge the accuracy of the method, the distribution of the error histogram of the distribution was analysed.

For every case, 'Simple' regression model with only linear terms performed worse than the 'Complex' model. For cases when accuracy is similar for two of the models, the one with the lower number of terms will be used. This is the case of the control derivatives, where just including the surface where they are located drew the same accuracy results.

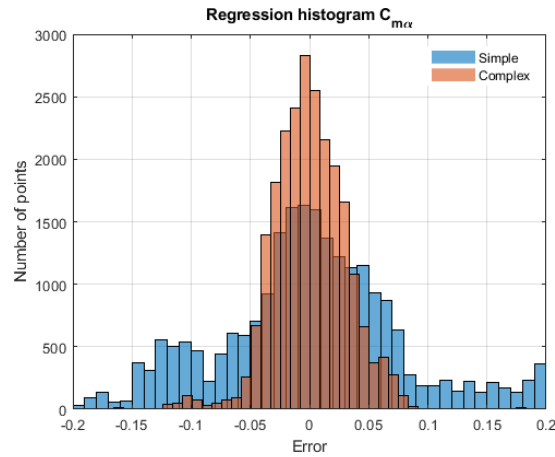
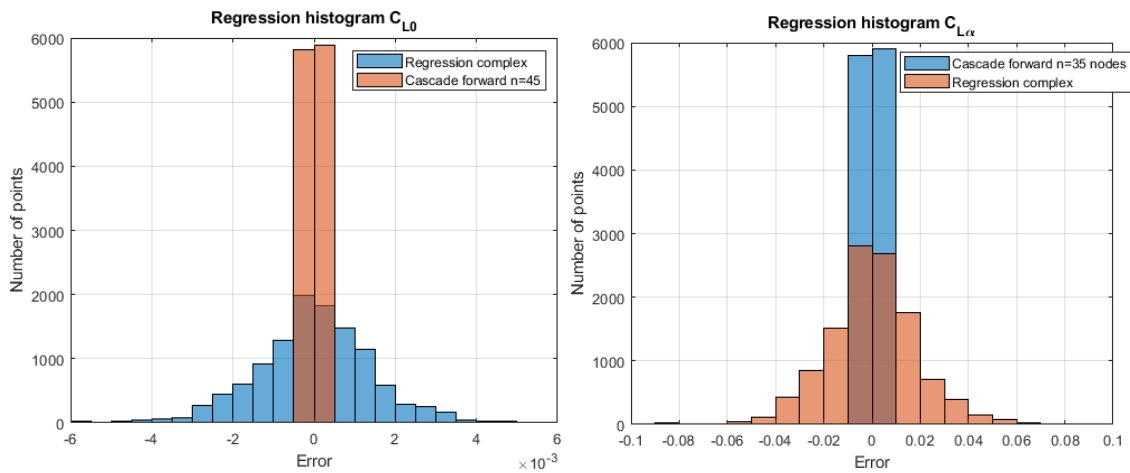


Figure 4.25: Error histogram for Simple vs complex regression models.

For the neural networks, different hidden layer sizes(20,35,50), structures(feedforward and cascade-forward) and training algorithms(Levenberg-Marquardt, Scaled Conjugated Gradient, BFGS Quasi-Newton and Variable learning rate backpropagation) were tested.

The same procedure was performed for the neural network, always obtaining better results with cascade-forward structure and Levenberg-Marquardt algorithm. Hidden layer optimum size varied depending on the aeroderivative. Control aeroderivatives performed better for a size of 25 hidden layers. Meanwhile, CL_0 and C_{m0} performed better for a size of 45, while the rest for 35.

Finally, regression and neural network results were tested against regression in Figure 4.27. Neural networks provided much better accuracy for the mapped domain, eliminating biases and decreasing standard deviation in the estimation. However, due to huge number of terms, confidence of the estimation may be reduced.



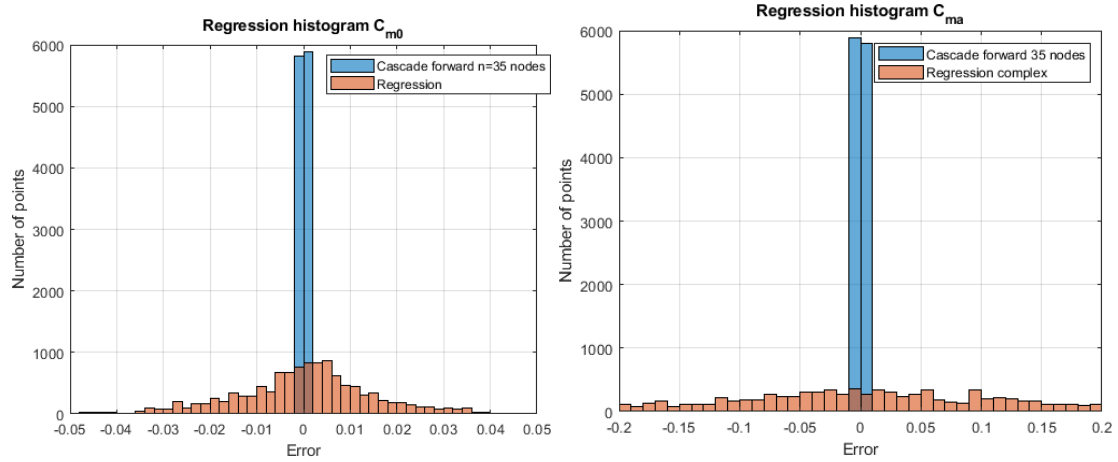


Figure 4.26: Error histograms for the different configurations

As mentioned during response surface methodology description, estimation is strictly limited to the mapped zone. Its use can lead to inaccuracies if the zone is not properly seeded. Furthermore, as can be confirmed in Figure 4.27, C_{M0} proves to be extremely complicated to model, with higher relative errors than the other aeroderivatives. As a result, trimming points accuracy will be affected.

However, this can be corrected by proper re-seeding of the zone. As observed in the following figure, error in the estimation of C_{M0} is greatly reduced when the domain is seeded.

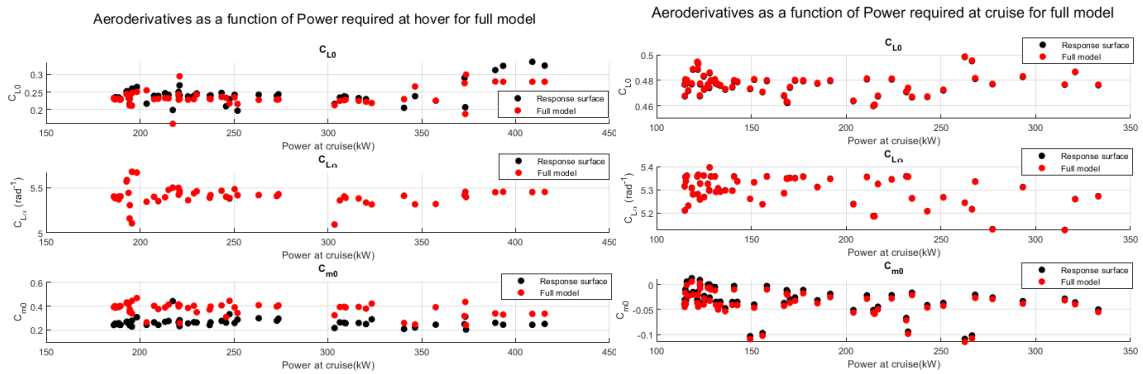


Figure 4.27: Comparison of aeroderivatives results with response surface and the full model. Image on the right had been re-seeded after showing poor results.

4.8. Model Assembly

4.8.1. Optimization model assembly

With the objective of assessing performance, a genetic algorithm multi-objective optimization establishing cruise and hover power consumption as the objective functions was performed. A trimming routine is included within the optimization before assessing aircraft performance. A diagram with the plant view and the main parameters of the optimization is presented in Figure 4.29.

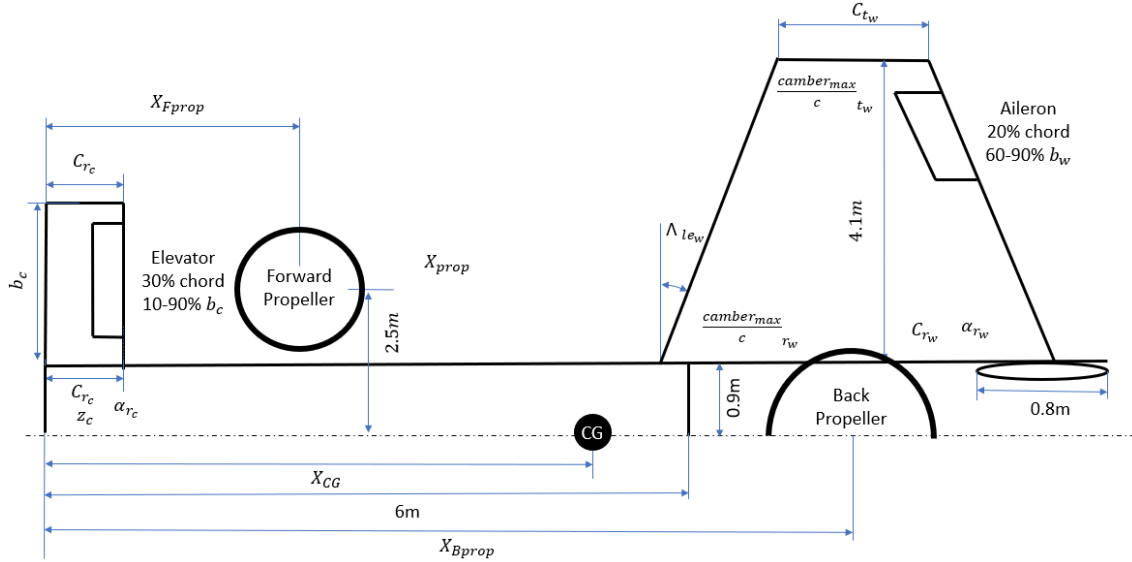


Figure 4.28: Full aircraft simplified plant diagram.

The structure of the optimization is presented in the diagrams below. The optimization parameters and the flight condition defined by altitude and TAS serve as the inputs for the aerodynamic and forward propeller blocks. The aerodynamic block includes AVL, zero-lift drag correction and the Oswald factor calculation from Scholz(2012). Due to the considerable amount of time consumed by AVL, around 30 seconds, a response surface is used to model aeroderivatives.

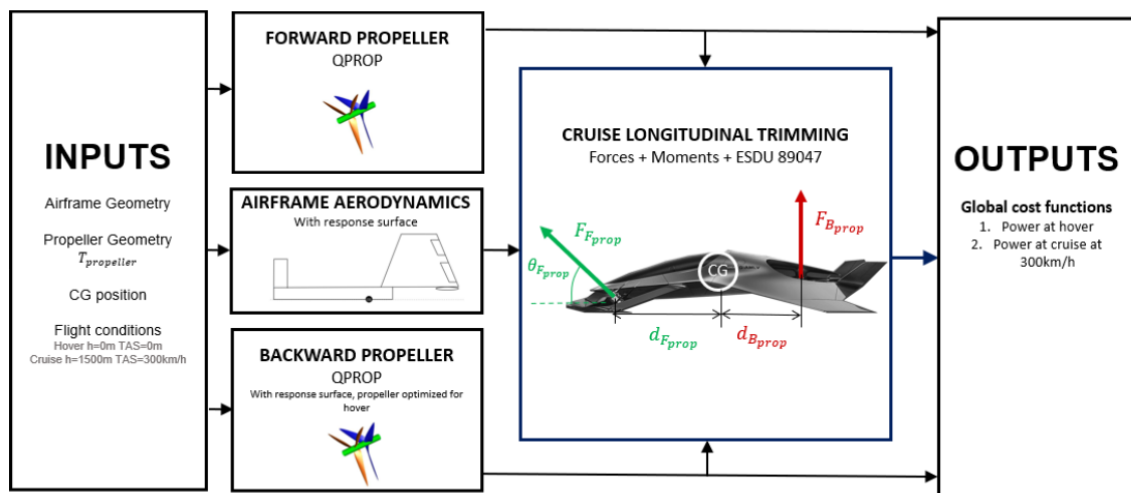


Figure 4.29: Model integration diagram for the optimization process.

Meanwhile, the forward propeller block calculates forces, moments and required power at each flight condition. The former two are fed to the longitudinal trimming module and the second to the cost function calculation. Known the flight condition and the propeller thrust at cruise, which are inputs to the optimization, power consumption calculation is feasible with QPROP. For hover thrust calculation, equilibrium of forces and moments is calculated with the model simplification presented in Figure 4.30. Zero pitch angle is assumed, while back and forward propeller thrusts acting perpendicular to the airframe. Propeller forces are then defined as a function of airframe and forward and backward propellers CG position. QPROP is not modeled as a response surface as its running time is below 0.1s.

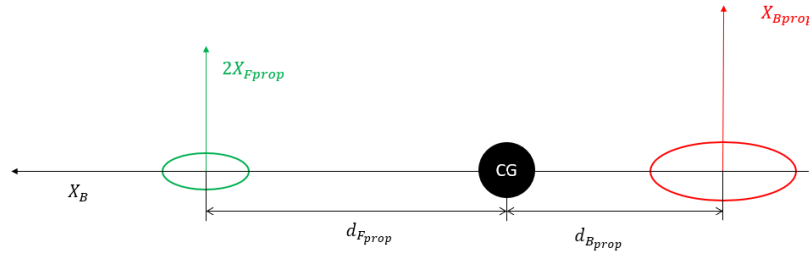


Figure 4.30: Propeller forces diagram during hover.

$$2X_{Fprop}d_{Fprop} = X_{Bprop}d_{Bprop}$$

$$W = 2X_{Fprop} + X_{Bprop}$$

The backward propeller block uses a response surface to model power required at hover. This response is obtained from the results presented in Section 5.1.2. The required thrust at hover is the input to calculate power required at hover, using a second order fit. A model to account for autorotation effects during forward flight is not included. Therefore, back propeller will have no effect in the cruise condition.

Before computing the power required or any other cost function, a trimming module establishes a constrain on the model, assigning a really high cost if the trim does not comply with the defined requirements or is infeasible. This module will include only longitudinal forces and moments, according to the following assumptions. First, the use of counter-rotating propellers and the assumptions of zero sideslip and equal tilt angle and rotational speed for both forward propellers allows, following the equations in ESDU 89047(2006), to neglect lateral directional moments and forces. As a result, a nonlinear system of 3 equations with 3 variables η_{elev} , θ_{prop} and α_b is obtained and presented below. Therefore, more than 1 solution will be present and so 'fsolve' will be used, a trust region local optimization algorithm embedded in MATLAB which requires an initial condition.

$$q_{prop} = \rho n^2 D^4 * \frac{dC_z}{d\alpha_{prop}} \text{ (from ESDU 89047)}$$

$$Z = 0 = q_{\infty} S_w (C_{L0} + C_{L\alpha} \alpha + C_{L\eta} \eta) - 2000g \\ + 2 \left(T_{Fprop} \sin(\alpha + \theta_{prop}) - q_{prop} \left((\alpha + \theta_{prop}) \cos(\alpha + \theta_{prop}) \right) \right)$$

$$X = 0 = -q_{\infty} S_w \left(C_{D0} + K(C_{L0} + C_{L\alpha} \alpha + C_{L\eta} \eta)^2 + C_{D\eta} \eta \right) \\ + 2 \left(T_{Fprop} \cos(\alpha + \theta_{prop}) + q_{prop} \left((\alpha + \theta_{prop}) \sin(\alpha + \theta_{prop}) \right) \right)$$

$$M = 0 = q_{\infty} S_w MAC (C_{m0} + C_{m\alpha} \alpha + C_{m\eta} \eta) \\ + 2X_{CGprop} \left(T_{Fprop} \sin(\theta_{prop}) - q_{prop} \left((\alpha + \theta_{prop}) \cos(\theta_{prop}) \right) \right) \\ + 2Z_{CGprop} \left(T_{Fprop} \cos(\theta_{prop}) + q_{prop} \left((\alpha + \theta_{prop}) \sin(\theta_{prop}) \right) \right) \\ + M_{viscous}$$

$$M_{viscous} = q_{\infty} S_w \left(CD_c \left(z_c \cos(\alpha) + \left| CG - X_{\frac{mac}{4}_c} \right| \sin(\alpha) \right) \right. \\ \left. + CD_w \sin(\alpha) \left| CG - X_{\frac{mac}{4}_w} \right| + CD_{fus} \sin(\alpha) \left| CG - X_{\frac{mac}{4}_{fus}} \right| \right)$$

$$(All \alpha = \alpha_b)$$

Considering that for cruise elevator angle should be close to zero, the angle of attack must be within the linear lift coefficient curve region and the ESDU correction only works within $\pm 20deg$ of propeller tilt angle, the following requirements are defined: $|\eta_{elev}| < 2deg$; $\alpha_b < 10deg$; $|\theta_{prop}| < 20deg$. η_{elev} is chosen considering that, during cruise, elevator deflection should be close to $0deg$. The restriction on the angle of attack is selected as an estimate of the linear region of the lift coefficient curve.

This limit may be further extended when trimming for another conditions, but in order to stick to the validity region of the model and the design constrains, maximum values should be: $|\eta_{elev}| < 20deg$; $\alpha_b < 10deg$; $|\theta_{prop}| < 20deg$.

As mentioned in the previous sections, genetic algorithms can be excessively time consuming due to the random nature of the seeding. This is especially relevant for optimizations with an elevated number of variables. In order to achieve optimum results in reasonable time, pre-seeding of the full aircraft optimization was needed. This scheme, based on decoupling the optimization in simpler previous steps with less variables to optimize, is presented in Figure 4.32. These simple steps considerably reduced optimization time.

First, only the 11 parameters from the airframe geometry and the airframe CG are optimized in a single-objective optimization. Cost function is defined as thrust required at cruise at 300km/h. Then, CG position and drag are provided as the

seeding for the propellers multi-objective optimization. Variables optimized are propellers geometry and CGs. Cost function are defined as power required at hover and power required at cruise at 300km/h. Finally, the full aircraft optimization is seeded with the optimum aircraft and the propellers optimization Pareto front. Cost function are defined as power required at hover and power required at cruise at 300km/h. Each of the three optimizations consist of a multi-objective genetic algorithm optimization followed by a pattern search algorithm optimization.

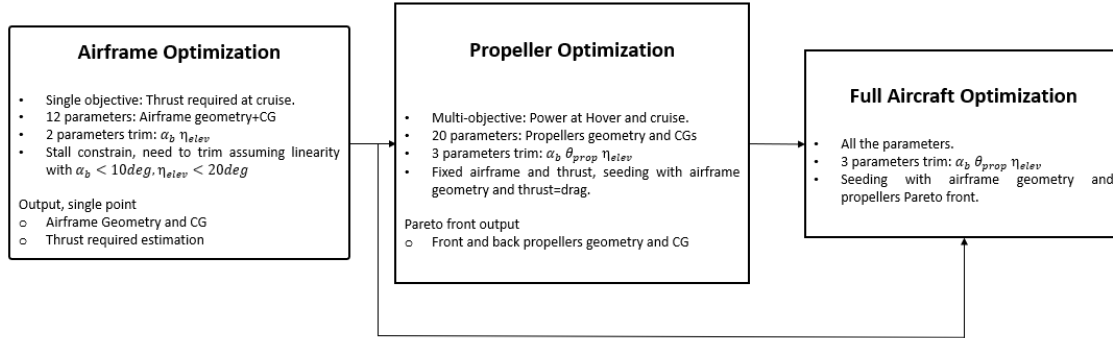


Figure 4.31: Optimization scheme diagram.

4.8.2. Performance trimming module

To obtain an estimation of how the aircraft flies at each point in the flight envelope, it is necessary to trim the aircraft at each flight condition. By obtaining the trimming curves, not only the trimming conditions will be defined, but also the power required at each flight condition. Again, only longitudinal trim will be considered following the assumptions that neither counter-rotating propeller nor the airframe generate lateral-directional forces or moments when sideslip is 0. Therefore, 5 different inputs will be determined at each point: airframe angle of attack, propeller tilt angle, elevator deflection and forward and backward propellers' thrust.

However, some limitations in the modelling can be found:

First, AVL aerodynamic modelling cannot provide accurate estimates for the non-linear part of the lift curve. Therefore, angle of attack will be limited to a maximum of 10deg and to a minimum of -5deg. This limit can be considered as a conservative estimation.

Second, propeller ESDU 89047(2016) correction is only valid for a propeller angle of attack below 20deg. As a result, model accuracy will decrease when this angle is surpassed and the ESDU correction will not be used in those cases.

Also, back propeller estimations may be inaccurate as inflow conditions in that zone are unknown with the current simplified model. Inflow conditions will be

defined as the airspeed at where the aircraft is flying without further correction for back propeller angle of attack.

Finally, elevator deflection will be limited to $\pm 25^\circ$ according to the decisions made by the design team from Cranfield's flight dynamics group.

Depending on the curve to obtain, different algorithms will be used, but all of them will be based on obtaining the lowest power possible trim via iterative exhaustive search schemes combined with MATLAB's embedded function `fsolve`.

Two different approaches will be used in the optimization depending on the speed. One which only includes the forward propellers forces and moments, used when the airframe is above the stall speed (the one for an angle of attack equal to 10° considering only the airframe aerodynamics). The other, for speeds below stall, also includes back propeller in the optimization.

For each of the variables, a range of values covering its whole domain is tested, like in a exhaustive search optimization algorithm. Each of the possible combinations will be evaluated with MATLAB's trimming algorithm '`fsolve`'. This algorithm performs a trust-region optimization, locating the local minimum for the forces and moments starting from a defined point. If trim is possible and the inputs are inside the domain, the point is saved, also calculating the required power for the forward and, if used, the back propellers. Finally, the point with the minimum power is selected as that condition trim point.

This algorithm is run at each flight condition, speed and altitude, to obtain a complete power vs airspeed envelope. As it can be deduced from the methodology, there is the chance that the obtained minimum is not the global minimum, although this can be solved by increasing the number of evaluated points at the expense of considerably increasing the computation time.

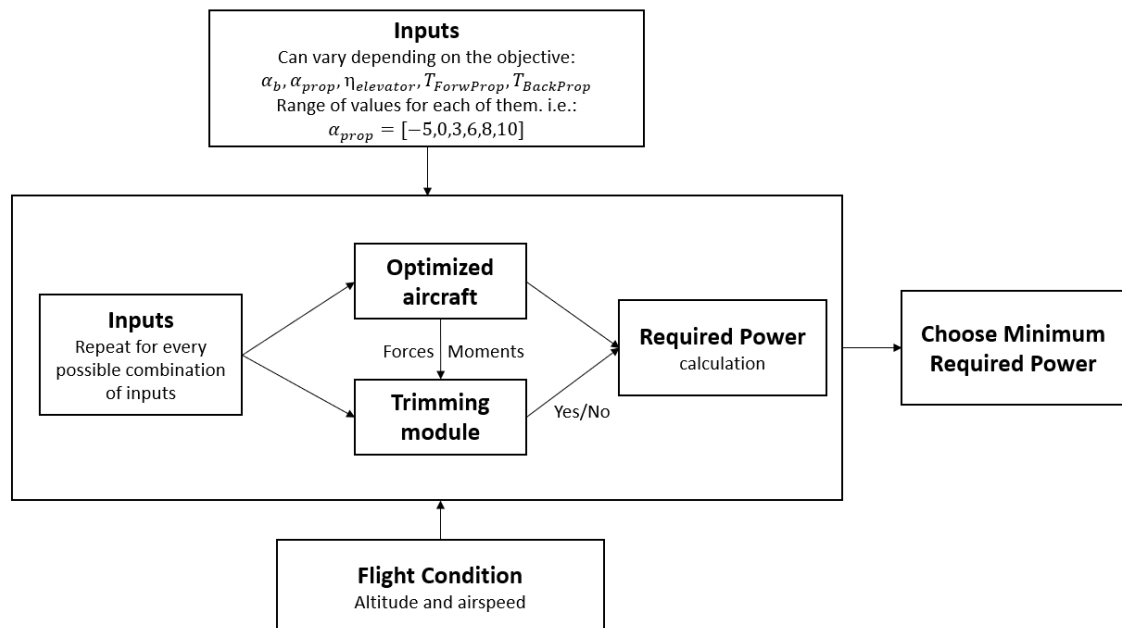


Figure 4.32: Trimming routine diagram.

The trimming equations inside the trimming module which must be minimized are:

$$q_{prop} = \rho n^2 D^4 * \frac{dC_z}{d\alpha_{prop}} \text{ (from ESDU 89047, 0 for } (\alpha + \theta_{prop}) > \pm 20deg)$$

$$\begin{aligned} Z &= q_{\infty} S_w (C_{L0} + C_{L\alpha} \alpha + C_{L\eta} \eta) - 2000g \\ &+ 2 \left(T_{Fprop} \sin(\alpha + \theta_{prop}) - q_{prop} ((\alpha + \theta_{prop}) \cos(\alpha + \theta_{prop})) \right) \\ &+ T_{Bprop} \cos(\alpha) \end{aligned}$$

$$\begin{aligned} X = 0 &= -q_{\infty} S_w (C_{D0} + K(C_{L0} + C_{L\alpha} \alpha + C_{L\eta} \eta)^2 + C_{D\eta} \eta) \\ &+ 2 \left(T_{Fprop} \cos(\alpha + \theta_{prop}) + q_{prop} ((\alpha + \theta_{prop}) \sin(\alpha + \theta_{prop})) \right) \\ &- T_{Bprop} \sin(\alpha) \end{aligned}$$

$$\begin{aligned} M = 0 &= q_{\infty} S_w MAC (C_{m0} + C_{m\alpha} \alpha + C_{m\eta} \eta) \\ &+ 2X_{CGprop} \left(T_{Fprop} \sin(\theta_{prop}) - q_{prop} ((\alpha + \theta_{prop}) \cos(\theta_{prop})) \right) \\ &+ 2Z_{CGprop} \left(T_{Fprop} \cos(\theta_{prop}) + q_{prop} ((\alpha + \theta_{prop}) \sin(\theta_{prop})) \right) \\ &- X_{Bprop} T_{Bprop} + M_{viscous} \end{aligned}$$

$$\begin{aligned} M_{viscous} &= q_{\infty} S_w \left(CD_c \left(z_c \cos(\alpha) + \left| CG - X_{\frac{mac}{4}_c} \right| \sin(\alpha) \right) \right. \\ &\left. + CD_w \sin(\alpha) \left| CG - X_{\frac{mac}{4}_w} \right| + CD_{fus} \sin(\alpha) \left| CG - X_{\frac{mac}{4}_{fus}} \right| \right) \end{aligned}$$

4.9. Battery performance analysis

In this section, the procedure to determine the viability of this configuration with current battery technology will be described. First, mission will be defined according to criteria extracted from other Urban Air Mobility projects and conventional aircraft. Then, the whole model will be assembled and its structure will be described. Finally, optimizing to obtain the lowest battery mass for each of the Pareto front points will determine the best achievable performance for the current configuration.

4.9.1. Mission definition

The objective of this vehicle is to allow fast displacements between close urban areas using a personal vehicle. To do so, the principal objective is established as travelling 300km in one hour but hovering and transition must also be included into the mission analysis to provide a realistic estimation of the battery needed.

Given the aircraft configuration and the design objective, cruise will be the main focus on the mission, reducing hover time to the minimum possible. Based on urban mobility mission analysis work by NASA (Snyder, 2017), hovering time of 2 minutes at the beginning and 2 minutes at the end of the mission were found to be coherent with urban air mobility requirements. The addition of this hover time in the mission will set up a conservative estimate that accounts for uncertainty, errors during transition modelling and possible inconveniences during flight.

To define cruise altitude, it is necessary to look into other urban air mobility projects and aircraft with similar design objectives such as rotorcraft or the V22-Osprey tilt-rotor(Boeing, 2020). A NASA study(Snyder,2019) defines a mission altitude of 600m for a range of 280km. Meanwhile, the V22 and helicopters like the AgustaWestland AW109(Royal Australian Navy, 2020) or the Robinson R44 (Robinson Helicopter, 2020) present operational ceilings around 7000m, 6000m and 4000m respectively. Lower cruise altitudes than these are thus expected, but for ranges over 500km. This project mission specifications are more similar to the ones defined by Snyder(2019). Considering the extra cruise range, a cruise altitude of 1000m seems appropriate and would allow to relax noise restrictions.

Taking account that transition cannot be modelled until defining the flight control, an estimation of the rate of climb will be taken from light aircraft Cessna 172(AOPA, 2020), which has a best rate of climb around 6.7m/s. The acceleration of the aircraft will be defined as 2m/s^2 based on work by Bacchini and Cestino(2019a). Power at hover and cruise will be obtained from the Pareto front, while the transition will be approximated as a linear variation from the power at hover to the power at cruise for the duration of the transition. Therefore, obtained mission will be the following:

- Hover: 2 minutes. Power at hover.
- Transition: rate of climb of 6m/s and acceleration of 2m/s^2 . 150s at a rate of climb of 6m/s to reach 1000m, 42s accelerating at 2m/s^2 to reach 300km/h. Power variation linearly from power at hover to power at cruise for the 150s. Speed in the transition considered as a linear variation from 0 to 300km/h for the 42 first seconds, then maintained at 300km/h for the rest 125 seconds.
- Cruise: Simplified distance taken as 300km minus the 2 transition distances. Therefore, 276km at 300km/h, 3312seconds. Power at cruise.
- Transition: rate of descent of 6m/s and deceleration of 2m/s^2 . Applies the same as in the first transition.

- Hover: 2 minutes. Power at hover.

4.9.2. Battery and model assembly and optimization

Assembly of the needed components for the optimization is described in this section. Battery model from 4.4 is used as the battery model and mission is described

To perform more realistic estimations, efficiencies of the different elements in the aircraft will be included in the estimations:

Motor efficiency is extracted from current electric motor models. Integral Powertrain SPM 242-76-4630 MGU (Integral Powertrain, 2020) is an electromagnetic motor with high conductivity encapsulation and liquid cooling systems. It has been chosen as it provides both the best power density, over 9kW/kg, and efficiency from all the alternatives checked. From the manufacturer datasheet, its maximum efficiency is expected to be over 98.6%, which will be chosen as the cruise motor efficiency. However, estimations for hover efficiency are not provided. EMRAX, another manufacturer, provides efficiency charts for every motor model as the one presented in Figure 4.34 from model 348CC (Emrax, 2020). Taking into account that the first model provided better efficiency levels, 94% of efficiency at hover can be assumed as viable.

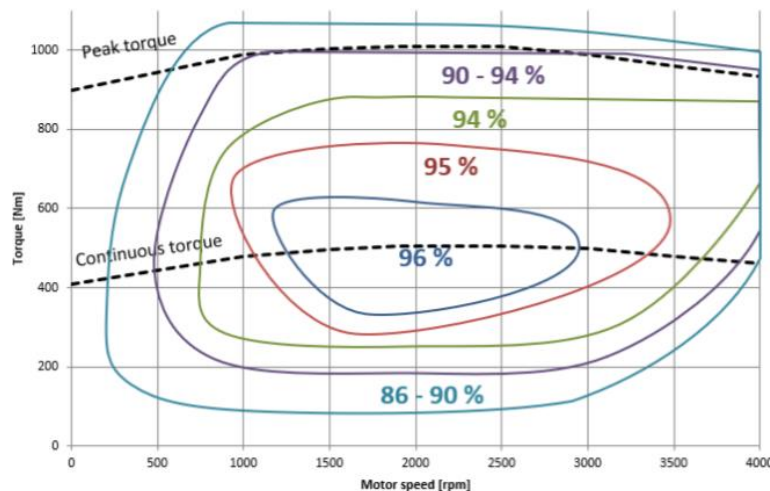


Figure 4.33: Emrax motor performance curves. Extracted from Emrax(2020).

Gearbox efficiency is defined as 98% from Hepperle (2012).

Dever et al.(2015) provided values for electronics efficiency of 93-95%, selected as 94%, and motor inverter efficiency of 97%.

Next, systems power demands must be addressed. For small aircraft, power can be considered to be 5-10% of the power at cruise (Khairy and Venneri, 1997, p299). Selected as 7.5% of power at cruise.

Then, battery model will be introduced, with the battery mass as a function of the number of batteries in series, the number of batteries in parallel and the cell mass. Thermal management, power distribution and structural weight must be accounted for and this will be dependent of the battery mass. Thus, only 80% of the battery mass will be available for energy production (Snyder, 2017). Cell capacity of 3.015Ah, nominal voltage of 3.7V and cell mass of 48g are extracted from a commercial Li-ion cell manufacturer (Hohm Tech, 2020).

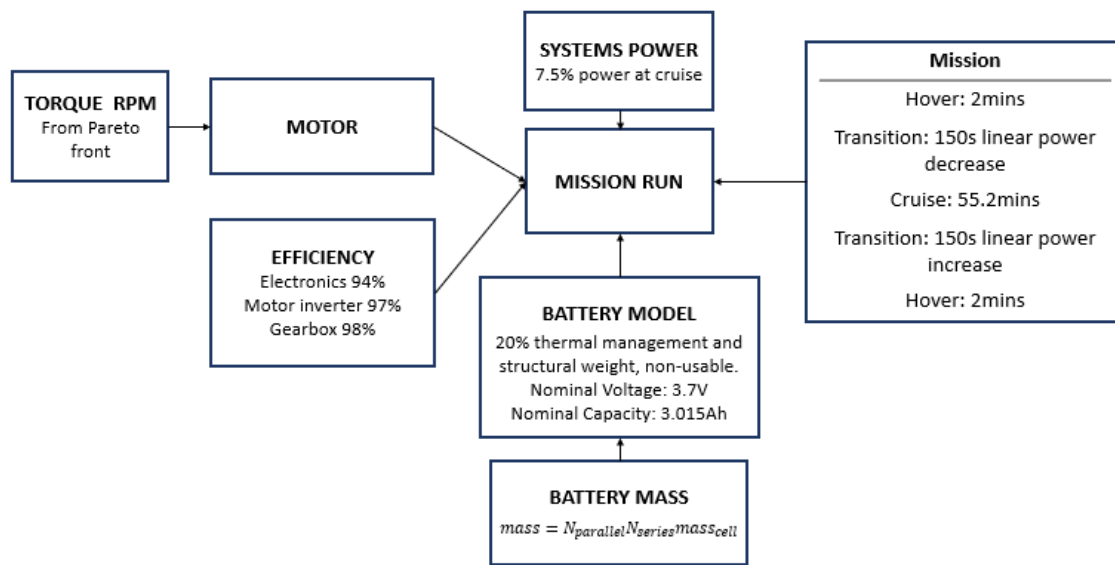


Figure 4.34: Battery performance model assembly.

Finally, an optimization is run to evaluate the best Pareto front point for the mission and the minimum mass required, including a 5% reserve fuel condition. Furthermore, apart of the state of charge of the battery, not surpassing cell maximum current nor cut-off voltage add further constrain with the optimization.

Optimization follows a simple methodology, reducing battery mass until the mission cannot be completed. This simplified model makes no practical difference between number of batteries in parallel and in series, but the last one defines the voltage output. Therefore, number of batteries in parallel will be the parameter to reduce.

5. Discussion of results

5.1. Propeller Optimization

5.1.1. Optimization Results Analysis

A preliminary multi-objective optimization only considering one propeller served to familiarize the author with the algorithms embedded in MATLAB and to further increase understanding of propeller parameters. The two objectives evaluated were power at hover for 1500N of thrust at 0m of altitude and power at cruise at 300km/h for 1500N of thrust at 1000m. No constraints were added into the optimization apart from lower and upper bounds, which are shown in Table 5.1, along with the 17 parameters to optimize.

The parameters are selected so that the geometry needed for QPROP is completely defined by a piecewise spline pchip distribution through 4 different points: 10%, 35%, 70% and 100% of the tip radius.

Forward Propeller	Lower Boundary	Upper boundary
Radius (m)		
Tip radius y_{tip}	0.5	0.65
Pitch θ (deg)		
Root	20	50
35% y_{tip}	$0.4 \theta_{root}$	$2 \theta_{root}$
70% y_{tip}	$0.4 \theta_{root}$	$2 \theta_{root}$
Tip	$0.4 \theta_{root}$	$2 \theta_{root}$
Chord c(m)		
Root	$0.01 y_{tip}$	$0.12 y_{tip}$
35% y_{tip}	$0.4 c_{root}$	$1.6 c_{root}$
70% y_{tip}	$0.4 c_{root}$	$1.6 c_{root}$
Tip	$0.4 c_{root}$	$1.6 c_{root}$
Thickness $\frac{t}{c}$(%)		
Root $\left(\frac{t}{c}\right)_r$	6	20
35% y_{tip}	$0.4 \left(\frac{t}{c}\right)_r$	$1.6 \left(\frac{t}{c}\right)_r$
70% y_{tip}	$0.4 \left(\frac{t}{c}\right)_r$	$1.6 \left(\frac{t}{c}\right)_r$
Tip	$0.4 \left(\frac{t}{c}\right)_r$	$1.6 \left(\frac{t}{c}\right)_r$
Camber $\frac{camber}{c}$ (%)		
Root $\left(\frac{camber}{c}\right)_r$	0	9
35% y_{tip}	$0.4 \left(\frac{camber}{c}\right)_r$	$1.6 \left(\frac{camber}{c}\right)_r$

70% y_{tip}	$0.4 \left(\frac{camber}{c} \right)_r$	$1.6 \left(\frac{camber}{c} \right)_r$
Tip	$0.4 \left(\frac{camber}{c} \right)_r$	$1.6 \left(\frac{camber}{c} \right)_r$

Table 5.1: Parameters and bounds for propeller multi-objective optimization.

The obtained pareto front is observed in Figure 5.1, selecting 3 different points to visualize and evaluate: best cruise, best hover and a middle performance one. Along with the required power, revolutions per minute(rpm) and torque(Q) are indicated in the figure.

First thing to note is that the power increases with speed as the output power is equal to $P_{req} = T \cdot T A S$. The best hover point converges to 35kW while the best cruise point value tends to 140kW. In line with this, hover torque and rpm at hover are always lower than the correspondent for cruise. This applies even for the most efficient cruise point, which presents the worst hover performance for all the Pareto front. However, it must be taken into account that for this vehicle real flight condition, thrust required at hover will be significantly larger than the required for cruise. Therefore, some of the results here cannot be extrapolated to the real flight condition.

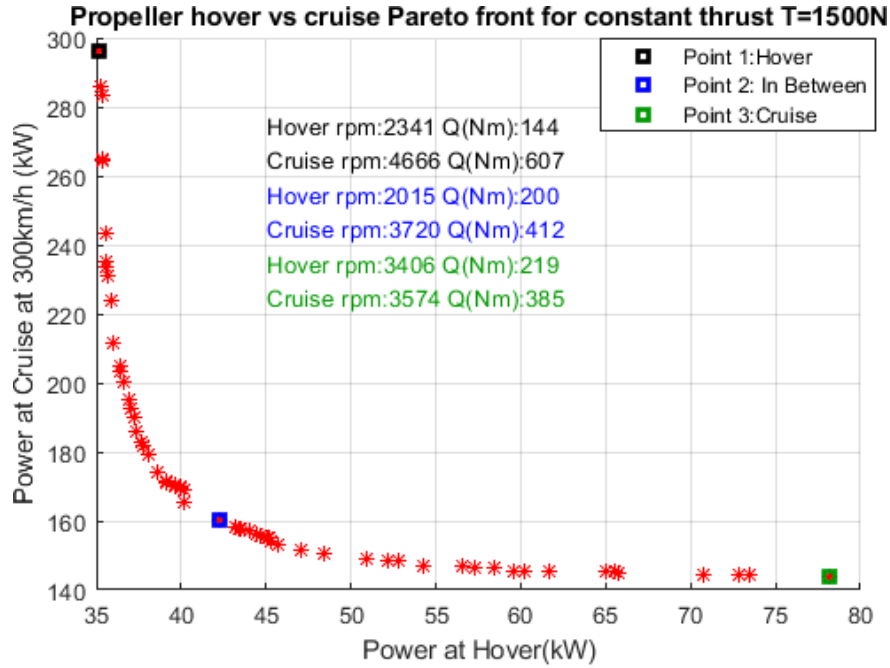


Figure 5.1: Propeller multi-objective optimization pareto front.

Moving to the parameters analysis within the optimization, tendencies are observed in the obtained results, which are presented in Figure 5.2 and Figure 5.3.

In this case, maximum radius is chosen to be the maximum bound for better hover efficiency cases. For the best cruise case however, radius is decreased down to 0.65m. A study relating the effect of propeller diameter and hover efficiency will be presented later in section 5.1.2, in which it will be demonstrated that propeller required power asymptotically tends to 0kW as the diameter increases.

Starting with the chord, both its distribution and values greatly vary depending on what is prioritized. Mean chord decreases as hover performance is reduced, going for considerably low values for better cruise performance and higher values for hover, converging to a different optimal chord value for each of the conditions. The most efficient cruise chord distribution are comparable to the ones used for conventional high speed propellers as the obtained by Brizzolara, Grassi and Tincani(2012), with the maximum chord at around 70% of the radius. Meanwhile, the best hover point chord distribution results similar to the ones obtained for low speed applications like wind turbines, like the obtained by Herráez et al.(2016).

Given the same airfoil and a blade distribution so that lift and drag coefficients distribution is the same for both conditions, generated lift and drag are a function of effective blade speed. For this propeller, both angular speed and airspeed are higher at cruise. Therefore, a lower chord is needed in cruise in order to generate the same amount of thrust.

Regarding the distribution, chord is always smaller at the root and the tip than in the rest of the blade. The low values on the root are due to the small blade speed at low radius, generating less thrust as a result. Meanwhile, at the tip, the Prandtl-Glauert correction accounts for tip losses 3D effects which also reduce the thrust at that location. Therefore, the zone around $r = 0.7y_{tip}$ is where the main portions of thrust and torque are generated. These effects will also influence blade pitch angle distribution.

The velocity profile diagram without including swirl effects, in Figure 4.10, provide guidance on the behaviour of pitch angle distribution. During hover, TAS equals 0 and thus effective blade angle of attack equals to β . On the other hand, TAS at cruise is 83.3m/s and, considering an approximation of $\omega_{prop} = 3500rpm = 366rad/s$, $\alpha_{prop} = \beta_{prop} - \arctan\left(\frac{0.228}{r}\right)$. The combination of r and TAS in this formula provide understanding in the selection of pitch angle. For hover, as $\alpha_{prop} = \beta_{prop}$, β_{prop} should be lower as the induced angle of attack, $\arctan\left(\frac{TAS}{\omega_{prop}r}\right)$, is 0. However, during cruise, a considerably high induced angle of attack is present, needing a higher blade pitch angle to be efficient. The induced angle of attack also depends on the radius: The lower the radius, the higher this induced angle will be as the $\omega_{prop}r$ becomes smaller. Thus, a higher value of β_{prop} will be required for lower radius in order to generate thrust efficiently.

Mean maximum camber and thickness results present higher dispersion, with no clearly defined trend. Maximum camber distribution could be considered somewhat similar for both conditions, with the maximum around 35% of the radius. However, thickness distribution shows discordances in distribution, tending to maximum values at 70% of the radius compared to the maximum at 35% for better hover performance.

It is difficult to provide an explanation for why the selected airfoils are those. Although there are some general trends like higher lift and drag coefficient as maximum camber and thickness increases, properties suffer extreme variation from one airfoil family to the others. In the end, the optimizer will chose an airfoil which is efficient at a certain condition. However, as the two conditions are extremely different, it is not possible to operate at the efficiency peaks at both conditions and trade-offs will be present.

Also, it must be taken into account that not only the lift and drag curves matter, but how the curves are defined, as explained in QPROP theory and formulation (Drela 2007) and in Section 4.3. This last point could be especially relevant as an inaccuracy source due to the somewhat arbitrary way of defining the aerodynamic properties.

Even if QPROP includes some 3D effects and corrections, only 2 dimensional airfoil properties are defined, with no blade sweep influence. Moreover, stall properties are not included in this software, which may extremely condition the results. High blade pitch angles could lead to separation at hover, decreasing accuracy as mentioned by De Leew(2012) in the validation.

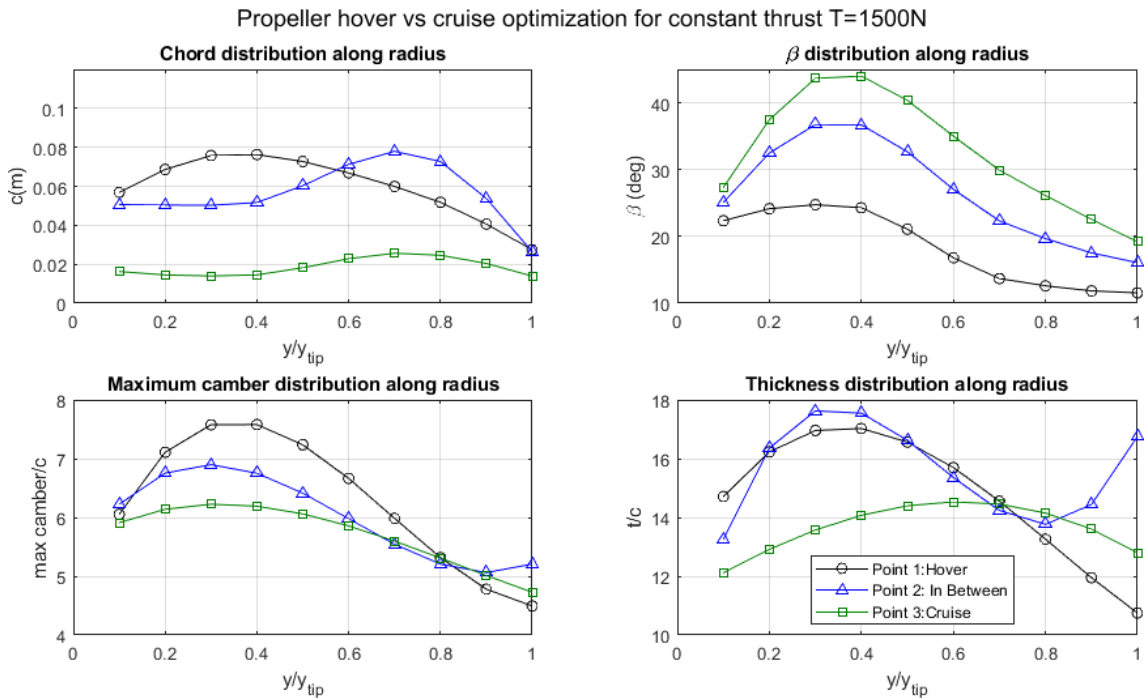


Figure 5.2: Chord, pitch angle, maximum camber and maximum thickness distributions for three different points in the Pareto front obtained from the propellers multi-objective optimization.

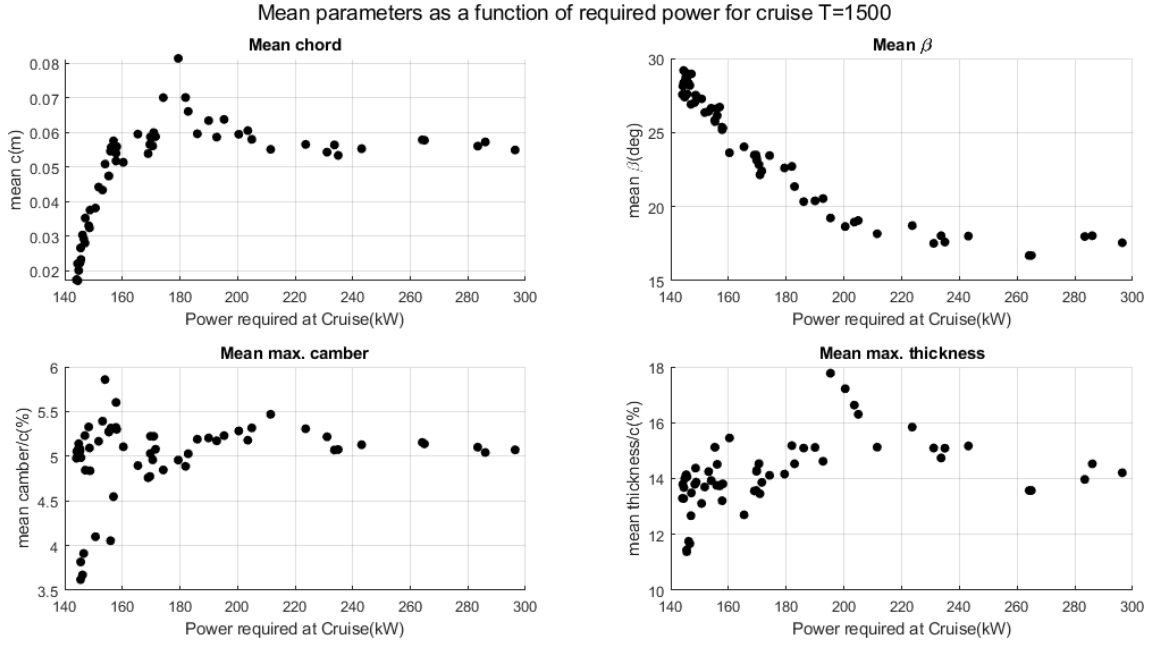


Figure 5.3: Chord, pitch angle, maximum camber and maximum thickness mean values for all the points in the Pareto front obtained from the propellers multi-objective optimization.

Results in this section cannot be generalized, except for β_{prop} , as dependence on the disk loading and thrust required may produce considerable variations. Nevertheless, they provide a good understanding of how propellers work and the relevant parameters within the optimization. All this knowledge will be used in the full aircraft optimization later in Section 5.3.

5.1.2. Propeller efficiency study

Diameter is one of the most relevant parameters in a propeller, as it directly influences two relevant performance parameters, disc loading and solidity. A study of the influence of diameter and thrust on required power at hover is presented in Figure 5.4, performing a single-objective optimization for a cost function of power required at hover at altitude of 0m for different required thrust required and diameter values.

Diameter proves to be extremely important for hover performance, as, for a given thrust, the lower bound on aircraft required power at hover is defined by it. As it increases, not only intercept at 8000N is reduced but so does the slope for thrust increment. Using disk actuator theory, ideal power can be defined as:

$$P_{ideal} = \sqrt{\frac{T^3}{2\rho A}} \quad (5.1)$$

Also, from momentum theory the following equation is obtained.

$$\eta_{prop} = \frac{V_{\infty}}{V_{\infty} + \frac{u}{2}}$$

Where u is the axial velocity increase in the final wake.

Both equations are intrinsically related and explain the same phenomena. For optimum efficiency, the velocity induced to the air should be minimal. This is achieved by increasing mass intake or reducing disk loading. Also, as the speed increases, the requirement for low disc loading becomes less relevant due to the higher value of V_{∞} . Thus, the improvements on efficiency caused by larger diameters will be lower at higher speeds. This will be confirmed in Subsection 5.3.4.

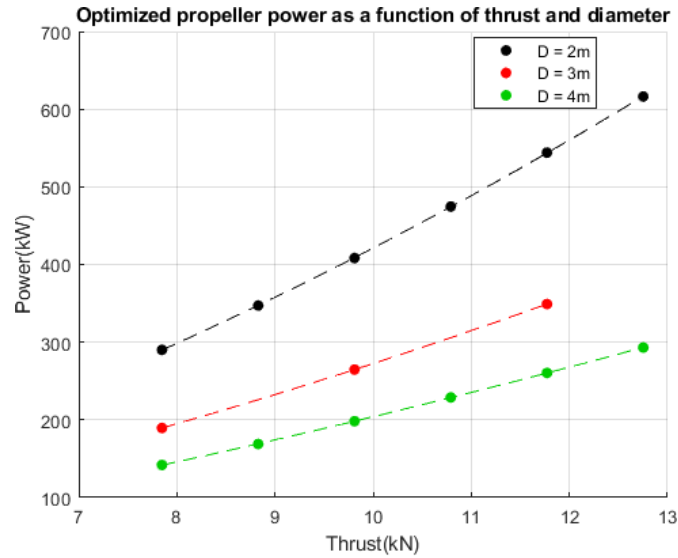


Figure 5.4: Optimized propeller for hover condition at altitude of 0m for different thrust and propeller diameter values.

The data obtained here will be used as a response surface for the full aircraft optimization, fitting a second order function as a function of thrust for each diameter as seen in Figure 5.4.

Diameter also influences propeller solidity σ . The optimum solidity value will provide optimum efficiency for a given airfoil and thrust. Too high solidity will force the propeller to act below the optimum point to generate the same lift and vice versa. Therefore, for optimum efficiency the proper combination of airfoil and solidity must be chosen.

5.2. Airframe Optimization

As it was explained in section 4.8.1, within the whole optimization process there is a block where only the airframe is optimized for minimum drag when longitudinally trimmed. The data obtained with this block is presented in this section and serve as valuable information to increase understanding of the aerodynamic behavior of the aircraft.

The following results are obtained from a multi-objective optimization to minimize drag at 2 flight conditions, cruise at 160km/h and cruise at 300km/h at altitudes of 0m and 1000m respectively. Parameter bounds on Table 5.2 are obtained from design considerations and iterations with the design. Limit on angle of attack below 10deg are also imposed.

Airframe	Symbol	Lower Boundary	Upper boundary
Wing			
Root chord(m)	C_{r_w}	1	4
Tip chord(m)	C_{t_w}	1	4
Leading edge sweep (deg)	Λ_{le_w}	0	45
Root angle of attack (deg)	α_{r_w}	0	2.2
Wing leading-edge X position	X_{le_w}	5	$10 - C_{r_w}$
Root Max. Camber (%)	$\frac{camber_{max}}{c} r_w$	0	3
Tip Max. Camber (%)	$\frac{camber_{max}}{c} t_w$	0	3
Canard			
Root chord(m)	C_{r_c}	0.5	1
Semispan(m)	b_c	1	3
Root angle of attack (deg)	α_{r_c}	0	2.5
Z position(m)	z_c	0	1
Longitudinal CG Position			
(from nose)	X_{CG}	4.5	5.5

Table 5.2: Optimization parameters with correspondent upper and lower boundaries.

The Pareto front obtained was one point, as the variations of the values within the drag values were below 0.1%. For the full aircraft optimization, the 'stall' condition will be defined as being able to fly at 160km/h at 0m for an angle of attack below 10deg considering thrust angle of attack is 0. This will be imposed as a Yes/No constrain, obtaining a high value for both cost functions if it is not

fulfilled. This optimum point was compared to the result obtained from a single objective optimization only considering drag at cruise at 300km/h at 1000m as a cost function imposing no constrains. This comparisons can be observed in Figure 5.5 and Table 5.3.

First appreciation is the increased size of both the wing and canard when adding the 160km/h condition. Meanwhile, both the wing and the airframe CGs are moved backwards, specially the former. Canard z position is modified from 0 to 1 with the 'stall' constrain, adding a small component of positive moment. Finally, the wing root angle of attack is increased from 0 to 1.2deg.

The stall speed is given by $v_s = \frac{2W}{\rho S C_{L_{max}}}$. By increasing the wing and canard surface, the surface term on the denominator is increased, but the aspect ratio is reduced and thus $C_{L_{\alpha}}$ and K are negatively impacted. Wing root angle of attack is increased for a higher C_{L_0} value. All these changes lead to a lower trim angle of attack α_{trim} , both to reduce induced drag but mainly to have a wider margin of angle of attack until reaching 10deg. However, as a drawback, drag becomes considerably higher, a 22%, mainly due to the increase in size of the wing and canard surface.

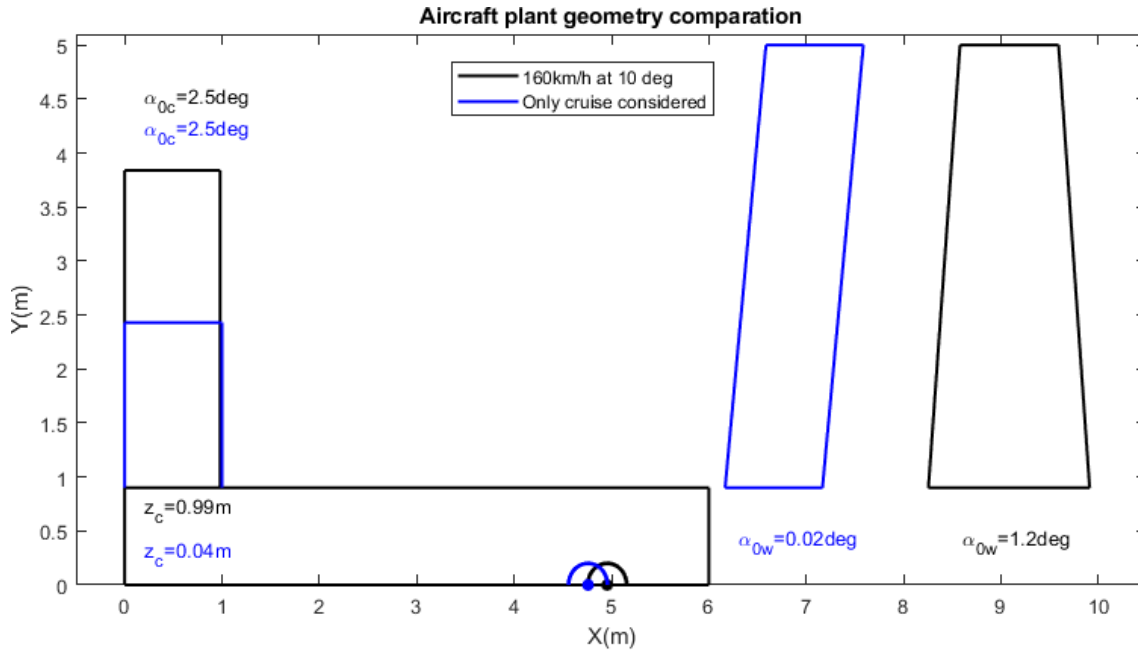


Figure 5.5: Aircraft geometry comparison, Single-objective Cruise 300km/h(blue) vs Multi-objective Cruise 300km/h and Cruise 170km/h(black).

	Single-objective Cruise 300km/h	Multi-objective Cruise 300km/h Cruise 170km/h
$S_w (m^2)^*$	10	13.3
$S_c (m^2)^*$	6.7	9.8
C_{L0}	0.38	0.48
$C_{L\alpha} (rad^{-1})$	5.4	5.3
C_{m0}	-0.063	0
$C_{m\alpha} (rad^{-1})$	0.090	-0.23
Drag at 300km/h(N)	1085	1331
C_{D0}	0.021	0.021
K	0.037	0.047
$\alpha_{trim} (deg)$	2.4	-0.19

Table 5.3: Airframe optimization results for the single-objective optimization only considering cruise and the multi-objective optimization considering stall limitations.

*Considered as the plan area of the effective wing, without including the fuselage

The main conclusion in this section is the trade-off between stall speed and drag at cruise. Even if the aircraft is able to maintain hover with the tilting propellers, certification and safety issues could limit operation in case of propeller fail. By reducing the stall speed, the flight envelope could be ampler, adding more versatility into the vehicle.

5.3. Full aircraft optimization

Optimization of the full aircraft is performed following the model assembly presented in Section 4.8. During the process of optimization, a certain degree of iteration was required, resulting in the introduction of the changes presented in section 5.3.1. The optimization results are presented and discussed in Section 5.3.2. Next, a sensibility analysis for variations from the optimum in the most relevant parameters is introduced in Section 5.3.3. Finally, Section 5.3.4 discusses the relation between diameter, center of gravity and efficiency.

5.3.1. Previous configurations insights

Before arriving to the ‘final’ configuration, other configurations with different parameters were tested, each of them drawing conclusions that led to modifications in the configuration, process and variables. From these trials, the valuable insight gained is presented in the following paragraphs:

Initially, wing chord was fixed to 7m in order to decrease the number of parameters. However, this proved to provide an incredibly low aerodynamic efficiency $\frac{L}{D}$, below 5, as a considerably high wing area of around 50m² was needed to provide enough lift. The cause for these results was the low aspect ratio, which had a great negative impact on $C_{L\alpha}$ and K while the 2D drag correction made parasitic drag enormously high due to the huge required surface.

Some variables used in the response surface tended to 0 or to one of the bounds and, therefore, were eliminated to increase accuracy. Twist for example tended to 0 in every optimization, becoming a non-relevant parameter to optimize. This may be due to Oswald factor not including any effects from it and stall characteristics not being studied within this optimization.

Canard z position respect to fuselage did not produce any viscous drag correction into the moment, a problem that was mentioned during AVL limitations section. Therefore, in order to account for canard z coordinate, the viscous drag effect on moment was added as a force applied at $\frac{mac}{4}$ of each lifting surface. Still, this does not include moment generated within the own airfoil due to pressure distribution and further validation of this method is required.

Originally fixed at 4.8m, it was noticed that CG was one of the most important parameters in the optimization and was implemented as an optimizable variable along with the propellers position.

A sensible population size must be chosen so the genetic algorithm works properly. Too high population sizes, over 600, will make the optimization inspect an ampler spectrum of the domain but will take an incredibly high amount of time

to converge. On the other side, a too low population size will make it converge in non-optimal results, requiring to increase the number of stall generations.

It has been demonstrated that response surface methodology accuracy is limited, especially for some of the aeroderivatives. To account for this, the possibility of enhancing results obtained by the Pareto front is present by applying a pattern search multi-objective optimization with the full aircraft model to the points in the response surface pareto front.

XFOIL 2D drag correction tended to overpredict zero-lift drag coefficient, obtaining values around 0.042 while expecting values from a range of 0.015 to 0.035 from military canard aircraft (Heffley and Jewell, 1972).

The great number of variables involved and the fact that only CG position proved to be coupling cruise and hover made the optimization inefficient and time-consuming when starting from 0. Even with different convergence criteria, it was found during the sensibility analysis that the obtained results were not even locally optimum. Therefore, a new method was devised to reduce running time and obtain more sensible results. This method reduced convergence time and results proved to be locally optimum after sensibility analysis. Method was explained in Section 4.8.

The final parameters have been chosen according to the limitations of the tools used, studies about the effect of the parameters on results and the fact that AVL must be modelled as a response surface. Some of the cases that have been eliminated are presented here: Wing and canard twist are not included as its main aerodynamic contribution are related to stall and lift distribution spanwise, not capture with the current model. Furthermore, limitations on AVL not capturing viscous effects lead to non-reliable results, motivating the decision of eliminating airfoil thickness from the optimization study. This study was performed for every airframe parameter in different points within the optimization domain, with thickness being the only parameter with such random behavior, making it impossible to model it as a response surface.

5.3.2. Full aircraft optimization results for back propeller diameter of 2m.

The results of the multi-objective genetic algorithm combined with the pattern search method for the full aircraft model are presented in this section. As mentioned in Section 4.8, population is pre-seeded with the Pareto front obtained from the uncoupled airframe and propeller optimizations. Power required at cruise at 300km/h and 1000m of altitude and hover at 0m are again evaluated as the cost functions:

$$\text{Cost function 1} = P_{cruise} r p s_{cruise}$$

$$\text{Cost function 2} = P_{hover} r p s_{hover}$$

An additional manual constrain was added, which assign a high cost if the conditions is not met. It is the same 'stall' condition mentioned in Section 5.2: Stall speed is defined as being able to fly at 160km/h at 0m only considering airframe aerodynamics and 0deg propeller angle of attack.

Full aircraft optimization involves 33 parameters: 11 for the airframe, 18 for the propeller and 3 for the propellers and aircraft CG position. These parameters have been chosen according design considerations and the insights gained through experience mentioned in section 5.3.1

Airframe	Symbol	Lower Boundary	Upper boundary
Wing			
Root chord(m)	C_{r_w}	1	4
Tip chord(m)	C_{t_w}	1	4
Leading edge sweep (deg)	Λ_{le_w}	0	45
Root angle of attack (deg)	α_{r_w}	0	2.2
Wing leading-edge X position	X_{le_w}	5	$10 - C_{r_w}$
Root Max. Camber (%)	$\frac{camber_{max}}{c} r_w$	0	3
Tip Max. Camber (%)	$\frac{camber_{max}}{c} t_w$	0	3
Canard			
Root chord(m)	C_{r_c}	0.7	1.2
Semispan(m)	b_c	1	4.1

Root angle of attack (deg)	α_{rc}	0	2.5
Z position(m)	z_c	0	1

Propellers	Lower Boundary	Upper boundary
Radius (m)		
Tip radius y_{tip}	0.55 (forward) 1(back)	0.7 (forward) 1 (back)
Pitch θ (deg)		
Root	20	50
35% y_{tip}	$0.4 \theta_{root}$	$2 \theta_{root}$
70% y_{tip}	$0.4 \theta_{root}$	$2 \theta_{root}$
Tip	$0.4 \theta_{root}$	$2 \theta_{root}$
Chord c(m)		
Root	0.8	0.12
35% y_{tip}	$0.4 c_{root}$	$1.6 c_{root}$
70% y_{tip}	$0.4 c_{root}$	$1.6 c_{root}$
Tip	$0.4 c_{root}$	$1.6 c_{root}$
Thickness $\frac{t}{c}$(%)		
Root	6	20
35% y_{tip}	$0.4 \left(\frac{t}{c}\right)_r$	$1.6 \left(\frac{t}{c}\right)_r$
70% y_{tip}	$0.4 \left(\frac{t}{c}\right)_r$	$1.6 \left(\frac{t}{c}\right)_r$
Tip	$0.4 \left(\frac{t}{c}\right)_r$	$1.6 \left(\frac{t}{c}\right)_r$
Camber $\frac{camber}{c}$ (%)		
Root	0	9
35% y_{tip}	$0.4 \left(\frac{camber}{c}\right)_r$	$1.6 \left(\frac{camber}{c}\right)_r$
70% y_{tip}	$0.4 \left(\frac{camber}{c}\right)_r$	$1.6 \left(\frac{camber}{c}\right)_r$
Tip	$0.4 \left(\frac{camber}{c}\right)_r$	$1.6 \left(\frac{camber}{c}\right)_r$
Thrust		
Trim forward flight(N)	Airframe Drag- 250	Airframe Drag+50

Longitudinal CG Position (from nose)	Symbol	Lower Boundary	Upper boundary
Aircraft (m)	X_{CG}	4.6	5.3
Forward Propeller(m)	X_{Fprop}	2.5	4.5
Back Propeller(m)	X_{Bprop}	6.6	8

Table 5.4: Full aircraft optimization parameters and bounds.

Obtained Pareto front shape is similar to the one obtained when only the propeller was evaluated, compare Figure 5.1 and Figure 5.6. Airframe geometry has no influence on hover except for the CG position, limiting coupling to propellers geometry and CG positions of the components. Propellers CG position can be modified so that range of forward-backward thrust distributions at hover can be selected, although the maximum is limited to 60% of the thrust provided by the back propeller. This is due to the conservative restrictions in propellers longitudinal CG position.

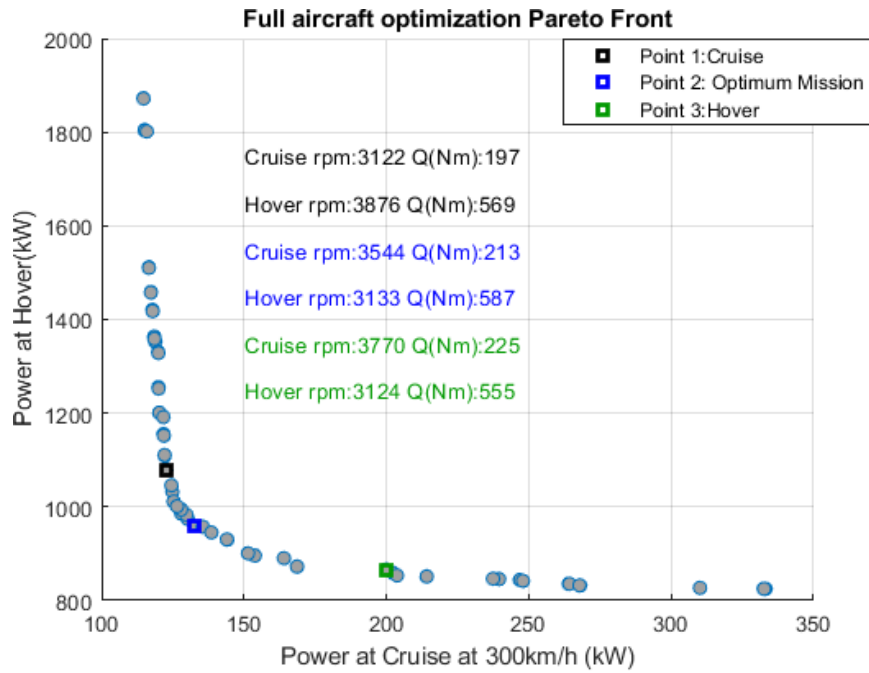


Figure 5.6: Full aircraft optimisation Pareto Front.

Some of the previous results from the propeller optimization in section 5.1 are repeated here and most of the justifications given can be applied here. Thus, explanations about the optimization in this section will be maintained brief and if further information is desired Section 5.1.1 can be consulted.

The trade-off between hover and cruise comes for the impossibility of operating at the optimal blade efficiency $\frac{L_{blade}}{D_{blade}}$ at the two conditions. The vast variety of the points tend to the maximum radius, as small reductions in diameter produce a severe reduction in hover efficiency, as explained in Section 5.1.3. Optimal pitch angle for hover will be substantially lower than the one for cruise due to the induced angle effect. This difference in induced angle is around 26deg at the 70% of the radius of the forward propeller rotating at 3600rpm. It also varies depending on the radius, being around 48deg higher for hover at 30% of the radius and

18deg at the tip for the same operating conditions as before. This explains the pitch angle distribution along the radius.

In this case, the difference in thrust at each condition serves to explain the different chord values. Comparing the thrust required at cruise to thrust required at hover ratio for the forward propellers $\frac{T_{Fhover}}{T_{Fcruise}}$, the ratio may range from $\frac{T_{Fhover}}{T_{Fcruise}} = 7.8$ for a 50%/50% distribution of thrust at hover to $\frac{T_{Fhover}}{T_{Fcruise}} = 6.2$ for a 60%(by back propeller)/40%(by forward propeller) distribution. To account for such a difference in required thrust, the chord for a more efficient hover is larger than for a more efficient cruise. At the same time, the maximum is maintained at around 70% of the radius to increase thrust generation for every point in the pareto front.

Thickness and camber distributions and mean patterns seem irregular and would require an in-depth analysis of the airfoil characteristics and how they are inputted into QPROP. However, in line with the commentaries made in Section 5.1.3, the optimal airfoil depends on solidity. If solidity is decreased, either rotational speed is increased or airfoils provide a higher lift coefficient to produce the same thrust. Looking at Figure 5.6, rotational speed at cruise is reduced as the power at cruise decreases, while pitch angle rises. Therefore, airfoil selection should aim for an airfoil that produces higher lift coefficient values at lower angles of attack. Normally, high-cambered airfoils comply with that description, but this cannot be generalized as properties vary considerably from one airfoil to another.

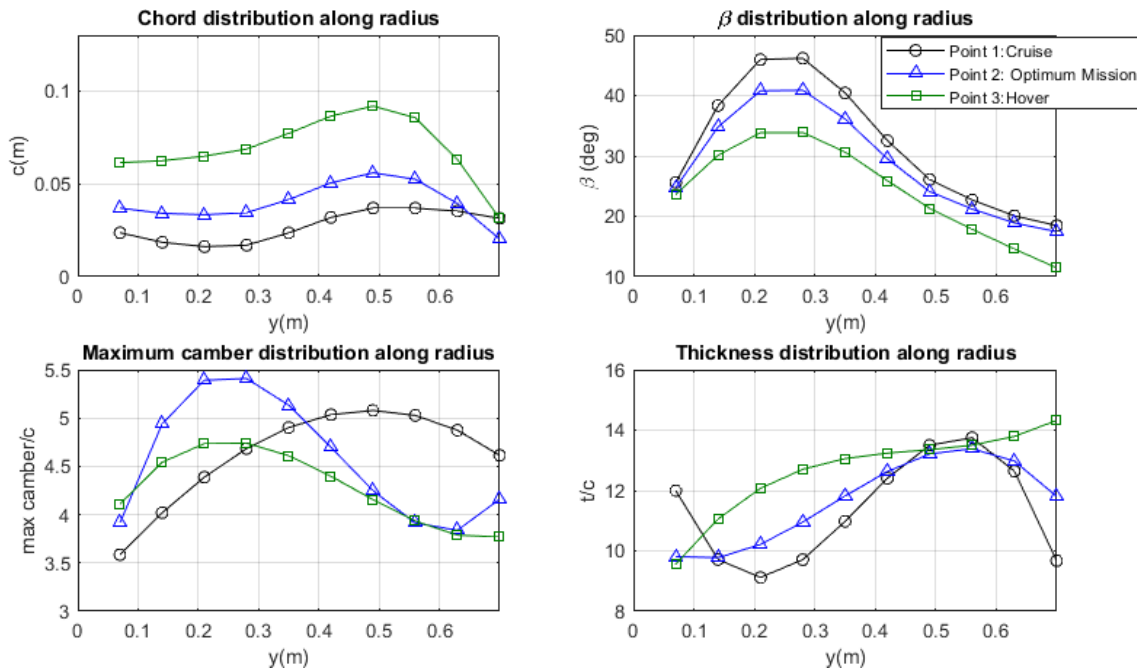


Figure 5.7: Chord, pitch angle, maximum camber and thickness distribution for the three points selected from the Pareto front in Figure 5.6.

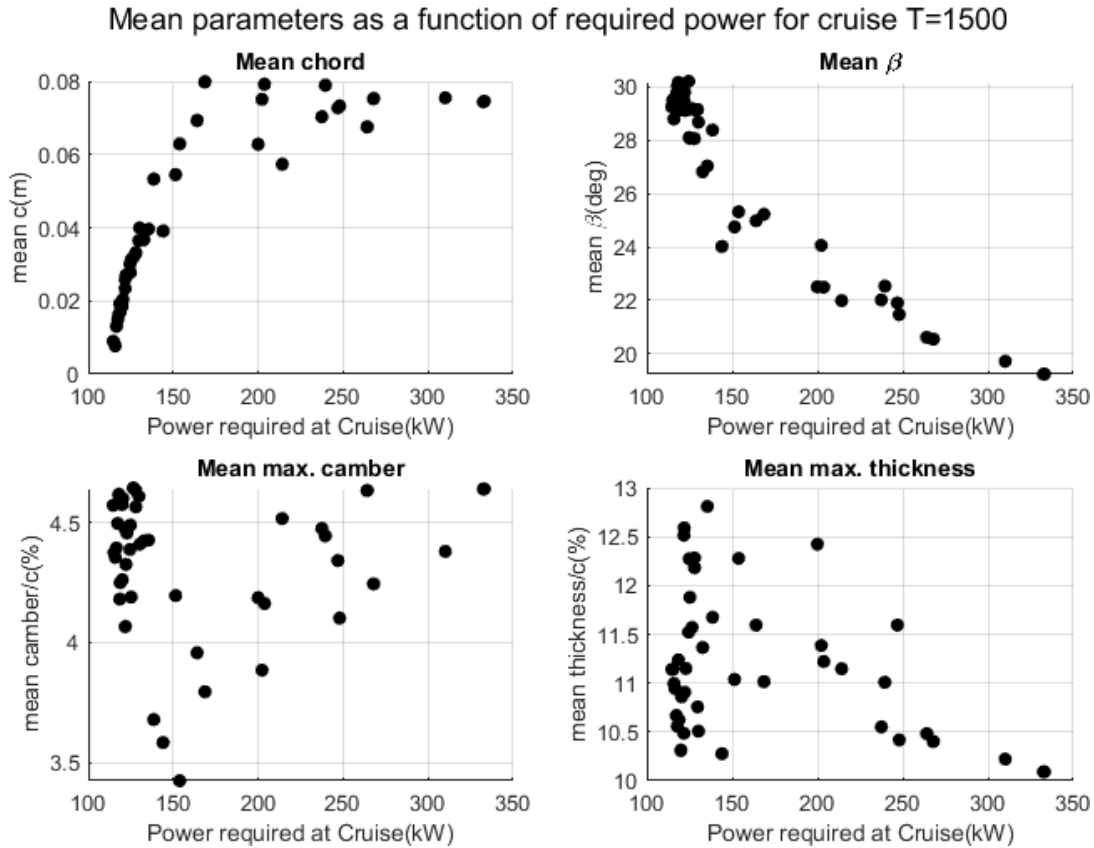


Figure 5.8: Chord, pitch angle, maximum camber and thickness mean values as a function of power required at cruise for all the points from the Pareto front in Figure 5.6.

Coupling between the propeller geometry and percentage of thrust by each propeller defines the trade-off between cruise and hover performance. Figure 5.9 shows the tendency to reduce the amount of thrust provided by the back propeller during hover for a better hover performance, tending to equally split the generated thrust. Meanwhile, for better cruise performance, higher percentage of thrust generation tends to be delegated to the back propeller, tending to the higher limit of 60% of thrust generated by the back propeller.

The cause is found in the fact that, once the forward propeller becomes orientated to be more efficient at cruise, the performance at hover gets negatively affected. To compensate for it, the percentage of thrust provided by the forward propeller tends to be decreased, as it is more efficient to force the back propeller to provide a higher percentage of the total thrust.

However, when the forward propeller is designed to be more efficient at hover, back propeller is alleviated from thrust generation, tending to an even thrust distribution. As it was shown in Figure 5.4, the slope and intercept terms of the hover thrust as a function of power greatly decreases for increments in propeller diameter. Therefore, each of the forward propellers will always tend to provide less thrust than the back propeller.

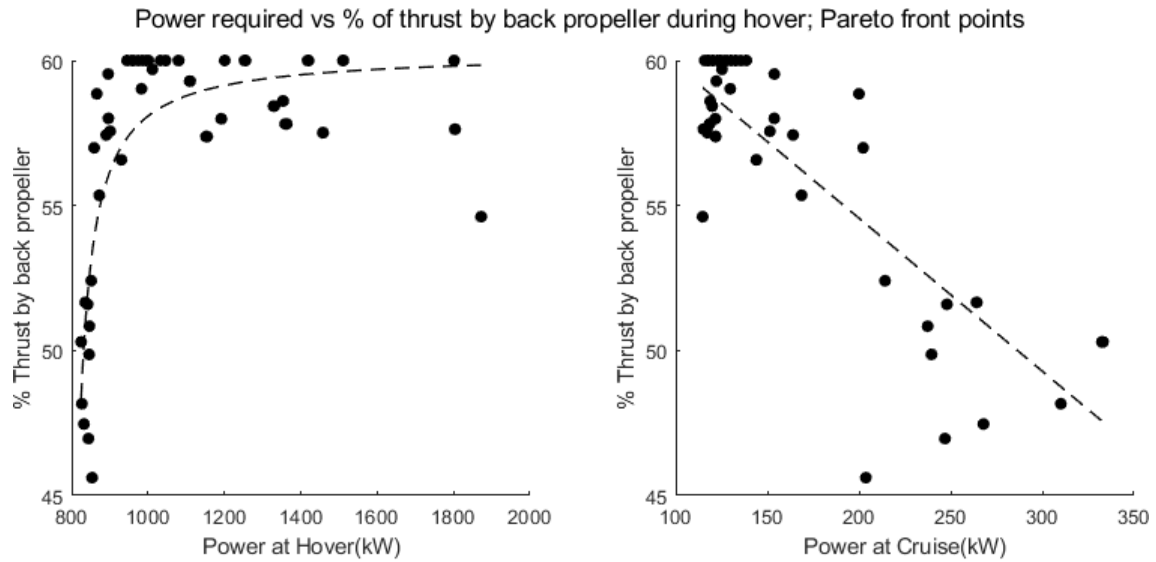
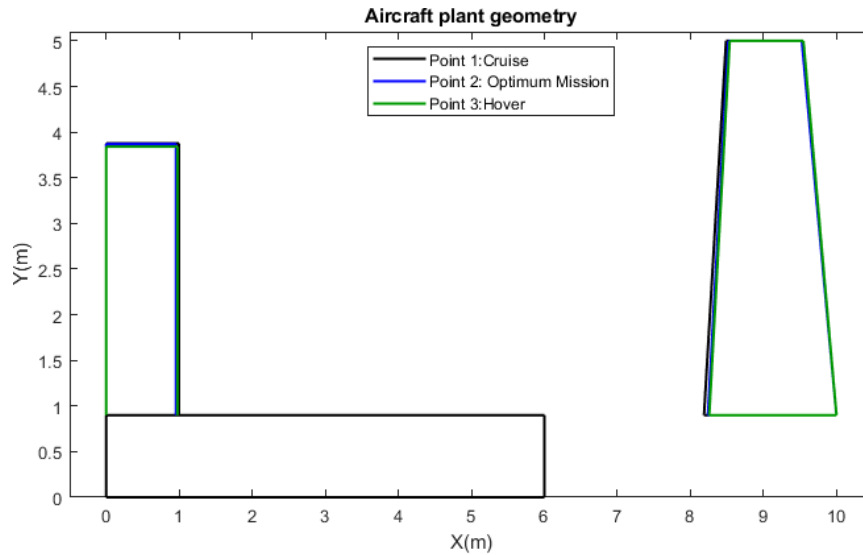


Figure 5.9: Percentage of thrust generated by the back propeller during hover as a function of power at hover(left) and power at cruise(right).

No significant variations in the three points aircraft geometry are appreciated when compared to the aerodynamically optimized airframe, as observed in Figure 5.10. In the same line, thrust and drag cruise values variation along the Pareto front are negligible, with a difference between maximum and minimum below 15N.



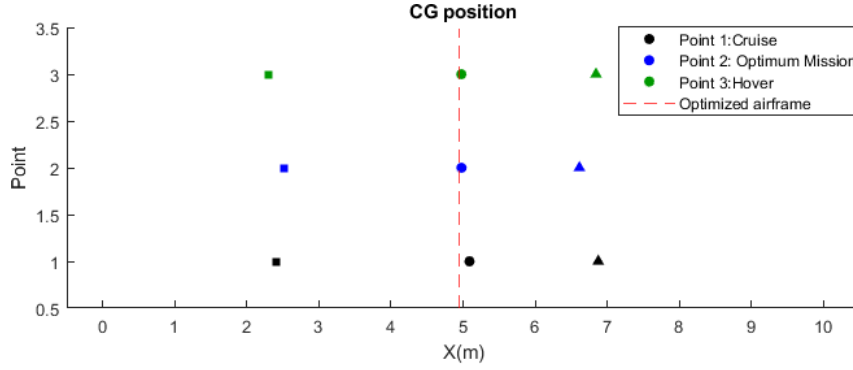


Figure 5.10: Airframe geometry(up) and CG location(down) for the multi-objective full aircraft optimization.

The values of the aero-derivatives seem constant throughout the whole pareto front, as observed in Figure 5.11. That is also the case for each of the parameters within the optimization, even for similar power at cruise values, results are scattered. Therefore, a degree of uncertainty is allowed for similar performance values.

As mentioned in the response surface error analysis from section 4.7.3, some of the aero-derivatives modelling is less accurate than others. In this case C_{m0} is the value with the biggest differences with the full model, although the error can be considered acceptable, not causing big deviations from the response surface results.

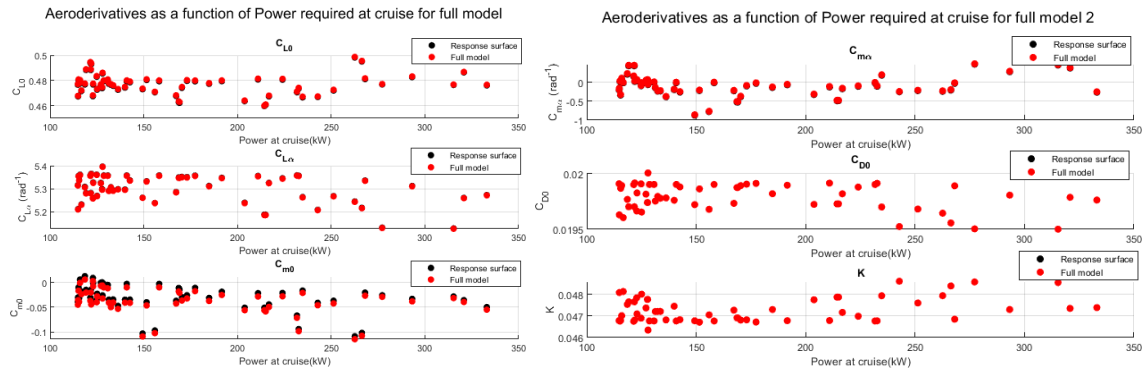


Figure 5.11: Aeroderivatives as a function of power at cruise for full model optimization .

The scattered values obtained for the aero-derivatives translate into a scatter in the trimming angles and the correspondent uncertainty. Also, the same response surface inaccuracy is present here, finding slight variation between response surface and full model results, although these seem to be irrelevant for most of the cases.

The most relevant trait is the small contribution to lift of around 50N from the forward propeller, as its angle of attack tends to 2.5/3deg for practically every value in the Pareto front. The reasoning behind this will be explained in the

performance study in Section 5.4.1.1. Variation for angle of attack and elevator angle is considerably small, 0.2deg and 0.5deg respectively for most of the values. Thus, it can be stated that the scatter within the optimization does not translate into big differences in the trimming angles.

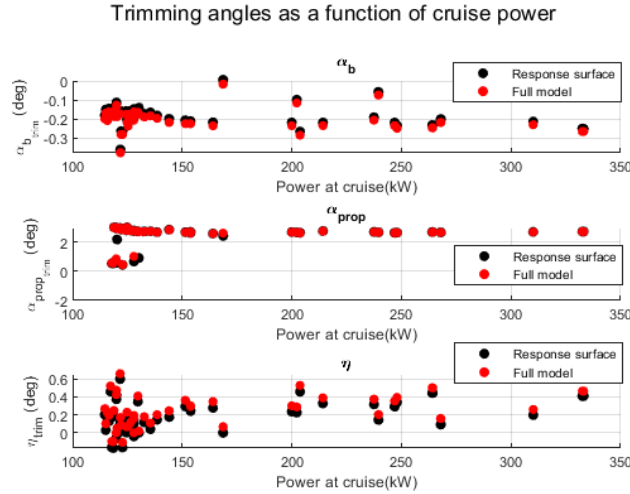


Figure 5.12: Trimming angles (airframe angle of attack, propeller angle of attack and elevator deflection) as a function of power at cruise for the full model optimization .

5.3.3. Sensibility analysis

The sensibility analysis has two objectives: 1. Increasing understanding of the current configuration and obtain more relevant parameters. 2. Validating the model, checking if the obtained results match with expected physics from the model.

The results here show the parameters which either had the biggest impact on performance or served to validate result. The methodology followed was varying each of the parameters while leaving the other constant for one chosen point in the Pareto front. Aerodynamic and propeller calculations and trimming were calculated for each of the modified points. In the case of the span, root and tip chords are modified so that the same wing surface is maintained.

For the span, the limitations was originally on 10m to fit in conventional heliports. In the case of relaxation of the constrain or the inclusion of folding wingtips, the effects would be considerably positive, as seen in Table 5.4. Not only drag can be reduced by 10% by increasing span 2 meters, but also stall speed can further be decreased. This reduction in stall speed could lead to further drag reduction if

original stall speed is maintained, due to the stall speed-drag at 300km/h trade-off mentioned before.

Variation (%) Except stall speed.	Span	
	Span =11m	Span=12m
C_{L0}	+8%	+14%
$C_{L\alpha}$	+10%	+17%
C_{D0}	+2%	+2%
K	-18%	-32%
$v_{stall}(km/h)$	165	160
Original 175km/h		
Drag	-5%	-10%

Table 5.5: Span sensitivity study for the final D=2m configuration.

Meanwhile, variation in the airframe CG can give a measure of the effect of uncertainty in mass distribution and also serve as a validation method of the modelling capabilities. Wide deviations in the CG position of -0.5 would lead to approximate increments in drag and power at hover of around 10%. The expected effect on the moment coefficients works as expected, with the moment becoming more negative and statically stable as the CG is moved forward.

	CG position					
	Original	-0.5m	-0.2m	-0.1m	+0.1	+0.2m
C_{m0}	-0.04	-0.22	-0.11	-0.076	-0.006	0.03
$C_{m\alpha}$	-0.22	-2.17	-1	-0.61	0.17	0.56
Drag(N)	1250	+123	+49	+24	-6	+7
$\alpha(deg)$	-0.1	-0.4	-0.16	-0.08	+0.1	+0.18
$\eta_{elevator}(deg)$	0	+2.2	+1.2	+0.8	-0.2	-0.5
Power at hover variation(%)		+10%	+2.5%	+1%	0%	-1%

Table 5.6: CG position sensitivity study for the final D=2m configuration.

Another uncertainty check would be the study of the change in mass, as this could vary during the whole design and even during the operation if the number of passengers is not 3. Obviously, decreasing mass would reduce the required drag and angle of attack during cruise as well as the stall speed. Variation in power required at hover seems close to $T^{\frac{3}{2}}$ according to disk loading equation (Eq 5.1) from Section 5.1.2.

	Mass				
	1500 kg	1800 kg	1900 kg	2100 kg	2200 kg
Drag(N)	-231	-100	-50	+54	+110
$\alpha(deg)$	-1.5	-0.6	-0.3	+0.3	+0.6

Power at hover variation(%)	-36%	-15%	-8%	+8%	+17%
$v_{stall}(km/h)$					
Original	150	163	168	177	181
175km/h					

Table 5.7: Mass sensitivity study for the final $D=2m$ configuration.

Finally, as mentioned before, restrictions could be applied on the propeller tip speed so transonic regime is not reached. An additional multi-objective optimization with the same structure as the previous chapter but including a constrain on the propeller tip Mach speed was performed. The results on Figure 5.13 show the negative effect of transonic constrains on performance, doubling the power required at cruise and slightly increasing the required during hover. However, as cruise altitude is 1km, noise requirements at that condition could be relaxed.

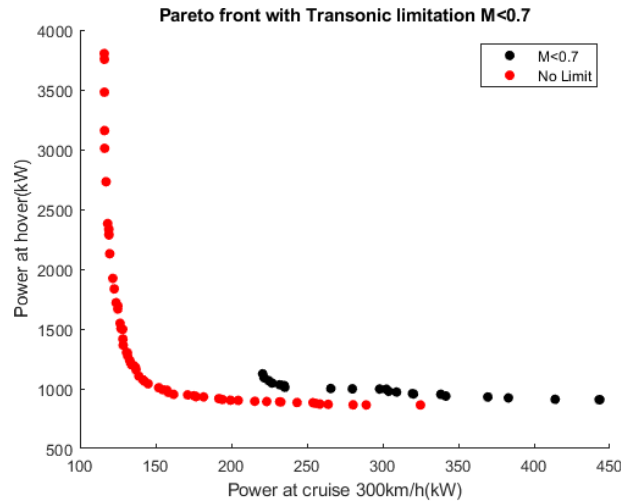


Figure 5.13: Comparison of optimization results. Red, optimization results as seen in 5.3.2. Black, optimization with transonic limitation constrain for blade tip Mach below 0.7.

The results presented here along with the propeller efficiency study in 5.1.2 present possible solutions to reduce the power required during the operation of this aircraft. Also, the variations of CG position and mass give an estimation for possible uncertainty due to mass and its distribution.

5.3.4. Optimization results for variations in propeller diameter and CG.

The benefit of this configuration is its relative capability to uncouple hover and cruise, as the back propeller can be optimized for hover while the forward propellers can be aimed at cruise performance. Furthermore, thrust distribution during hover can be altered so that the back propeller provides a higher percentage of total thrust. This allows for the front propeller to be designed for more efficient cruise while limiting the negative effect on hover performance. However, further considerations into the location and size of the propellers must be taken into account for sensible results. Optimization results for variations in the bounds of diameter and CG will be presented in this section.

Previous configuration limited propeller size to 1.4m and 2m for forward and backward propellers respectively. It was demonstrated in 5.1.2 that, by increasing propeller diameter hover efficiency could improve. However, aircraft and propellers size and its CG location must be considered. If back propeller size is increased, back propeller will need to be located further away from the CG for a realistic design. A limit of the tip of the back propeller at least in 5.8m seems acceptable, considering the mass distribution needed for a CG position around 4.8m. Thus, if diameter is 3m, lower bound of the back propeller CG location will be moved back to 7.3.

It was also shown in the previous optimization in Section 5.3.2 that, for better cruise performance, thrust was distributed in a 60/40 proportion between back and forward propellers respectively, which was defined as the limit. To be able to reach this optimum thrust distribution, ratio between forward propeller and back propeller distances to the CG should be $\frac{X_{Fprop}}{X_{Bprop}} = \frac{3}{2}$. With the new lower bound on the back propeller CG location on 7.3, forward propeller should be located around 1.55m. This location cannot be achieved without superposing canard and forward propeller.

Therefore, increasing propeller diameter add further considerations into the optimization, as the better hover efficiency might be overridden by the new thrust distribution during hover.

Different configurations were tested varying propeller diameter and cg location. Variant 1 fixed propeller diameter to 3m and 2m for the backward and forward propellers respectively. Lower bound for the back propeller longitudinal CG position is 7.3. Lower bound for the forward propeller longitudinal CG position is set so superposition of canard and forward propeller is not possible. Variant 2 was similar to Variant 1, but the forward propeller diameter could vary between 1.3m and 2m. Variant 3 was equal to Variant 2, but superposition of the canard and the forward propeller the forward propeller. Thus, lower bound of longitudinal CG position of forward propellers was set to 1m. This could represent a configuration where the forward propellers are in front of the canard or in

between, like in the Aston Martin Volante concept. The objective was to observe the effects of wider margins for the CG locations.

Longitudinal CG Position (from nose)		Variant 1	Variant 2	Variant 3
		Lower Boundary/ Upper boundary	Lower Boundary/ Upper boundary	Lower Boundary/ Upper boundary
	Tip radius(m)	1/1 (forward prop) 1.5/1.5(back prop))	0.65/1 (forward prop) 1.5/1.5 (back)	0.65/1(forward prop) 1.5/1.5 (back prop)
	Aircraft (m)	4.5/5.3	4.5/5.3	4.5/5.
	Forward Propeller(m)	$(C_{r_c} + y_{tip_{FPProp}})/4.5$	$(C_{r_c} + y_{tip_{FPProp}})/4.5$	1.4/4.5
	Back Propeller(m)	7.3/8.3	7.3/8.3	7.3

Table 5.8: Variant configurations boundaries during the optimization.

Results for the 4 configurations' Pareto fronts are presented from Figure 5.14 and Figure 5.15. Improvements compared to the original design are considerable for hover performance with around a 30% increase in efficiency. On the other side, best cruise efficiency is increased by less than a 3%. These results are in line with the explanations provided in Section 5.1.2, as the benefit of lower disk loading is more pronounced on hover efficiency than on cruise.

Differences between the results for the three Variants are negligible for the best cruise and hover points. However, in the zoomed region in Figure 5.14, the positive effect of wider margins in CG location can be noted. In some points in that region, an increase in efficiency around 5% for both cruise and hover is observed.

Another interesting observation is the comparison of Variant 1 and Variant 2 results. Variant 2 margins are wider and contain Variant 1 domain. Even though differences are relatively low in magnitude, it is observed that efficiency obtained by Variant 2 is lower than the obtained in Variant 1. This proves the fact that, by increasing the number of variables in an optimization, confidence in the convergence to the optimum can be reduced.

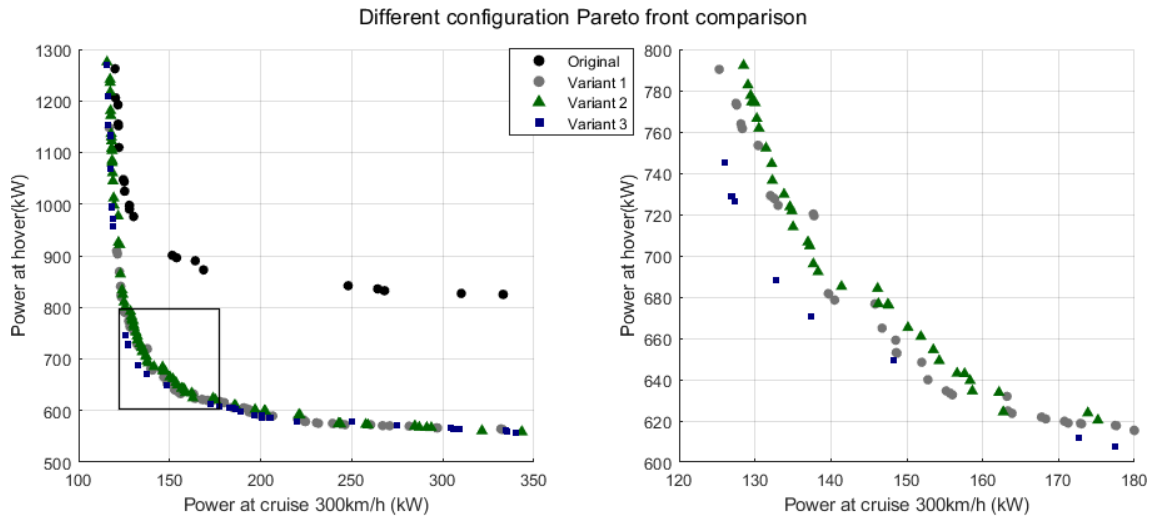


Figure 5.14: Pareto front for the original configuration and the different variants. Left, whole domain. Right, zoom in the black square.

Forward to backward propellers diameter ratio influences the optimum thrust distribution at hover, as observed in Figure 5.15. Variant 3 tends to around 63% provided by the back propeller for better cruise efficiency, and to approximately 54% provided by the back propeller for better hover efficiency. When forward propellers diameter is fixed to be 2m (Variant 1), optimum thrust distribution at hover tends to be around 56% of thrust by the back propeller for every point in the Pareto front. This is a cause of the limitations in the forward propellers longitudinal CG location. Also, by forcing the diameter to 2m and due to the lower bound on the blade chord value, limitations on applicable solidities may be present.

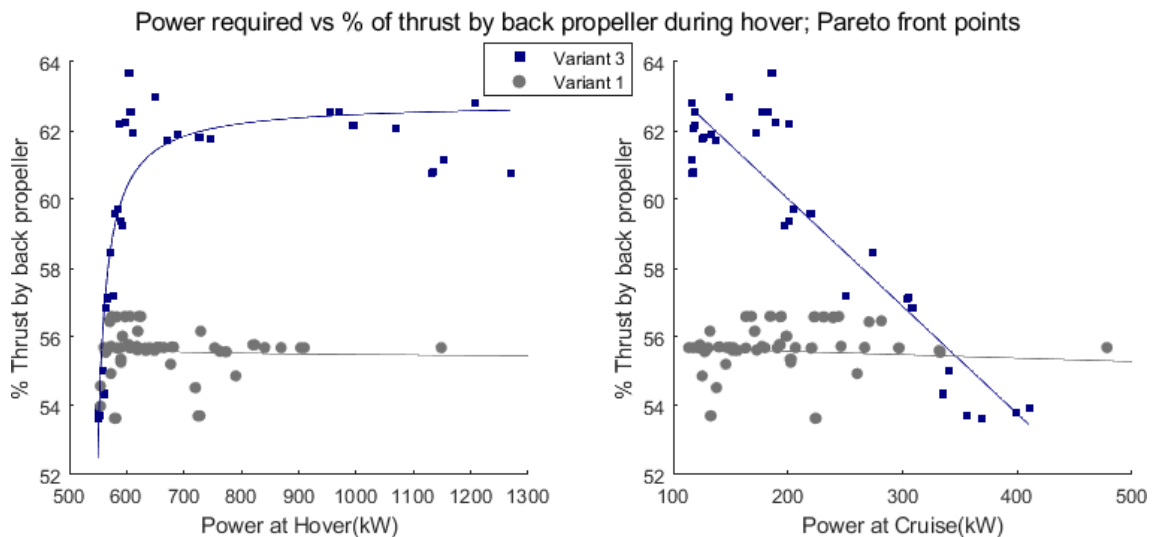


Figure 5.15: Percentage of thrust provided by the back propeller at hover as a function of Power at cruise at 300km/ for Variant 1 and Variant 3.

This section brings insight into more complex trade-offs between propeller diameter, cg location and thrust distribution. The first conclusion is the positive effect of diameter in performance at cruise and hover, especially for the second. Also, flexibility into propeller CG location leads to improvements in performance. For a better cruise performance, back propeller tends to provide a higher percentage of thrust at hover. For better hover performance, the percentage of thrust provided by the back propeller reduces, tending to more equal distribution during hover.

Another conclusion is the need to include propellers mass and mass distribution validation within the optimization. Increasing propeller diameter leads to higher rotor and structural mass. This should be included for proper evaluation of the trade-offs. Regarding mass distribution, propellers and powerplants suppose a relevant percentage of the mass of the aircraft. Greatly displacing them during the optimization could considerably affect CG estimation. A possible validation method to include this effect would be:

- Calculation of the optimum CG for a certain configuration within the optimization.
- Configuration analysed by mass distribution module, which generates upper and lower bounds on the possible CG values of the aircraft.
- Hard constrain with the following question, validity condition. Is the optimum CG inside the bounds?

5.4. Performance analysis

The trim analysis in Section 5.4.1 provides trimming information for every flight condition within the flight envelope. With the power requirements defined, a mission analysis is performed in Subsection 5.4.2 to assess the viability of the concept with current battery technology.

5.4.1. Trim analysis

Following the trimming methodology explained in 4.8.2, the minimum power point is obtained for each defined flight condition. Trimming point will be defined as a function of airspeed, altitude and propeller tilt angle. The curves presented in this section will show relevant information about the transition, which will be useful for defining the flight control for the whole flight envelope.

The flight envelope will be divided in two parts:

The 'Standard Cruise' region, where the airframe aerodynamics generate enough lift to maintain flight for $\alpha_b < 10deg$.

The ‘Stall’ region, which requires back propeller thrust to be able to fly. The speed that separates both curves is defined as the stall speed. Given the uncertainty on the accuracy of the back propeller results at high airspeeds, it will not be included for speeds over stall speed.

5.4.1.1. Performance for the ‘Standard Cruise’ region

First, the curve for speeds above stall speed without the back propeller influence will be studied. Performance curves in this phase are similar to the ones obtained for conventional aircraft, as defines linear lift and drag characteristics. However, the tilting propellers add nonlinear mechanics, producing slight variations in the curves that will be studied in this section.

As a counter-rotating propeller driven electric aircraft, power consumption is directly related to power required at each condition. Thus, maximum range and maximum endurance speeds will be given by minimum drag and minimum power speed respectively (N.Lawson,2019). According to the data presented in Figure 5.16, increasing altitude displaces both power and thrust curves to the right and upwards, with the increase in thrust being lower than the correspondent increase in power.

Therefore, optimum range and optimum endurance points will considerably vary depending on the altitude at where the aircraft is flying. Not only that, but also stall speed will vary due to the influence of density, placed at the denominator $TAS_{stall}^2 = \frac{2W}{\rho S_w C_{Lmax}}$. By increasing altitude, less aerodynamic forces are generated and therefore the aircraft decreases its minimum operational speed.

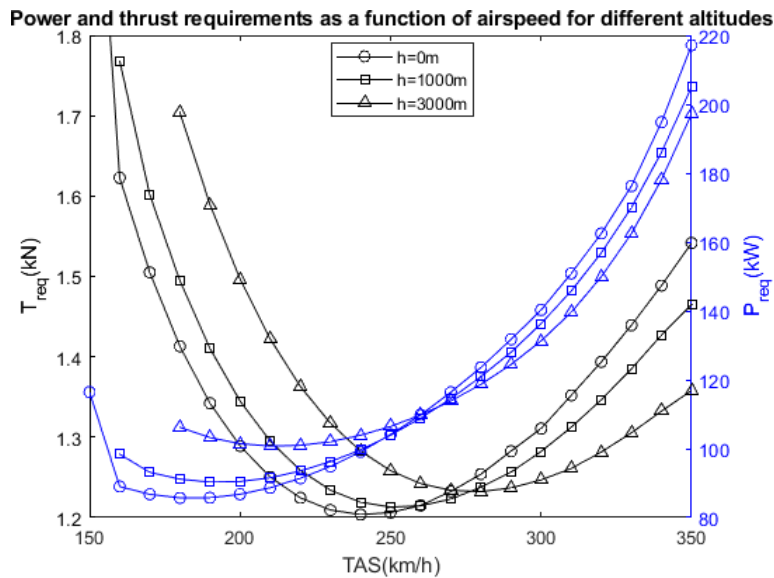


Figure 5.16: Power and thrust required as a function of airspeed and altitude for the D=2m optimized aircraft.

As observed in the full aircraft optimization results, most of the points in the Pareto front presented a propeller angle of attack of around 2.5deg, adding a small contribution to lift. Due to the ESDU correction, thoroughly explained in 4.2.3, when the propeller is in presence of an angle of attack, axial and normal forces are generated in the propeller axes as a consequence. Then, while a positive angle of attack contributes to lift generation, it also reduces the component of force on the wind X direction, requiring more thrust to compensate the same drag.

Additionally, there is the effect of the moment generated by the propeller. Normally, the elevator on the canard may be used to counter-act the moment generated by increasing the angle of attack ($C_{m\alpha} < 0$), but at the same time this would produce a drag increment. In parallel, when the propeller is tilted respect to the aircraft, thrust component in the normal direction to the aircraft has an effect similar to the canard. It generates a positive moment but thrust in the direction opposite to the drag is decreased.

Then, the viscous drag correction generates an additional positive moment. Canard viscous drag generates a more positive moment as the angle of attack increases. Wing and fuselage moments counter themselves for every angle of attack.

A balance between all the interactions just presented is found with the trimming algorithm, which defines the minimum power required at each flight condition. The trimming angles presented in Figure 5.17 show the trends for each of the inputs.

Angle of attack follows the expected trend, rising as the airspeed is reduced to increase lift coefficient. For higher altitudes, curves are displaced to the right due to the reduction in lift generation because to the lower density, which translates into higher stall speeds.

Meanwhile, both elevator and propeller angle of attack follow a similar trend until reaching lower speeds, where the elevator deflection is reduced while the propeller angle of attack and the airframe angle of attack rapidly increase. Lift and moment generation is divided evenly into propeller and elevator at higher speeds, with an approximate relation of $\frac{L_{prop}}{L_{elevator}} \sim 1$ at 300km/h; while at lower speeds the propeller increases its relative importance increasing $\frac{L_{prop}}{L_{elevator}}$ up to approximately 3 for 160km/h.

Due to the low variation in the elevator angle deflection for the whole curve, it is determined that the current elevator is oversized for the current needs (current size: 10-90% of the span and 70-100% of the chord).

Trimming angles as a function of airspeed for different altitudes

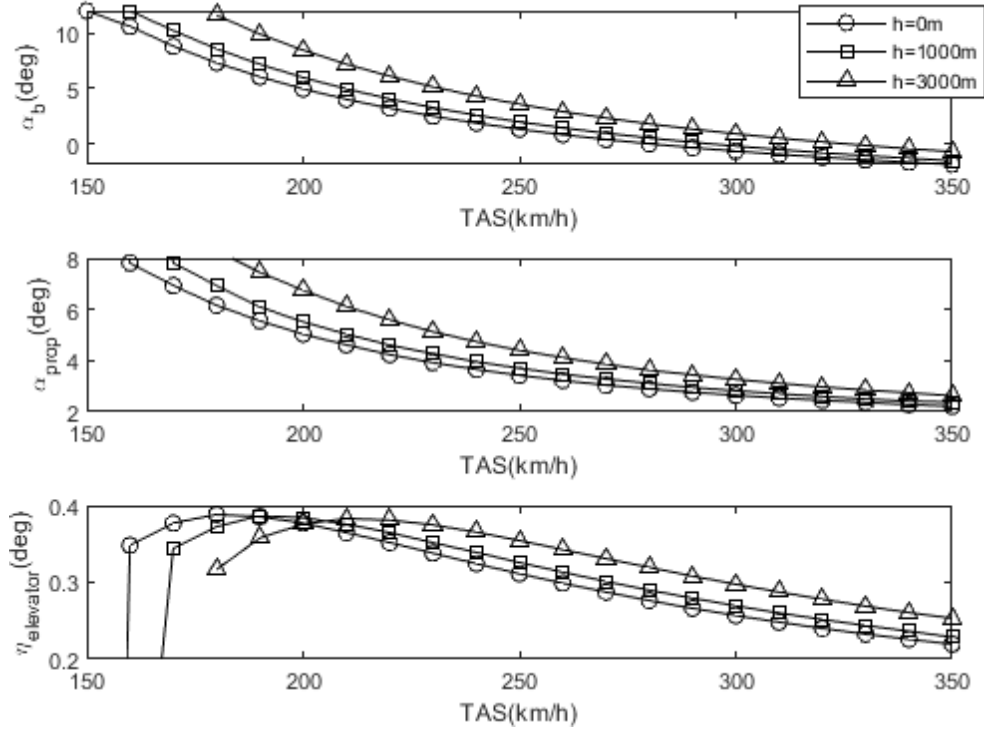


Figure 5.17: Trimming angles as a function of airspeed and altitude for the $D=2m$ optimized aircraft

5.4.1.2. Performance for the ‘Stall’ region

This section will present the ‘stall’ region of the curve. Again, methodology defined in 4.8.2 is followed to obtain the minimum power required at each condition. Nevertheless, flight condition will be defined by airspeed, altitude and tilt angle to provide a mapping for the transition regime.

Several considerations must be stated here regarding the limitations of the model. ESDU correction is only valid for propeller angles of attack of $\pm 20^\circ$, making it invalid for most of the transition region. Then, modelling accuracy for the back propeller is limited due to the lack of knowledge about the inflow conditions in that zone. The higher the speed, the more inaccuracy is expected.

For each propeller tilt angle, the power, angle of attack and thrust and power distributions are obtained and showed from Figure 5.18 to Figure 5.20.

ESDU correction can be applied down to 100km/h, the last point where trim can be maintained for a propeller angle of attack of $\pm 20^\circ$. It must be noted that propeller angle of attack is defined as $\alpha_{prop} = \alpha_b + \theta_{prop}$. Therefore, for lower speeds, induced angles due to ‘swirl’ or induced velocity may make this angle closer to 0deg.

From 150 to 90 km/h, flight can be maintained with tilt angles up to 60 without major rise in required power. Then, from 45 until 90km/h flying at the appropriate tilt angle becomes dominant due to the higher penalization for non-optimal angles. Finally, the slowest transition region, from 0 to 45, the differences reduce again.

Optimum power value slightly grows until reaching 30km/h and then drops rapidly as speed increases. This is explained in the following paragraphs:

In the transition region, there is a trade-off between the positive effect of aerodynamic lift and the negative effect on the forces generated by the back propeller. Assuming zero flight path angle, if angle of attack is increased, back propeller thrust will be inclined the same angle. This will not only reduce the lift generation by the back propeller $T_{Bprop} \cos(\alpha_b)$, but also will generate a component of drag $T_{Bprop} \sin(\alpha_b)$. As it can be seen in Figure 5.19, maximum airframe angle of attack is not maximum until reaching 60km/h. This is combined with the fact that, for constant thrust, power increases with airspeed ($P_{req} \approx TAS T_{req}$).

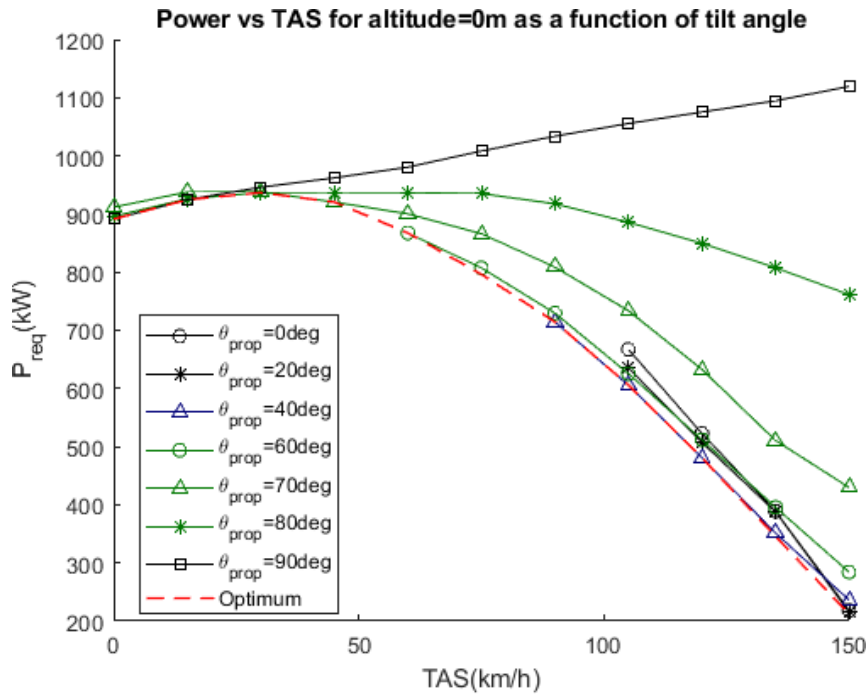


Figure 5.18: Power required as a function of airspeed and tilt angle for altitude=0m. Optimum(minimum) at each airspeed defined by red dashed line.

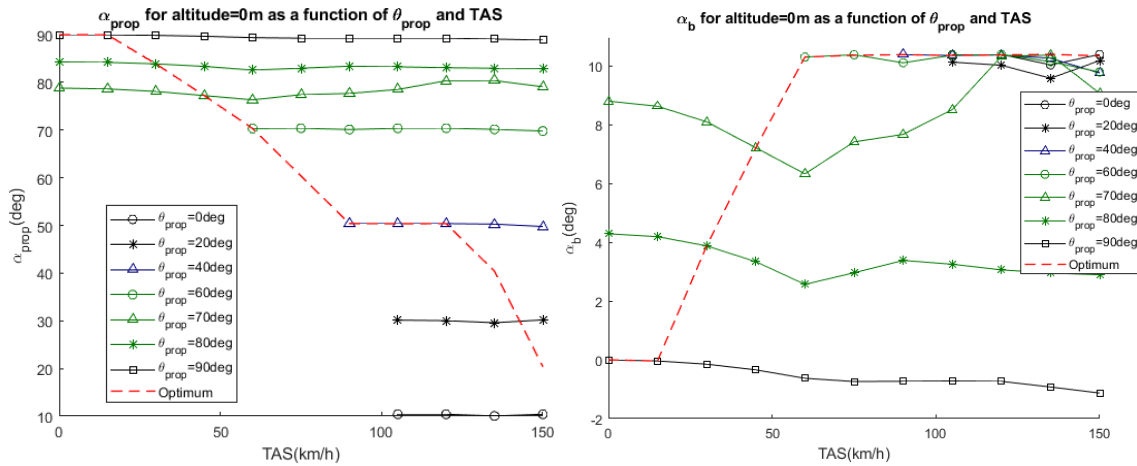


Figure 5.19: Propeller angle of attack(left) and Airframe angle of attack(right) as a function of airspeed and tilt angle for altitude=0m.

Optimum(minimum) at each airspeed defined by red dashed line.

Propeller angle of attack defined as the sum of airframe angle of attack and propeller tilt angle:

$$\alpha_{prop} = \alpha_b + \theta_{prop}$$

Regarding the thrust distribution, back propeller becomes dominant in thrust generation for speeds below 135km/h, highlighting its importance during transition. The problem with this is the increased power required by the back propeller during transition. Maximum power requirement for back propeller is not defined by hover but by transition. This will define the maximum power requirement for the electric motor and, therefore, its mass. A possible solution to limit the power at this condition is including it in the optimization, either as another flight condition or as a maximum power required constrain.

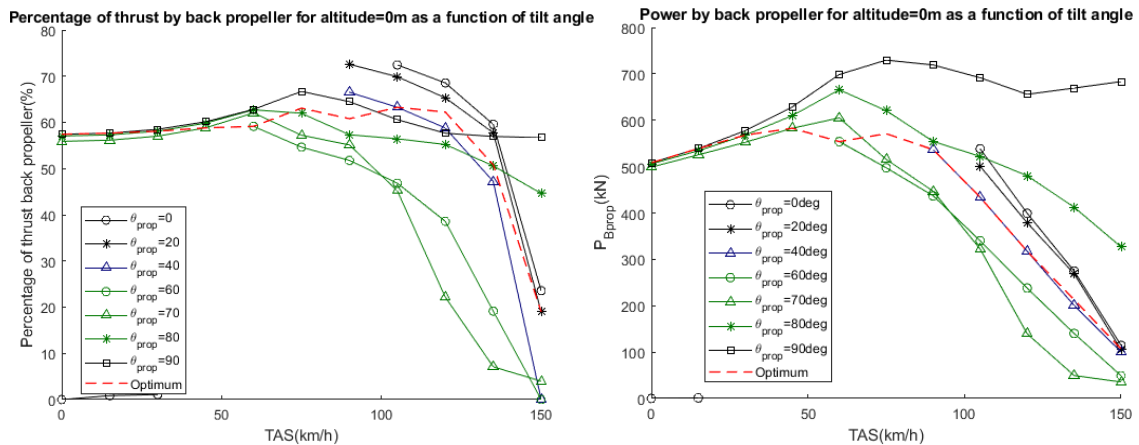


Figure 5.20: Percentage of thrust by the back propeller at hover(left) and power by the back propeller at hover(right) as a function of airspeed and tilt angle for altitude=0m.

Optimum(minimum) at each airspeed defined by red dashed line.

Maximum power requirement for the whole aircraft is found during transition, at around 30 km/h. For the back propeller, maximum power is found at speeds

around 45 km/h. Forward forward propellers provide maximum power during hover. Thus, power and size of the electric battery and motors must be selected accordingly. However, accuracy for the trimming results presented in this section cannot be guaranteed, as most of the transition occurs at conditions out of the scope of the model validity. Furthermore, this trimming is mathematical and has no validity without further stability analysis with the controller.

5.4.2. Battery performance

Battery performance will be evaluated for the mission defined in 4.9.1 for two configurations, the stated as 'Original' and 'Variant 1' from Section 5.3.4. Systems and other components efficiency losses described in 4.9.2 are accounted in the simulation. The evaluated Pareto front and the optimum points are presented in Figure 5.21.

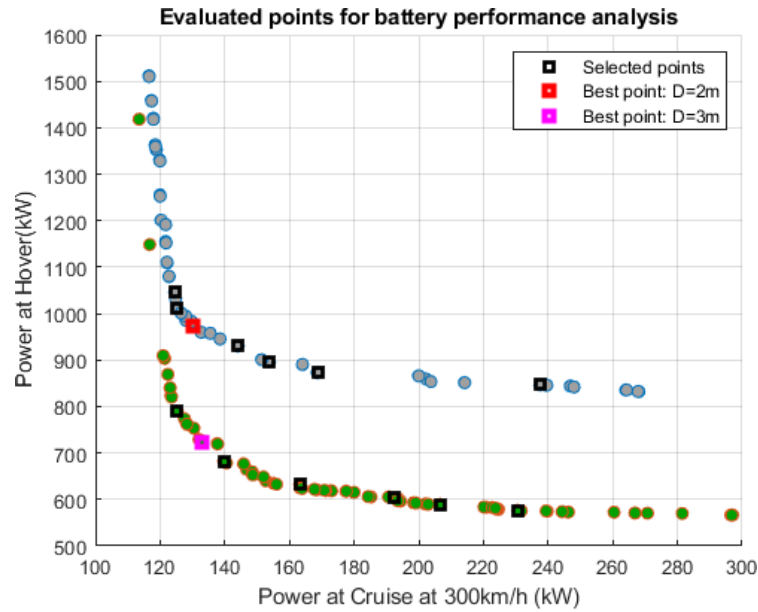


Figure 5.21: Pareto front and optimum mission points of 'Original' and 'Variant 1' configurations.

Original battery mass is 400kg for cells of a nominal voltage of 3.7V, a capacity of 3.015Ah and a cell mass of 48g (Hohm Tech, 2020). The equivalent battery mass to fulfill the mission by the original configuration is 1510kg, or an equivalent of 3.8 times the current energy density of the current cell. For the variant one, the required increment in specific energy to complete the mission would be considerably lower, around 3.1 times the current one. In the current battery pack modelling, capacity and power are obtained by multiplying the values of one cell

by the total number of cells. Therefore, an equivalent between mass or number of cells and power density can be established.

	Original	Variant 1
Required mass (kg)	1520	1278
Required increase in specific energy (multiplier of current one)	x3.8	x3.2

Table 5.9: Original and Variant 1 required mass and increase in specific energy to complete mission described in Section 4.9.1

The battery parameters evolution during the mission is presented in Figure 5.22, and the percentage of energy consumed at each flight phase in Table 5.10.

Transient effects cause that, when intensity values are too high, normally above 18A for each cell, discharge rate surges. This feeds-back into voltage, which rapidly reduces its value, further increasing current demand. Eventually, battery simulation is stopped when cell cut-off voltage or maximum intensity are reached. As seen, battery behavior changes considerably from low power to high power demand.

Limitation on battery size comes from the high power required during hover. This power demand forces a higher current value and discharge rate. This effect is further intensified at landing. Voltage of the system is lower when state of charge is low, requiring higher values of current that cause a surge in the discharge rate. This is showed in Table 10, where both second transition and landing present considerably increments in energy consumed when compared to first transition and take-off. Also, from the remaining SOC, it is determined that specific energy is not the limiting factor, but specific power is.

Percentage of SOC consumed (%)		
Phase	Original	Variant 1
Take-off	12.9	11.1
Transition	8.7	7.9
Cruise	43.4	50.1
Transition	9.3	8.4
Landing	15.8	14.1
Remaining SOC	9.9	8.3

Table 5.10: Percentage of SOC consumed at each flight phase and remaining SOC in the end.

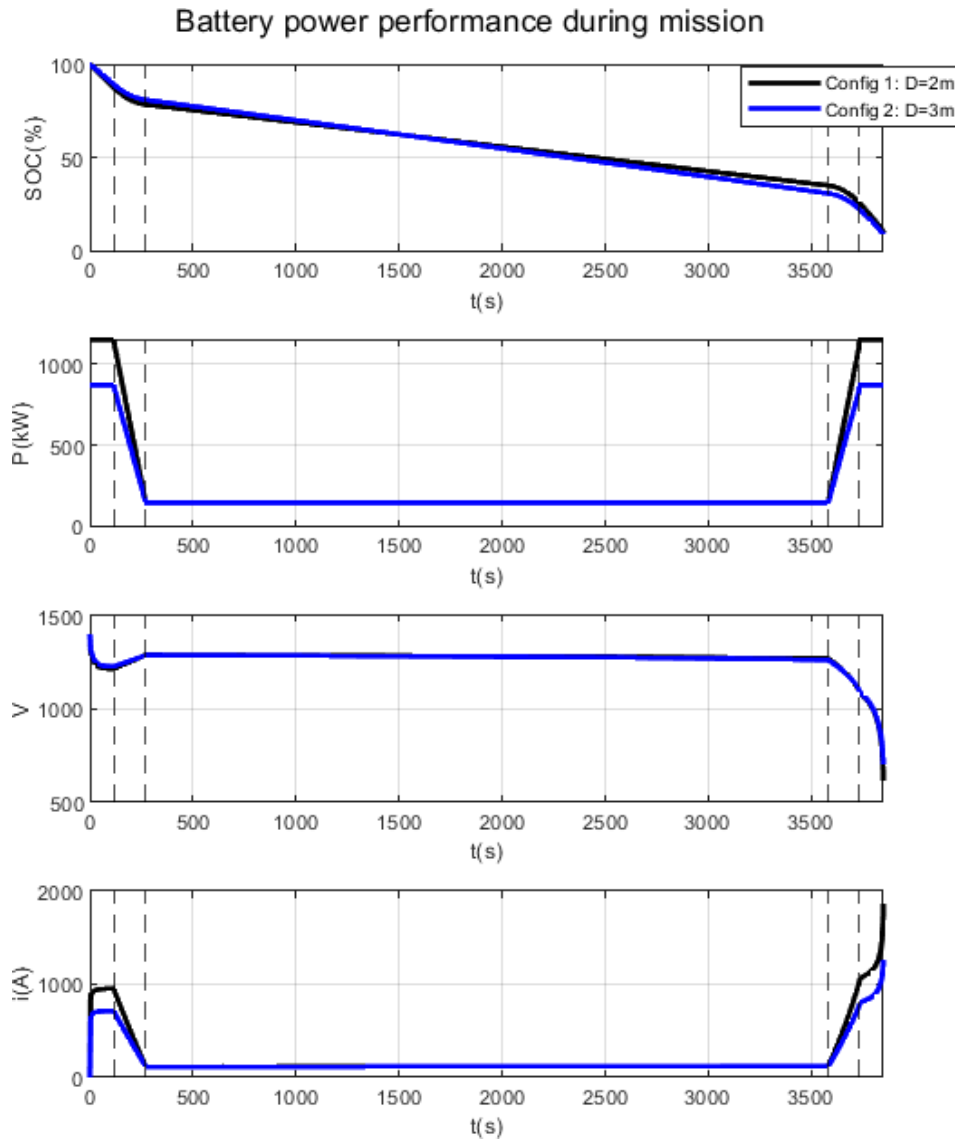


Figure 5.22: Battery parameters evolution during the mission described in Section 4.9.1. Config 1 is the original configuration while Config 2 represents Variant 1.

Being hover the limiting condition, a study is made to check the necessary power density or battery mass increase to take-off. This is presented in Figure 5.23, where hover time is studied as a function of the power density multiplier. It is seen that, with the current battery, at least 1.75 the current mass is needed just to take-off for variant 1, while the value is considerably higher for the original.

The results in section 5.4.2 showed the problem with high disk loading aircraft. As observed in the results, larger disk loading values will cause a surge in power demand during hover. As a result, batteries will need higher specific power in order to be able to even start flying.

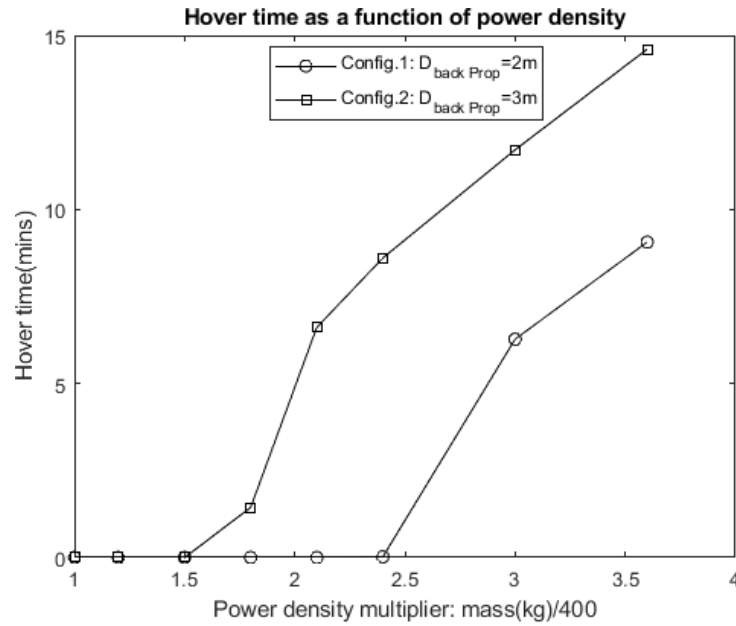


Figure 5.23: Hover time as a function of power density multiplier for the current mass. Config 1 is the original configuration while Config 2 represents Variant 1.

The battery performance analysis showed the impossibility to fulfill the mission with current battery technology. Moreover, aircraft is not even capable to take-off with the current battery mass. The problem, however, is not on energy density but on specific energy. According to Bacchini and Cestino(2019b), power can be significantly augmented using supercapacitors for the most power demanding flight phases. However, this would lead to a reduction in the energy density of the battery.

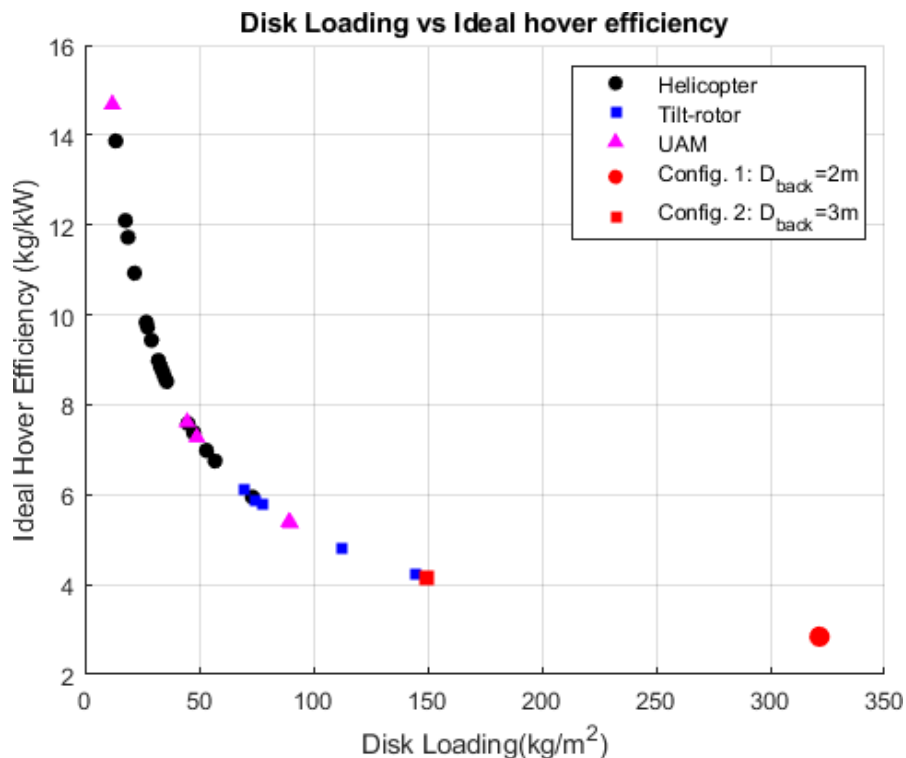
The main limitation of the cell model is the behavior at high power demand for each cell. The parameter identification for this model was performed using low power demand. Representation of the behavior for high power demand may be inaccurate, especially considering that thermal effects are not considered in this simulation.

5.5. Assessment against other aircraft

Getting to this point, most of the relevant parameters for aircraft performance have been identified. What is left to do is to compare where the 'final' configuration is compared to other configurations, both conventional canard and new urban air mobility configurations. For the UAM vehicles, only flight-tested designs have been included. Tables with the data used and the sources can be found in Appendix A.

First parameter to be evaluated will be disk loading, which defines ideal hover efficiency. Most of the aircraft capable of hovering beat this configuration on this parameter, as only the Lilium Jet presents a higher value of 765kg/m^2 . As it was proven in the previous section, reasonably low values for this parameter are needed in order to be able to maintain hover for a reasonable amount of time. This comes at the expense of a reduction in cruise performance.

First version with back and forward propellers diameters of 2m and 1.35m power loading caused hovering problems and caused problems with power supply during hover. Second version with larger propellers, maximum of 3m and 2m for the back and forward propellers respectively, allowed for a disk loading reduction down to a value of 150 kg/m^2 , similar to the Bell V-280 Valor.



Main aircraft aerodynamic parameters are presented as a function of MTOW for different canard aircraft in Figures 5.25 and 5.26. The main issue with this design is the limited span of 10m to adapt to heliports requirements. Observing the tendency in the figure, span for similar mass aircraft is expected to be around 2m longer. This limitation in span translates to further limitations on aspect ratio.

A lower aspect ratio involves higher stall speeds due to the reduction in lift coefficient slope. All of this leads to an increase in surface area if stall speed wants to be maintained. In the end, this feeds-back to the start, as the aspect ratio is further reduced due to the increment in wing surface. Also, lower aspect ratio implies higher induced drag. The quantitative results were presented in the sensibility analysis from Section 5.3.3

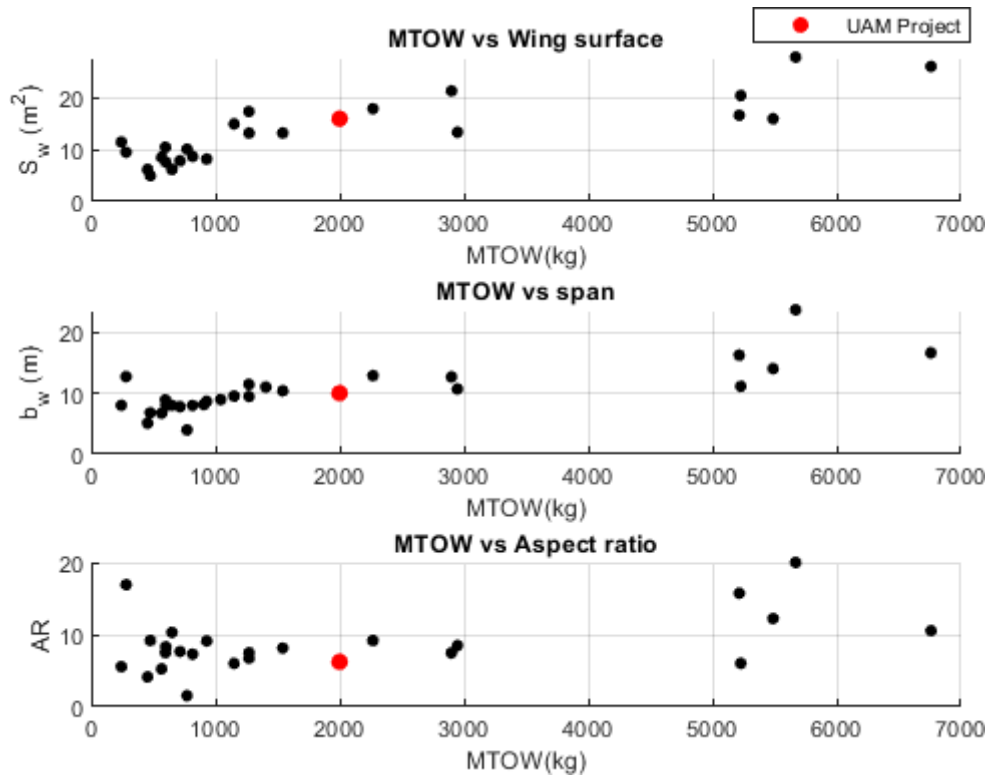


Figure 5.25: Wing surface, span and aspect ratio as a function of MTOW for different canard aircraft and current configuration.

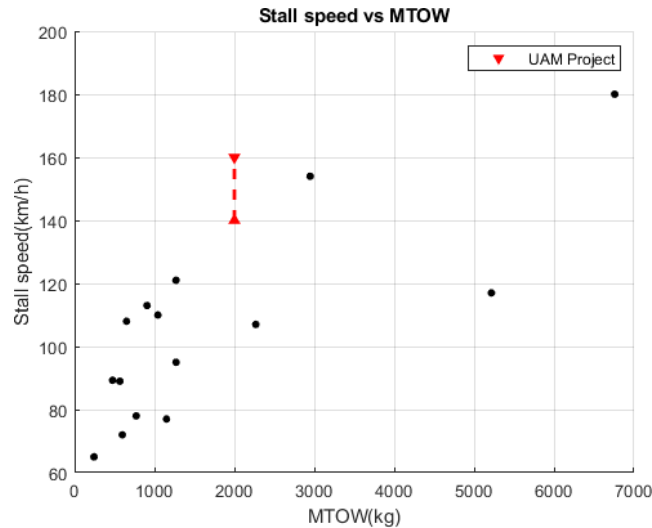


Figure 5.26: Stall speed as a function of MTOW for different canard aircraft and current project configuration.

Estimations from Bacchini and Cestino(2019a) yield battery mass to total mass ratios from 0.33 to 0.5 for other UAM projects. These numbers seem coherent with the results obtained in Section 5.4.2 and the considerable increase in energy density required to complete the mission. Also, passenger to total mass ratio for other UAM vehicles ranged from 0.25 to 0.4, while the current project's ratio is 0.15 (EHang, 2020) (Kitty Hawk, 2020) (Lilium Jet, 2020) (Airbus, 2019c). These comparisons can conclude that current mass may be overestimated.

Whereas passenger cruise efficiency values range from 14.5 to 20, fighters and VTOL jets are around 7-9. Helicopters present ever lower values, about 4-5 (Martinez, Ortega and Palacin, 2005) (Bacchini and Cestino, 2019b). Maximum $\frac{L}{D}$ value of 16 could be excessively optimistic comparing against this data, especially considering the restrictions in span and aspect ratio.

6. Conclusions

This section summarises the key findings, the conclusions and the future work regarding the objective of assessing the viability of the concept described in Section 2.

The growth in urban traffic congestion and pollution is demanding alternatives to conventional means of transportation. Electric Urban Air Mobility arises as one of the possible solutions for this problem. However, with current electric battery technology, specific power and energy suppose a considerable penalty into performance. Right now, the focus on this transportation as an alternative and the fast innovations on the field of electric powered aviation may accelerate the introduction of this type of vehicles into service.

6.1. Achievement of the objectives

Related to the objectives established in Section 2, conducting the undertaken research has led to the following results:

- A method for modelling and optimizing an EVTOL has been successfully developed. Modelling capabilities included airframe aerodynamics, propeller aerodynamics, inertia properties and electric batteries.
- An optimisation module allows to obtain a set of best configurations for different flight conditions and the associated trade-offs. An optimization scheme was developed to account for the large number of variables involved. Problem was decoupled in parts before optimizing the full aircraft. Genetic and direct search algorithms were combined to obtain optimum results. Response surface methodology led to considerable reduction in computational time.
- A performance analysis module has been developed. Viability of the model powered by Li-ion battery has been assessed with this module. Trimming conditions and power required have been obtained for multiple flight conditions. Capability for mission analysis has been include.
- A study of the key design parameters has been performed along with comparison against other aircraft and UAM projects.
- Simulink model has been developed and provided to the flight control design team.

6.2. Key findings

This configuration allows for a degree of uncoupling for hover and cruise. While the back propeller is optimized for hover, forward propellers can be optimized for cruise. Furthermore, thrust distribution during hover can be altered so that the back propeller provides a higher percentage of total thrust. This can reduce the negative impact of inefficient forward propellers at hover. Optimum thrust distribution during hover for the mission was found to be around 62% of the thrust provided by the back propeller and 38% by the forward propellers. Increasing the propeller diameter also provides a drastic increase in hover efficiency. However, the limitations arise in the size of the aircraft and the distances between the aircraft centre of gravity and the propellers. Also, safety and fail scenarios could impose constraints on this.

Operability may be limited in case of propeller fail. Reduction in stall speed can increase the operability envelope of the aircraft. However, cruise drag is increased for a reduction in stall speed.

The combination of response surface and an optimization scheme with pre-seeding and different algorithms proved to be necessary to obtain optimum results in reasonable time.

Model is not viable with current power density and battery technology. To be able to complete the specified mission, energy density must be increased by 3.1 times the current one. Hover proved to be the limiting phase due to its high-power demand. To be able to take off, energy density must be increased by 1.7 times the current one. However, the limitation was not on energy density but on specific energy. Supercapacitors could help to solve this problem. Accuracy of the model at high power demands can be limited.

Performance analysis showed that maximum power condition is found during transition. Therefore, electric motors and batteries should be sized accordingly.

After comparison with other UAM projects, it was determined that current battery mass to total mass ratio is too low and must be increased. Furthermore, total mass seems to be overpredicted by comparison to other UAM projects battery mass to total mass and passenger mass to total mass ratios. Mass reduction would lead to considerable improvements in performance. Performance can also be enhanced by relaxing constraints on wingspan.

Model limitations lead to reduction in accuracy and inapplicability in certain regions of the flight envelope. Airframe geometry is simplified, with the wing and the fuselage being disconnected. Fuselage is modelled as an airfoil. Aerodynamic modelling tool is only applicable for the linear region of the lift coefficient curve. Drag estimates are obtained with empirical estimations. Canard and airfoil camber have no effect in induced drag generation, which may lead to inaccurate results. Propeller angle of attack correction is only applicable for $\pm 20^\circ$. Back propeller autorotating effects are not included in forward flight.

6.3. Future work

Due to limited time, some design aspects could not be assessed, especially the ones related to safety and fail cases. Furthermore, modelling showed flaws in some aspects and should be improved for more accurate predictions. Recommendations are divided into design changes and model improvement.

Recommendation to improve design:

- Evaluation the consequences of relaxation of the constraints on span, propeller diameter and thrust distribution at hover.
- Mass distribution could be optimized to reduce total mass and make design comparable to other UAM projects.
- Supercapacitors could be included to enhance hover performance by producing high specific power at this flight condition. However, this would cause a trade-off as specific energy would be reduced. Hybrid power system with fuel cells could be another alternative.
- A second blade pitch angle possible on the forward propeller would considerably increase hover efficiency, decrease noise and suppress possible stall. This would come at the expense of increased price, higher complexity and lower reliability.
- Ducted fans can provide higher levels of thrust and noise reduction.

Recommendations for enhancing the model accuracy:

- Inclusion of structural models and requirements in propeller and airframe design.
- Introduction of viscous effects modelling capabilities into the aerodynamic model are necessary for increased accuracy. Software like XFLR5 or VSAERO could be an alternative modelling software.
- Accurate aerodynamic prediction would require the inclusion of the complete aircraft. Therefore, back wing could be attached to the fuselage by a leading-edge extension or a similar structure.
- Enhance battery model by including temperature effects to improve accuracy for high power demands.
- QPROP results proved to be conflictive at low J for the forward propellers. A capability that includes separation modelling into propeller analysis may be essential for accurate estimations at low J . A modelling tool or correction is needed for accurate estimation for propellers angles of attack over 20deg. Furthermore, counterrotating propellers cannot be accurately modelled with QPROP. CROTOR could be a viable choice for counterrotating propeller modelling. Back propeller model should be further enhanced to account for windmilling effects during cruise.
- Modelling of propeller-airframe interaction effects, e.g. forward propellers slipstream.

- Noise levels normative is strict in urban areas and, thus, noise modelling is necessary for viability analysis. Noise modelling with XROTOR or NAFnoise could be an alternative.
- Introduction of a mass sizing module that accounts for wing, canard and propellers size in mass estimation. In line with this, a mass distribution capability should be included to validate centre of gravity values.

Bibliography

Airbus(2020b) E-Fan X: A giant leap towards zero-emission flight. Available at: https://www.airbus.com/innovation/zero-emission/electric-flight/e-fan-x.html?fbclid=IwAR1OLK_JssFNoZWR8nkg73fudmUR6E7angXUdGLo9FV_Dy-W3sKiXFjIZ5g

Airbus(2020b) CityAirbus: Our four-seat EVTOL demonstrator. Available at: <https://www.airbus.com/innovation/zero-emission/urban-air-mobility/cityairbus.html>

Airbus(2020c) Vahana: Our single-seat EVTOL demonstrator. Available at: <https://www.airbus.com/innovation/zero-emission/urban-air-mobility/vahana.html>

Anderson, J. D. (2001). Fundamentals of aerodynamics. Mcgraw Hill Series in Aeronautical and Aerospace Engineering. ISBN: 0073398101.

AOPA (2020) Cessna 172 Aircraft Fact Sheet. Available at: <https://www.aopa.org/go-fly/aircraft-and-ownership/aircraft-fact-sheets/cessna-172>.

Aston Martin (2020) The Aston Martin Volante vision concept. Available at: <https://www.astonmartin.com/en-us/models/future-models/the-aston-martin-volante-vision-concept-usa>.

Bacchini, Alessandro & Cestino, E. (2019a). Electric VTOL Configurations Comparison. Department of Mechanical and Aerospace Engineering, Politecnico di Torino. DOI: 10.3390/aerospace6030026.

Bacchini, Alessandro & Cestino, E. (2019b). Key aspects of electric vertical take-off and landing conceptual design. Journal of Aerospace Engineering. Volume: 234 issue: 3, pages: 774-787. Available at: <https://doi.org/10.1177/0954410019884174>.

Brizzolara, Stefano & Grassi, Davide & Tincani, Emilio. (2012). Design Method for Contra-Rotating Propellers for High-Speed Crafts: Revising the Original Lerbs Theory in a Modern Perspective. International Journal of Rotating Machinery. 408135. 10.1155/2012/408135.

Boeing (2020) V-22 Osprey Technical Specifications. Available at: <https://www.boeing.com/defense/v-22-osprey/>

Borst, H. (1973) Summary of Propeller Design Procedures and Data. Volume I. Aerodynamic Design and Instalation. Army Air Mobility Research and Development Laboratory. Available at: AD-774 851.

Camberos, J., Kolonay, R., Eastep, F. and Taylor R. (2014). Zero-Lift Drag Prediction Including Aeroelastic Effects. 55th AIAA/ASME/ASCE/AHS/ASC Structures, Structural Dynamics, and Materials Conference. Available at: <https://doi.org/10.2514/6.2014-1194>.

- Cook, M.(2012) Flight Dynamic Principles: A Linear Systems Approach to Aircraft Stability and Control 3rd Edition. Butterworth-Heinemann. ISBN: 9780080982427
- Cooke, A. (2013) Data Pack for the Jetstream 31. Part of the Flight Dynamic Principles Assignment, MSc in Aerospace Dynamics, Cranfield University.
- Cooke, A.(2019) J31 (G-NFLA) 'Flight Test Report' [Lecture] Flight Experimental Methods. Cranfield University. October.
- Dantsker, O. & Vahora, M. (2018) Comparison of Aerodynamic Characterization Methods for Design of Unmanned Aerial Vehicles. 10.2514/6.2018-0272.
- De Leeuw, T. (2013) Investigation on the influence of scaling effects in propeller testing through the use of theoretical prediction codes. MSc Thesis. TU Delft.
- Deb, K. (2011) Multi-Objective Optimization Using Evolutionary Algorithms: An Introduction. Department of Mechanical Engineering Indian Institute of Technology Kanpur.
- Dever, T.P.; Duffy, K.P.; Provenza, A.J.; Loyselle, P.L.; Choi, B.B.; Morrison, C.R.; and Lowe, A.M.(2015). TP-2015-216588: Assessment of Technologies for Noncryogenic Hybrid Electric Propulsion. NASA.
- Dimchev, M. (2012) Experimental and numerical study on wingtip mounted propellers for low aspect ratio UAV design. Msc thesis. TU Delft.
- Drela, M. (2005) Propeller Characterization for QPROP. Available at: http://web.mit.edu/drela/Public/web/qprop/prop_measure.pdf
- Drela, M. (2006) QPROP Formulation. Available at: http://web.mit.edu/drela/Public/web/qprop/qprop_theory.pdf
- Drela, M. (2007) QPROP User Guide. Available at: http://web.mit.edu/drela/Public/web/qprop/qprop_doc.txt
- Drela, M., Youngren, H. (2017). AVL 3.36 User Guide. Available at: http://web.mit.edu/drela/Public/web/avl/avl_doc.txt.
- EHang (2020) EHang website. Available at: <https://www.ehang.com/ehangaav>
- Emrax (2020). Emrax model 348CC technical specifications. Available at: <https://emrax.com/e-motors/emrax-348/>
- ESDU (2006). ESDU 89047: In-plane forces and moments on installed inclined propellers at low forwardspeeds. ESDU International. With Amendments A to C, August.
- ESOTEC (2011) CROTOR: XROTOR on Steroids. Esoteric Technology Developments. Available at: <http://www.esotec.org/sw/crotor.html>
- European Environment Agency (2019) CO2 emissions from passenger transport. Available at: <https://www.eea.europa.eu/media/infographics/co2-emissions-from-passenger-transport/view>

Finger, F., Braun, C., Bil, C. (2017) A Review of Configuration Design for Distributed Propulsion Transitioning VTOL Aircraft. Conference: Asia-Pacific International Symposium on Aerospace Technology 2017, APISAT2017

Garcia, D. (2009). Robust smoothing of gridded data in one and higher dimensions with missing values. Computational Statistics & Data Analysis, Volume 54, Issue 4 Pages 1167-1178, ISSN 0167-9473. Available at: <https://doi.org/10.1016/j.csda.2009.09.020>.

Gudmundsson, S. (2013). General Aviation Aircraft Design: Applied Methods and Procedures. General Aviation Aircraft Design: Applied Methods and Procedures. 1-1034.

Gur, O., Rosen, A. (2009) Optimization of Propeller Based Propulsion System. Technion, Israel Institute of Technology. Available at: 10.2514/1.36055

Heffley, R., Jewell, W. (1972) CR-2144: Aircraft handling qualities data. Systems Technology, Inc. NASA. Available at: AD-A277031.

Herráez, Iván & Akay, Buşra & van Bussel, Gerard & Peinke, Joachim & Stoevesandt, Bernhard. (2016) Detailed analysis of the blade root flow of a horizontal axis wind turbine. Wind Energy Science. 1. 89-100. 10.5194/wes-1-89-2016.

Hepperle, Martin. (2012) Electric Flight - Potential and Limitations. Institute of Aerodynamics and Flow Technology, German Aerospace Center.

Hohm Tech (2020). Hohm Life 4 Specification datasheet. Available at: <https://hohmtech.com/product/h%CF%89-life-hohm-life-inr-18650-3-7v-li-comnni-3077mah-36-3a-high-drain-rechargeable-li-ion-battery-ft-2-pack/>.

Hubbard, H. (1991) Aeroacoustics of Flight Vehicles: Theory and Practice. Volume 1: Noise Sources. NASA Langley Research Center. Available at: 19920001380.

INRIX (2019a) INRIX 2019 Global Traffic Scorecard. Available at: <https://inrix.com/scorecard/>.

INRIX (2019b) INRIX Global Traffic Scorecard: Congestion cost UK economy £6.9 billion in 2019. Available at: <https://inrix.com/press-releases/2019-traffic-scorecard-uk/>.

Integral Powertrain (2020) High Torque SPM Motors Generator Units. Available at: <https://integralp.com/downloads/high-torque-spm-motors-generator-units/>.

Jobe, C. (1984) AFWAL-TM-84-203: Prediction of aerodynamic drag. Air Force Wright Aeronautical Laboratories, Flight Dynamics Laboratory.

Johnson, W. (2010) NDARC-NASA Design and Analysis of Rotorcraft Theoretical Basis and Architecture. NASA Ames Research Center. Available at: 20100021986.

- Johnson, W. (2013) Rotorcraft Aeromechanics (Cambridge Aerospace Series). Cambridge: Cambridge University Press. doi:10.1017/CBO9781139235655
- Keane, A., Nair, P. (2005) Computational Approaches for Aerospace Design: The Pursuit of Excellence. ISBN: 978-0-470-85540-9
- Kisielowski, E., McVeigh, M. (1971) NASA-CR-1646: A design summary of stall characteristics of straight wing aircraft. Dynasciences Corp. Blue Bell.
- Kitty Hawk (2020) Kitty Hawk website. Available at: <https://kittyhawk.aero/>
- Khairy, A., Venneri, S. (1997) Future Aeronautical and Space Systems. Profress in Astronautics and Aeronautics: Volume 172.
- Lanham, C. (1979) ASD-TR-79-5004. Inertia Calculation Procedure for Preliminary Design. Aeronautical Systems Division, Wright-Patterson Air Force Base.
- Lawson, N. (2019) 'Fundamentals of Aircraft Performance' [Lecture] Introduction to Aircraft Aerodynamics. Cranfield University. October.
- Leishman, J. (2006) Principles of Helicopter Aerodynamics. 2nd edition. Cambridge Aerospace Series. ISBN: 0521858607
- Lilium Jet (2020) Lilium Jet webpage. Available at: <https://lilium.com/>
- Liu, G., Yang, J., Whidborne, J. (2006) Multiobjective optimisation and control. Series: Engineering Systems Modelling and Control. European Journal of Operational Research. Available at: 174. 668–671. 10.1016/j.ejor.2005.04.003.
- Lone, M. (2020) 'Aircraft System Identification II' [Lectures] Aircraft System Identification. Cranfield University. March.
- Long, P. (1985) TP-2382: Wind-Tunnel Investigation of a Full-Scale Canard-Configured General Aviation Airplane. NASA.
- MathWorks (2020a) Choose a Multilayer Neural Network Training Function. Available at: <https://uk.mathworks.com/help/deeplearning/ug/choose-a-multilayer-neural-network-training-function.html>
- MathWorks (2020b) griddatan, interpolate N-D scattered data. Available at: <https://uk.mathworks.com/help/matlab/ref/griddatan.html>
- MathWorks (2020c) nlinfit, Nonlinear regression. Available at: <https://uk.mathworks.com/help/stats/nlinfit.html>
- MathWorks (2020d) paretosearch Algorithm. Available at: <https://uk.mathworks.com/help/gads/paretosearch-algorithm.html>
- Mathworks(2020e) When to use a Hybrid Function. Available at: <https://uk.mathworks.com/help/gads/when-to-use-hybrid-function.html>.

Maisel, M., Giulianetti, D., Dugan, D. (2000) The History of the XV-15 Tilt Rotor Research Aircraft: From Concept to Flight. NASA, Washington D.C. Available at: 20000027499.

Martinez-Val, R., Perez, E., Palacín, J. (2005) Historical evolution of air transport productivity and efficiency. Universidad Politécnica de Madrid.

McVeigh, A., Kisielowski, E. (1971) CR-1646: A design summary of stall characteristics of straight wing aircraft. Dynasciences corporation, scientific systems division, NASA.

Mikkelsen, D., Mitchell, G., Bober, L. (1984) Summary of Recent NASA Propeller Research. NASA Technical Memorandum 83733. Available at: N84-32334.

Molter, C., Cheng, P. (2017) Propeller Performance Calculation for Multicopter Aircraft at Forward Flight Conditions and Validation with Wind Tunnel Measurements. University of Stuttgart, Wind Energy Research Group (SWE) at the Institute of Aircraft Design.

Mutluay, T. (2015) The development of an inertia estimation method to support handling quality assessment. MSc thesis, TU Delft.

NASA (2018) Urban Air Mobility Market Study. Available at: <https://www.nasa.gov/sites/default/files/atoms/files/uam-market-study-executive-summary-v2.pdf>

Nigam, N., Tyagi, A., Chen, P., Alonso, J., Palacios, F., Ol, M., Byrne, J. (2015) Multi-Disciplinary Propeller/Rotor Analysis and Design. Conference: 53rd AIAA Aerospace Sciences Meeting. Available at: 10.2514/6.2015-0029

Peerlings, B. (2018) A review of aerodynamic flow models, solution methods and solvers – and their applicability to aircraft conceptual design. Literature study report. MSc thesis, TU Delft.

Raymer, D. (1992) Aircraft Design: A Conceptual Approach, 2nd Edition. American Institute of Aeronautics and Astronautics, AIAA Education Series. ISBN: 0-930403-51-7.

Our World in Data (2018) Urbanization. Available at: <https://ourworldindata.org/urbanization>

Our World in Data (2019) World Population Growth. Available at: <https://ourworldindata.org/world-population-growth#:~:text=The%20visualization%20shows%20how%20strongly,middle%20of%20the%2016th%20century.>

Robinson Helicopters Company (2020) R44 Raven II Technical Specifications. Available at: <https://robinsonheli.com/r44-specifications/> (Accessed 8 August 2020).

Royal Australian Navy (2020). Agusta A109E performance specifications. Available at: <https://www.navy.gov.au/aircraft/agusta-a109e-power> (Accessed 8 August 2020).

Siddappaji, K., Turner, M. (2015) Counter rotating propeller design using blade element momentum theory. University of Cincinnati, School of Aerospace Systems.

Scholz, N. (2012) Estimating the Oswald Factor from Basic Aircraft Geometrical Parametres. Hamburg University of Applied Sciences. Available at: https://www.fzt.haw-hamburg.de/pers/Scholz/OPerA/OPerA_PUB_DLRK_12-09-10.pdf.

Snyder, C. (2019) Personal Rotorcraft Design and Performance with Electric Hybridization. NASA Glenn Research Center Cleveland OH. Available at: 20170005655.

Thiele, M., Obster, M., Hornung, M. (2019) Aerodynamic Modeling of Coaxial Counter-Rotating UAV Propellers. Institute of Aircraft Design, Technical University of Munich

Torenbeek, E. (1982) Synthesis of subsonic airplane design. Delft University Press. ISBN: 90-247-2724-3.

Tornado (2020) Tornado: A Vortex Lattice Method implemented in MATLAB. Available at: <https://tornado.redhammer.se/index.php/theory>.

United Nations (2018) The World's Cities in 2016: https://www.un.org/en/development/desa/population/publications/pdf/urbanization/the_worlds_cities_in_2016_data_booklet.pdf

United Nations (2018) World Urbanization Prospects 2018. Available at: <https://population.un.org/wup/>

Valdes, G., Navarro, F., Harrison, K., Merrington, R., Mabel, S., Prasad, S. (2019) Flight experimental methods group test report. Part of Flight Experimental methods course in Cranfield University.

Vertical Flight Society (2020) eVTOL Classifications. Available at <https://evtol.news/classifications>.

Vratny, P., Gologan, C., Pornet, C., Isikveren, A., Hornung, M. (2013) Battery Pack Modeling Methods for Universally-Electric Aircraft.

Wisniewski, C., Byerley, A., Heiser, W., Van Treuren, K., Liller, K. (2015) Designing Small Propellers for Optimum Efficiency and Low Noise Footprint. 33rd AIAA Applied Aerodynamics Conference. Available at: 10.2514/6.2015-2267.

Yip, L. (1985) NASA-TP-2382: Wind-Tunnel Investigation of a Full-Scale Canard-Configured General Aviation Airplane. NASA Langley Research Center. Available at: 19850011615

Appendix A

Canard aircraft data

	MTOW (kg)	OEW (kg)	Span (m)	Wing Area(m2)	Cruise speed (km/h)	Max. Speed (km/h)	Stall speed (km/h)	Source
Velocity XL	1270	816	9.45	13.23	380	370	121	1
Velocity SE	1043	590	8.94		346		110	2
Velocity Vtwin	1542	907	10.39	13.24	370			3
Rutan Long EZ	601	322	7.96	7.617	232	298		4
Rutan VariEze	476	263	6.77	4.98	266	314	89.3	5
Mikoyan-Gurevich MiG-8	1150	642	9.5	15		205	77	6
Berkut 360	907	469	8.13		354	298	113	7
Cozy MK IV	930	476	8.655	8.2	350			8
AASI Jetcruzer	2268	1352	12.85	17.95	570	590	107	9
Beechcraft Starship	6759	4574	16.6	26.1	568	620	180	10
e-Go Aeroplanes e-Go	243	115	8	11.5		222	65	11
Piaggio P.180 Avanti	5488	3799	14	16	589	740	190	12
Peterson Kenai	1406	587	11					13
Rutan Solitaire	281	172	12.7	9.517				14
OMAC Laser 300	2900	1700	12.65	21.4	467			15
Avtek 400A	2948	1714	10.67	13.4	550		154	16
Gyroflug Speed Canard	715	440	7.77	7.87				17
Viking Dragonfly	567	272	6.71	8.56	210	290	89	18
Scaled Composites Model 133-4.62								
ATTT	5216		16.21	16.67		310	117	19
Scaled Composites Proteus	5670	2658	23.65	27.92	352	313		20
Dickey E-Racer Mark 1	816	499	7.986	8.733	362	400		21
QAC Quickie Q2	454	222	5.08	6.22	225	290		22

Miles M.39B Libellula	1270	1091	11.43	17.42	164		95	23
Lockspeiser LDA-01	771	561	3.96	10.11	170		78	24
Kyushu J7W	5228	4928	11.114	20.5	422	750		25
Ion Aircraft Ion 100	598	403	8.89	10.5	251		72	26
Aceair AERIKS 200	650	400	8	6.2	259	370	108	27

Sources list:

Source number

- 1 <http://www.velocityaircraft.com/aircraft>
- 2 <http://www.velocityaircraft.com/aircraft>
- 3 <http://www.velocityaircraft.com/aircraft>
- 4 Jane's All The World's Aircraft 1982–83. Taylor 1982, pp. 564–565.
- 5 Jane's All The World's Aircraft 1982–83. Taylor 1982, pp. 564–565.
- 6 Gunston, Bill (1995). *The Osprey Encyclopedia of Russian Aircraft 1875–1995*. London: Osprey. p. 184. ISBN 1-85532-405-9.
- 7 Taylor, Michael J. H., ed. (1999). *Brassey's world aircraft and systems directory 1999-2000* (2nd ed.). London: Brassey's Inc. p. 583. ISBN 1-85753-245-7.
- 8 cozyaircraft.com
- 9 Brassey's World Aircraft & Systems Directory 1996/97
- 10 Beech Starship 1 (model 2000) FAA Approved Airplane Flight Manual" (PDF). bobscherer.com. September 1998. Retrieved August 3, 2017.
- 11 Bayerl, Robby; Martin Berkemeier; et al: *World Directory of Leisure Aviation 2011-12*, page 42. WDLA UK, Lancaster UK, 2011. ISSN 1368-485X
- 12 Taylor, John W. R. (1988). Lambert, Mark, ed. *Jane's All The World's Aircraft 1988-89* (en inglés) (79 edición). Coulsdon, Reino Unido: Jane's Information Group. p. 800. ISBN 0-7106-0867-5.
- 13 <https://www.katmai-kenai.com/aircraft/kenai.php>
- 14 <https://web.archive.org/web/20110715225311/http://www.sailplanedirectory.com/PlaneDetails.cfm?PlaneID=330>
- 15 *Jane's All the World's Aircraft 1987–88* p.480
- 16 *John W.R. Taylor, ed. (1988). Jane's All the World's Aircraft 1988-89. London: Jane's Information Group. ISBN 0-7106-0867-5.*

- 17 Jane's All The World's Aircraft 1992–93, Lambert 1992, pp. 79–80.
- 18 Jackson 2003, pp. 734–735.
- 19 Jane's All the World's Aircraft 2003–2004
- 20 Jane's All the World's Aircraft 2003–2004
- 21 Purdy, Don: *AeroCrafter - Homebuilt Aircraft Sourcebook, Fifth Edition*, page 146. BAI Communications, 15 July 1998. ISBN 0-9636409-4-1
- 22 "What are the specifications for a Q2?". *Quickie Builders Association*. Archived from the original on 2005-12-17. Retrieved 2006-04-14.
- 23 Miles aircraft since 1925, Brown (1970) p236-242
- 24 Jane's All The World's Aircraft 1976–77
- 25 Francillon, Rene (1979). *Japanese Aircraft of the Pacific War*. London: Putnam & Company Limited. ISBN 0 370 30251 6
- 26 Jackson, Paul (2011). *Jane's All the World's Aircraft 2012-13*. Coulsdon, Surrey: IHS Global. p. 842. ISBN 978-0-7106-3000-1.
- 27 Jackson, Paul. *Jane's All The World's Aircraft 2003–2004*. Coulsdon, UK: Jane's Information Group, 2003. ISBN 0-7106-2537-5.

Rotorcraft and Tilt-rotor Data

Data extracted from Leishman(2006).

ROTORCRAFT	Mass (kg)	Rotor radius,m	Number of rotors	Disk area, m2	Disk loading Nm-2	Ideal power(W)	Hover efficiency
AS 332 Puma	8600	7.79	1	190.64	45.1	1133864	7.6
SA365	4000	5.97	1	111.78	35.8	469708	8.5
AS350B	1950	5.34	1	89.75	21.7	178425	10.9
Augusta A103	2605	5.5	1	95.03	27.4	267733	9.7
Bell 206	1886	5.64	1	99.93	18.9	160837	11.7
Bell 412	5409	7.01	1	154.38	35.0	628493	8.6
Bell AH-1 Cobra	4545	6.71	1	141.45	32.1	505731	9.0
Bell 22B	3750	6.4	1	128.68	29.1	397385	9.4
Boeing CH-45	9706	7.62	1	182.41	53.2	1389814	7.0
Boeing CH-47C	14969	9.15	1	262.73	57.0	2217966	6.7
MBB BO 105	2600	4.91	1	75.8	34.3	298914	8.7
MBB BK 117	3200	5.5	1	95.03	33.7	364515	8.8
Hughes 500E	1364	4.02	1	50.85	26.8	138674	9.8
AH-64 Apache	8022	7.32	1	168.1	47.7	1087829	7.4
Robinson R22	623	3.83	1	46.18	13.5	44919	13.9
Schweizer 300	932	4.09	1	52.55	17.7	77047	12.1
Sikorsky UH-60	10000	8.18	1	210.11	47.6	1354245	7.4
Sikorsky ch-53r	33409	12.04	1	455.41	73.4	5617129	5.9
Sikorsky s-76a	4671	6.71	1	141.26	33.1	527261	8.9
TILT-ROTOR							
V-22 Osprey	23859	5.8	2	211.366354	112.9	4976006	4.8
Agusta Westland AW609	7620	3.95	2	98.0333988	77.7	1318760	5.8

Bell V-280 Valor	26000	5.35	2	179.840471	144.6	6136727	4.2
Bell Eagle Eye	1020	1.525	2	14.6123328	69.8	167287	6.1
Bell XV 15	6804	3.8	2	90.7291958	75.0	1156627	5.9

UAM Data

UAM	Mass (kg)	Rotor radius (m)	Number of rotors	Disk area (m ²)	Disk loading (Nm ⁻²)	Power(kW)
Volocopter 2C	900	1.15	18	74.7	12.0	360
Airbus Vahana	2200	1.4	4	24.6	89.3	800
Boeing Aurora Flight Sciences Pegasus PAV	800		8			600
BlackFly International	255	0.455	8	5.2	49.0	250
E-Hang 184	360	0.8	4	8.0	44.8	1216
Kitty Hawk Cora	1224			13.6	90.0	

UAM	Ideal power(W)	Hover efficiency	Cruise speed (km/h)	Max speed (km/h)	Range (km)	Source
Volocopter 2C	61288	15		110	35	1
Airbus Vahana	408152	5	190	220	50	2
Boeing Aurora Flight Sciences Pegasus PAV					80	3
BlackFly International	35043	7	130		64	4
E-Hang 184	47280	8	100	130	35	5
Kitty Hawk Cora	227941	5	180		100	6

Source list:

Source

- 1 <https://www.volocopter.com/en/product/>
- 2
- 3 <https://evtol.news/aurora/>
- 4 <https://www.opener.aero/#technology>
- 5 <https://www.ehang.com/ehangaav>
<https://evtol.news/ehang/>
- 6 <https://kittyhawk.aero/>